Bulk sensitive Photoelectron Spectroscopy of strongly correlated transition metal oxides

Inaugural–Dissertation
zur
Erlangung des Doktorgrades
der Mathematisch–Naturwissenschaftlichen Fakultät
der Universität zu Köln

vorgelegt von
Thomas Christoph Koethe
aus Düsseldorf

Köln 2007

Contents

Chapter 1

Introduction

1.1 Strongly correlated transition metal oxides

Modern solid state research has focused to a considerable extent on the physics of strongly correlated electron systems, because here we find interesting phenomena arising from conditions far away from well understood limiting cases. Being such systems, the transition metal oxides have shown to be a very wide ranged field for researchers to find unexpected properties like unconventional superconductivity in the high–T_c cuprates [1] and the ruthenates [2], large magnetoresistance effects in manganites (CMR) [3], and cobaltates (GMR) [4, 5], as well as unusual phase transitions like metal–insulator– [6] or spin–state transitions [7], and many more. Correlated systems provide the advantage to test novel theoretical models and methods of computation, and mark the frontier for fundamental research, not to mention the unpredictable technological impact. In other words, transition metal oxides represent model systems for the development of theoretical descriptions, and therefore are essential for the progress of our understanding of nature. On the other hand, the physical properties found in these materials are invaluable for technological applications, and in some cases even open up completely new possibilities. They can often be tuned in a certain range by external parameters like temperature, pressure, external electric or magnetic fields, or composition, e. g. by doping. In order to optimize the properties of a material for a specific application, a solid understanding of their physics is required.

The characteristics of a solid are to a large extent determined by the electronic structure. This includes the electronic configuration of the ground state of the system, as well as electronic excitations, which are responsible for the macroscopic properties like resistivity, magnetism and so on. The experimental investigation of the electronic structure is therefore an essential part in the attempt to understand the physical properties of a material. A wide range of spectroscopic methods is available and is also needed to investigate the electronic excitations, and in turn provides insight into the mechanisms responsible for its macroscopic physical properties. Photoelectron spectroscopy (PES) investigates the excitations from the ground state to all accessible final states with an electron removed, or in other words, a hole injected to the system [8–10]. It is therefore by concept directly related to the one-hole propagator, represented by the Green's function. In the actual measurement,

however, we encounter practical difficulties that can prevent us from extracting the true one-particle Green's function of the bulk system from the experimental spectra. The most important one is the surface contribution to the spectra, which has in the past often been neglected in the analysis, though in most cases not at all negligible. For correlated systems, this is particularly serious since correlation effects are known to be most sensitive to the local environment, and in turn the electronic structure of the surface may well be quite different from the bulk. In the transition metal oxides, this is a consequence of the atomic like $3d$ orbitals which make up the low energy excitations in a PES spectrum. We can demonstrate the remarkable differences between surface and bulk electronic structure, and the confusion in the literature resulting from the discussion of experimental data without account of surface effects, using as an example $LaCoO_3$. Our bulk-sensitive study reveals that the bulk system is predominantly in a low spin state up to room temperature, with a thermally populated higher spin state contribution, whereas the surface appears to be in a high spin state independent of temperature. The lack of bulk sensitivity is also the reason why the experimental photoemission data of VO_2 available in the literature did not show the enormously large transfer of spectral weight across the metal-insulator transition observed in our bulk-sensitive experiment. The same is true for the absence of distinctive satellite features in the valence band and core level spectra of Ti_2O_3 in the literature data, and the confusing assignments made for the spectral features in the valence band of $GdBaCo_2O_{5.5}$. These examples show the importance of bulk sensitivity in the investigation of the electronic structure of correlated systems, which is a major issue of today's solid state physics research.

1.2 Photoelectron Spectroscopy: theoretical concept

In a photoemission experiment, a sample is irradiated by light of well defined energy $h\nu$. An electron bound to the sample can be excited by the incoming photons and, in case its energy separation from the vacuum level is less than the absorbed photon energy, is emitted to the vacuum. As a result, the system makes an excitation from the N–particle initial state with energy E_N^0 to a $(N-1)$–particle final state of energy E_{N-1}^{FS}. The *binding energy* is identified with the difference of the total energies of the excited final state and the ground state, $E_\mathrm{b} = E_{N-1}^{FS} - E_N^0$. The photoemission spectrum then is given by the number of electrons as a function of binding energy. In this description, it is assumed that the photoelectron can escape the solid without interaction with the system left behind, called the sudden approximation. Its validity is the better the higher the kinetic energies of the photoelectrons, as scattering cross sections decay accordingly.

A clear distinction has to be made between the energy scale of the exciting photons and the energy of the excited final states with respect to the ground state, the binding energies. In principle, any final state with total energy not more than the photon energy above the ground state, can be reached. The excess energy of the excitation process, given by the difference of photon energy and binding energy, results in kinetic energy of the photoemitted electron, plus the so–called work func-

tion necessary to overcome the vacuum threshold. Therefore, in a PES experiment not only the high lying excitations with energies close to the photon energy can be measured, but also the low–energy excitations close to the Fermi energy. However, in order to detect sharp and low–lying excitations, the experimental setup has to have an adequate energy resolution. For instance, in order to get a reasonably resolved valence band spectrum, a resolution of the order of 0.1 eV is necessary, while in x–ray photoelectron spectroscopy (XPS) the excitation energies are of the order of 1 keV.

In order to find a theoretical description of the information provided in a PES spectrum, we have to take a close look at the photoemission process, starting out from the transition probability within Fermi's Golden Rule,

$$W_{IS,FS}^{\text{PES}} \propto |\langle FS_N|\mathcal{O}^{\text{PES}}|IS_N^0\rangle|^2 \delta\left(E_N^{FS} - E_N^0 - h\nu\right). \tag{1.1}$$

In this expression, $|IS_N^0\rangle$ represents the initial state, which is the ground state of the system with energy E_N^0. $|FS_N\rangle$ refers to a N–particle final state with energy E_N^{FS}. The photoemission process is signified by the operator $\mathcal{O}^{\text{PES}}$, generally given by the operator of interaction between light and matter, $\mathcal{H}^{\text{int}} = \mathbf{A} \cdot \hat{\mathbf{p}} + \text{h.c.}$, with the vector potential of the electromagnetic field $\mathbf{A}$ and the quantum mechanical particle–momentum operator $\hat{\mathbf{p}}$. The photoemission operator can be identified with the electromagnetic dipole interaction, $-e\hat{\mathbf{r}}$, with the unit charge e, and takes in second quantization the form

$$\mathcal{O}^{\text{PES}} = \sum_{k,i} M_{k,i}\varepsilon_k^\dagger c_i, \tag{1.2}$$

composed of the optical matrix elements $M_{k,i} = \langle k|\mathcal{H}^{int}|i\rangle$, the creation operators $\varepsilon_k^\dagger$ of a photoelectron with momentum k, and the annihilation operators c_i of a bound electron in the one–particle state $|i\rangle$. The N–particle final state thus includes both the system of $N-1$ electrons bound to the solid, and the photoemitted free electron. In the sudden approximation, the two components separate, and the final states are given by

$$|FS_N(k,j)\rangle = \hat{a}|k\rangle|FS_{N-1}(j)\rangle, \tag{1.3}$$

where $\hat{a}$ is the anti–symmetrization operator, $|k\rangle$ represents the photoelectron with energy E_k, and $|FS_{N-1}(j)\rangle$ denotes the eigenstates of the $(N-1)$–electron system with quantum numbers j and energies $E_{N-1}^{FS}(j)$. Hence, the total energy of the N–particle final state is the sum of the energies of the $(N-1)$ electron system and the photoelectron, $E_N^{FS} = E_{N-1}^{FS}(j) + E_k$, such that conservation of energy is accomplished by the δ–function in the transition probability (1.1).

In order to evaluate the matrix element in (1.1), we also express the initial state as an anti–symmetrized product of a one–particle state, which is annihilated in the photoemission process, and a $(N-1)$ particle state,

$$|IS_N^0\rangle = \hat{a}|i\rangle|IS_{N-1}(i)\rangle = c_i^\dagger|IS_{N-1}(i)\rangle, \tag{1.4}$$

in which $|IS_{N-1}(i)\rangle$ does not need to be the ground state or even an eigenstate of the $(N-1)$ electron subsystem. In fact, such a separation of the N electron state

does not necessarily have to be meaningful, but we can always find an approximate product state instead. From the representation (1.2) of the photoemission operator in second quantization, we see that it acts on the one–particle states only, and by substituting (1.4) and (1.3) into (1.1), we find

$$W_{i,(k,j)}^{\text{PES}} \propto \lim_{\eta \to 0} \frac{1}{\pi} \text{Im} \frac{|\langle k|\mathcal{O}^{PES}|i\rangle\langle FS_{N-1}(j)|c_i|IS_N^0\rangle|^2}{E_{N-1}^{FS} + E_k - E_N^0 - h\nu - \mathrm{i}\eta}, \qquad (1.5)$$

where the δ–function was rewritten by use of $\lim_{\eta \to 0} \text{Im}\frac{1}{x - \mathrm{i}\eta} = \pi\delta(x)$. The photoemission spectrum as a function of the photoelectron energy E_k is given by the sum of (1.5) over i, corresponding to all possibilities of exciting bound electrons, and over j, according to all possible final states fulfilling energy conservation. With the choice of $|FS_{N-1}(j)\rangle$ as eigenstates of the $(N-1)$ electron system, we can use the completeness relation of this basis set in the sum of (1.5) over j, yielding

$$I^{\text{PES}}(E_k) \propto \lim_{\eta \to 0} \frac{1}{\pi} \text{Im} \sum_{i,i'} M_{k,i} M_{i',k} \langle IS_N^0|c_{i'}^\dagger \frac{1}{\mathcal{H} + E_k - E_N^0 - h\nu - \mathrm{i}\eta} c_i|IS_N^0\rangle, \quad (1.6)$$

sometimes referred to as the *photocurrent*. We recognize on the right hand side of (1.6) the spectral function $A(E_k)$ in the limit $\eta \to 0$, convoluted with optical matrix elements. The spectral function is given by the imaginary part of the one–*hole* propagator, the Green's function $\mathcal{G}(E_k)$. The photoemission spectrum peaks at photoelectron energies corresponding to poles in (1.5), i.e. at

$$E_k = E_N^0 + h\nu - E_{N-1}^{FS}. \qquad (1.7)$$

Note that the often used correspondence between the photoemission spectrum of a system and its occupied electronic density of states in a one-electron description is in general incorrect, as it completely neglects the many-body character of the excitation. The conceptually simple and elegant description of PES in (1.6) makes it a powerful and appealing experimental tool for the investigation of solid state systems. There are, however, practical difficulties which can hamper the access to the basic information on the electronic properties of the system in the actual measurement, as will be discussed in the following section.

1.3 Photoelectron Spectroscopy: Bulk vs. Surface

In photoemission, one always has to deal with surface sensitivity in the sense that a comparably large fraction of the photoemission signal originates from the first few layers of the crystal. This is because the excited photoelectron may lose a certain amount of its kinetic energy due to inelastic scattering with the crystal lattice and electrons. The longer the distance that the photoelectron has to cover until it leaves the crystal, the higher the probability for scattering processes and the average loss of energy. At some point, the electron lost too much energy to overcome the vacuum threshold and cannot escape from the crystal.

Assuming an exponential decrease of the relative number of photoelectrons escaping the sample with distance z from the surface with an inelastic mean free path λ,

$$N(z) = N_0 e^{-z/\lambda}, \qquad (1.8)$$

the volume of the sample probed in a photoemission experiment, is given by λ, denoted as the escape depth, together with the emission angle (cf. figure 1.2). The value of the escape depth is not a sharp number but an average and moreover depends on kinetic energy. It is claimed to be more or less insensitive to the material, since the photoemission final states lie very high in energy ($\approx h\nu$ for emission from the valence band), and as a result behave in good approximation like free electrons, independent of the specific properties of the solid they propagate in. From a large

Figure 1.1: Electron escape depth as a function of kinetic energy for various metals. The data indicate a universal curve with a minimum of 2 – 5 Å for kinetic energies of 10 – 100 eV. Figure taken from Prutton [11], as reproduced from [12].
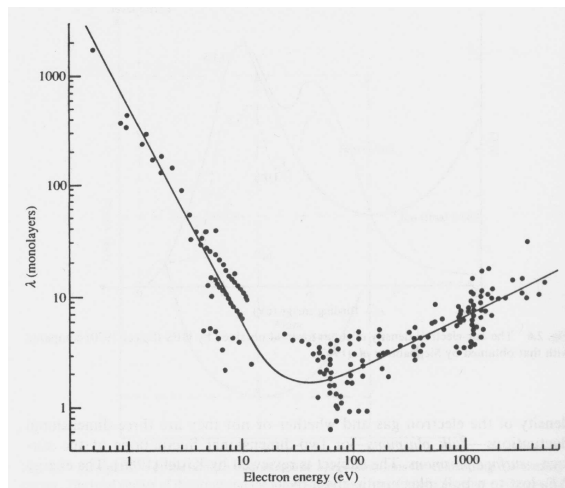
number of measurements, the so–called *universal curve* has been extracted, given as a solid line in figure 1.1. It shows that the escape depth ranges between 1 and ≈ 20 Å for photon energies between 10 and 1500 eV, as commonly used in experiment, with a minimum around 50 eV. This means that in a crystal with lattice spacings of a few Å, a photoemission experiment will probe only up to at most ten monolayers. Furthermore, according to (1.8) the intensity from the surface layers will be disproportionately higher than from deeper layers, causing the spectra to be even more surface sensitive. Note that the validity of the universal curve in the case of correlated systems, especially the increase of the escape depth for photon energies below 10 eV has been questioned, thus the relevance of ultra–violet photoelectron spectroscopy (UPS) for bulk properties, see e. g. [13]. Actually, the escape depth has to be strongly dependent on the electronic structure of the system, since it is determined mostly by the scattering amplitude of the photoelectrons with the electronic system of the solid. Therefore, systems with a wide electronic gap like the band insulators MgO or $SrTiO_3$, for which low energy scattering processes are dominated by the comparably weak electron–phonon interaction, are found to have very large values of the escape depth. Note also that the penetration depth of the light in any case is orders of magnitudes larger and will not be a limiting factor.

The extreme surface sensitivity in the low photon energy range may be advantageous and welcome for experiments focused on surface properties. However, in most cases the electronic structure of the bulk material is supposed to be under investigation, and therefore the degree of bulk sensitivity has to be known at least roughly. It has to be kept in mind that maybe not even the most part of the experimental data is representative of the bulk system. Considering the intrinsic surface sensitivity of PES, in order to extract from the measured spectra meaningful infor-

mation about the bulk electronic properties, the conditions of measurement have to be carefully chosen to optimize for bulk sensitivity. A number of aspects have to be mentioned in this context, the photon energy being only one of them. As the universal curve in figure 1.1 suggests, the escape depth is maximized by choosing the highest possible photon energy. However, apart from technological difficulties concerning high energy light sources of appropriate resolution etc. on the one hand, and correspondingly electron energy analyzers working in a high voltage range on the other hand, there are also difficulties arising from the photoemission process itself for high photon energies, mainly due to the strong decrease of the photoionization cross sections with photon energy, resulting in very low count rates in the experiment. Only in the last few years, considerable progress has been made in the field of hard x–ray PES (HAXPES or HXPES) with photon energies of 10 keV and more, yielding very promising bulk sensitivity, but also a number of experimental, conceptual and technological challenges [14–16]. But even in conventional soft x–ray photoemission, escape depths of 15 – 20 Å can be realized with photon energies of a several hundred eV, customarily available in contemporary synchrotron beam lines or conventional x–ray sources, thus providing a reasonable bulk sensitivity in most cases.

Another significant issue in terms of bulk sensitivity is the sample preparation, which is a matter of several aspects. One of them is the quality of the sample, not only in the sense of composition, but also of the surface definition. In this respect, the use of single crystals is naturally preferable, since here the surface is well defined in terms of lattice planes, and usually an even surface termination can be achieved. On the other hand, polycrystalline samples, which in most cases can be synthesized by much less sophisticated means, are more commonly, sometimes even the only samples available at all. However, the surface of a polycrystalline sample does not have a well defined orientation, and will therefore not be flat and even. This not only increases the surface area, but also effectively reduces the bulk probing volume. As a result, the surface contribution to the photoemission spectrum of a polycrystalline sample is considerably enhanced with respect to the bulk contribution, as compared to a single crystal sample. Moreover, to establish a clean surface is for polycrystalline samples much harder. First of all, the roughness of the surface results in a higher degree of contamination. The often used method to scrape off surface contamination, due to the granular consistence more easily tends to bury adsorbate atoms into the surface instead of removing them. Upon fracturing polycrystalline samples instead, again a rough surface is produced, which is rather determined by grain boundaries and impurities, than by the crystal structure, and so is of poor crystalline quality.

These difficulties exist in principle for single crystals as well, but mostly are less severe. Scraping the surface is unfavourable, not only due to the danger to rub in impurities, but also because of the macroscopic scratches left on the surface, which in turn becomes more like a polycrystalline sample. The bottom line is, that the desirable condition is a single crystal which is cleaved *in–situ*, this means split in such a way, that a well defined surface of low crystallographic indices shows up. This is not always possible, however. While many ionic compounds of simple lattice structure usually cleave nicely into specular surfaces, systems of more complicated structure, or soft materials rather break into terraced surfaces or are simply cut

along the blade.

After so much efforts have been made to establish a well defined clean and flat surface, we still have to take a lot of care about the sample quality. On the one hand, the sample exposes a surface of a certain reactivity to an atmosphere of the lowest possible pressure. As an example, we consider the case that every particle which hits the surface, will stick there, expressed by a sticking coefficient $S = 1$. An exposure of this surface to a pressure of 2.5×10^{-6} torr over one second, a quantity referred to as 2.5 L (Langmuir), results in an estimated contamination of one monolayer. As a result, at a pressure of 10^{-9} mbar, and with a sticking coefficient of one, the surface is completely covered with adsorbate particles within one hour. Therefore, the sample has to be kept under ultra high vacuum (UHV) conditions, and the experiment should be completed in a few hours — depending on the actual pressure, and the sticking coefficient, which fortunately often is small. As a measure of the surface contamination, photoemission lines of the most common contaminants carbon and oxygen (mostly in form of carbon monoxide and water) can be monitored repeatedly over the time of measurement — usually, if the photon energy permits, the $1s$ core levels at $\approx$ 285 and 530 eV, respectively, with the precise binding energies depending on the chemical environment. On the other hand, not only surface contamination effectively changes the sample actually being measured, but also the chemical stability of the system. The sample might either react with contaminants like oxygen, or the chemical composition might change due to evaporation of some constituents, both leading possibly to a system with completely different properties. Since the line shapes and energy positions of the peaks depend on the chemical species, changes in the spectra with time show up clearly and indicate sample degradation.

Still the optimally bulk sensitive experimental setup does not necessarily result in spectra primarily related to the bulk properties. After all, the surface contribution may still be more than negligible and consequently disturb the spectra. In the analysis, possible surface contributions must be considered, preferably by subtraction of a particularly surface sensitive reference spectrum. There are several ways to subtract surface contributions: one is to take the same spectrum at low photon energy, resulting in a considerably shorter escape depth (see figure 1.3) [17]. This approach is however impractical in cases, where the spectrum consists of contributions with independent photoionization cross sections, e. g. from different constituents in a compound, because these also change with photon energy. In turn the shape of the spectrum may change completely, irrespective of any surface effects [18]. As was discussed above, scraping a single crystal can increase the surface contribution to the spectrum noticeably. Another way to increase the surface sensitivity intentionally, is by changing the emission angle [17]. As illustrated in figure 1.2, with a fixed escape depth of the photoelectrons, given by the height of the blue hatched area, the contribution from the bulk (green) to the spectrum is maximized for electrons emitted normal to the surface (blue arrow), resulting in the most bulk sensitive geometry. Note that the surface region (yellow) still makes up a significant fraction of the total probing volume (blue hatched). In contrast, electrons emitted under an angle to the surface normal (red arrow), can still travel the same distance through the solid to the surface, however, a substantially larger fraction of the path is in the surface

region, which means that a correspondingly smaller number of photoelectrons originates from the bulk region. In other words, while the surface volume is the same as for normal emission, the bulk contribution to the probed volume (red hatched) is noticeably smaller. At an angle of $60°$ with respect to the surface normal, the effective probing depth is reduced by a factor $1/2$. This procedure is, however, subject to the constraint of a well defined surface orientation, since otherwise the definition of the emission angle becomes meaningless. In experiment, this means that the surface has to be flat on the scale of the measured area, i. e. the spot size of the light.
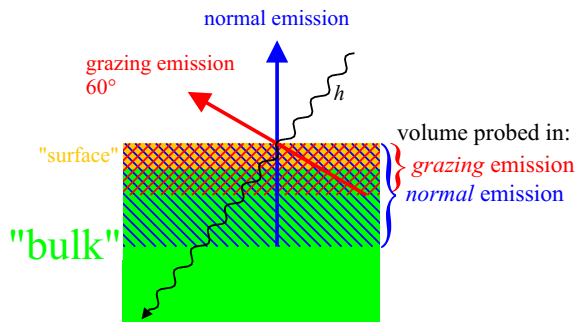

Figure 1.2: The probing volume for normal emission (blue hatched) maximizes the contribution of the bulk (green). The contribution of the surface (yellow) is the same in grazing emission (red hatched), but due to the fixed escape depth, the probing depth is reduced by a factor $1/2$ at $60°$.

The surface sensitivity in PES would not be a major issue if the properties of the system at the surface were equal or at least very similar to the bulk. However, the broken discrete translational invariance at the surface leads to electronic states that are confined to the surface, and in turn do not represent bulk properties. Such surface states tend to show up in the spectrum in form of sharp structures of high intensity, possibly much more pronounced than the actual bulk features. In the case of Sr_2RuO_4, this situation had created considerable confusion in the literature, when the surface state was not identified as such at first, but interpreted as a bulk feature [19]. The conclusions drawn from this misinterpretation were in disagreement with findings of more bulk sensitive methods [20], and the discrepancy was only resolved by realizing the surface nature of the controversial feature [21].

Moreover, the change in environment at the surface, and the possible associated relaxation of the lattice, can lead to substantial changes in the electronic properties of the system at the surface. This is of particular importance for correlated systems, the properties of which often crucially depend on a delicate balance of different energy scales, e. g. hybridization strength vs. crystal field, exchange, or local Coulomb repulsion energy. The changes at the surface are most likely to result in a significantly modified electronic structure, as has been shown for a number of correlated systems like rare earth compounds. As an instructive example, Ce $3d$ core–level photoemission spectra of $CeIr_2$ taken by Laubschat *et al.* under varying conditions of surface sensitivity are shown in figure 1.3. The spectra consist of three spin–orbit doublets A, B and C related to different final state configurations, $4f^0$, $4f^1$ and $4f^2$, respectively. It turns out that the intensity of structure B changes noticeably both with photon energy, and with emission angle, indicating that it is strongly related to the surface sensitivity of the spectra. In both cases, the intensity consistently appears to be enhanced in the more surface sensitive setup, suggesting that the corresponding final state has an increased overlap with the ground state at the surface. The stabilization of the respective ground state contribution $4f^1$ at

Figure 1.3: Ce–$3d$ core–level photo-emission spectra of CeIr$_2$ recorded with varying surface sensitivity: (a) for different photon energies and constant electron–emission angle, $\theta = 20°$; (b) for different angles θ and constant $h\nu = 1486.6$ eV. The spectra consist of three $3d_{3/2}$–$3d_{5/2}$ doublets due to different $4f$ final state configurations; they are normalized to the same intensity of doublet A and corrected for background. Figure taken from Laubschat *et al.* [17].
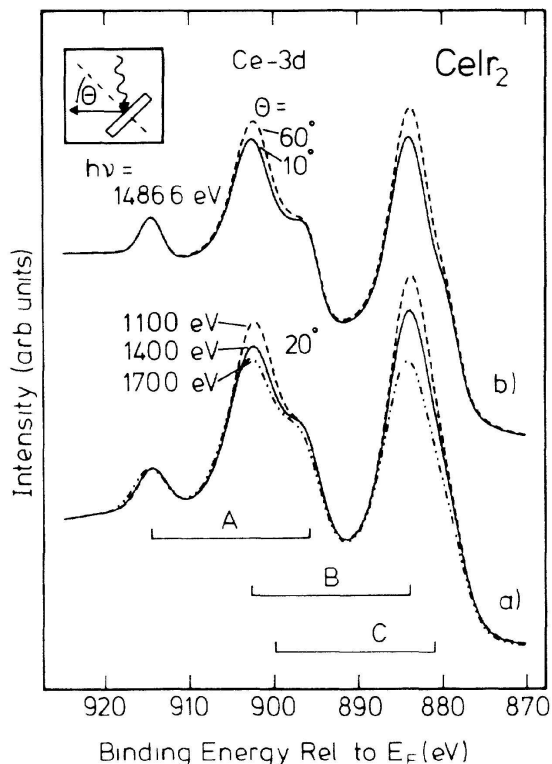
the surface is supported by similar findings in Ce–$4f$ core–level PES. This is interpreted as a strong reduction in the $4f$ hybridization at the surface, which can be confirmed by quantitative simulation of the spectra. The analysis of the surface sensitivity dependence not only demonstrates drastically the degree of dissimilarity in the electronic structures of bulk and surface, but also gives a quantitative example of the importance of a consideration of surface effects: previous PES studies of the same systems not taking surface effects into account, had given averaged values of hybridization energies of less than 50% of the true bulk value, and as a result were in disagreement with theoretical predictions [22].

Similarly confusing results have been found in low photon energy measurements from CeRu$_2$Si$_2$ and CeRu$_2$, which are expected to have significantly different electronic properties. While CeRu$_2$Si$_2$ is a so–called heavy fermion system of rather localized $4f$ states and a Kondo temperature $T_K = 25$ K, the electronic structure of CeRu$_2$ is assumed to be characterized by itinerant $4f$ electrons due to stronger hybridization, resulting in a Kondo temperature of the order of 1000 K. Despite the quite different nature of the $4f$ electronic structure, the low photon energy spectra of these systems turn out to be surprisingly similar [18]. As higher photon energy spectra reveal, however, this result is due to the similar *surface* properties of the two compounds, while the actual *bulk* spectra in fact display very dissimilar line shapes, reflecting the different electronic properties [18].

Another famous example where the surface sensitivity issue of PES has led to a misinterpretation of the results, and as a consequence to a wrong model, is the calcium substitution series of the perovskite strontium vanadates, Sr$_{1-x}$Ca$_x$VO$_3$ [23, 24]. The valence band photoelectron spectra of polycrystalline samples taken with UV light ($\hbar\omega \leq 50$ eV) display a striking x dependence which was interpreted as

a consequence of the increasing distortion from the regular structure for $x = 0$ with a V–O–V bond angle of 180°. As the bandwidth W is assumed to be reduced with distortion, the value of U/W increases and correlation effects are expected to gain importance on the spectra. Thus the system was concluded to be close to a Mott–Hubbard transition controlled by bandwidth on tuning the composition. The observed spectra were explained in terms of non–local correlation effects introducing a k–dependent self–energy. On the other hand, thermodynamic and magnetic studies of the vanadates did not show according x dependent behaviour, which led to some confusion and a controversial discussion of either findings [25]. A reinvestigation of the photoemission study using higher photon energies up to 900 eV, and applying a careful surface treatment, was necessary to resolve this issue [13]. Figure 1.4 shows
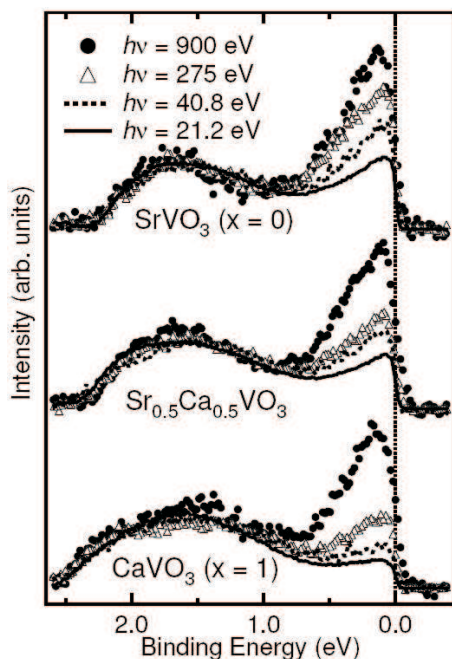
Figure 1.4: Photon energy dependent V3d PES of $Sr_{1-x}Ca_xVO_3$. While the low photon energy spectra change with composition, the high photon energy spectra are independent of x. Taken from Sekiyama *et al.* [13].

the changes of the V 3d spectrum with photon energy, and demonstrates that the seeming x dependence at low photon energies vanishes at higher ones. The decisive improvement of this approach over the previous ones consists in the bulk sensitivity achieved by both a much longer escape depth, from figure 1.1 estimated a factor four, and a well defined clean surface. The changes in the spectra observed in UPS were thus traced back to surface effects and therefore not representative of the bulk.

The importance of surface effects and even the mere consciousness of their presence are of particular importance, as it happens time and time again that experimental results have led to wrong interpretations on the ground of such issues. The credibility of PES in general has suffered severely from reports in the literature of erroneous findings due misinterpretation caused by disregard of surface effects, as the above examples demonstrate. It is therefore extremely important to make sure to which extent the measured spectra are actually representative of the bulk electronic properties of the studied system, and in particular to reduce the *inevitable* surface contribution as much as possible. In these conditions, PES is a very powerful technique in contemporary solid state science, and permits access to information that no other method can give.

1.4 Scope

The results of bulk-sensitive photoelectron spectroscopy from a number of correlated transition metal oxides are presented in this thesis. We have chosen systems of model character, not only interesting by themselves, but in particular as examples for a whole class of systems, and as such important test cases for recent theoretical models. In turn, the quality of the experimental data has to be adequate for a comparison to model calculations, above all, the degree of bulk sensitivity. As we have discovered, a large number of previous studies available in the literature turned out to be not sufficiently bulk sensitive, and as a result do not represent reliable data for theoretical modeling.

In chapter 2, we present a detailed study of the different contributions from surface and bulk to the valence band spectra of $LaCoO_3$ in the range from 65 K to room temperature, using photon energies between 450 eV and 6 keV and varying degrees of surface sensitivity. We observe a prominent low binding energy peak of temperature dependent weight, which is characteristic of a Co^{3+} low spin state. By contrast, this feature is not present in previously published results of various groups. We can show that the literature results are not representative for the bulk system. By analyzing the emission angle dependence of the spectra, we have been able to separate the bulk and surface contributions. We observe a temperature dependent, predominantly low-spin bulk spectrum, corresponding to the proposed spin state transition, in accordance with the magnetic susceptibility. At the same time, the surface is temperature independent. Based on the line shape analysis, we infer that the Co^{3+} ion at the surface is in a high spin state.

In chapter 3, we present a detailed study of the valence and conduction bands of VO_2 single crystals across the metal-insulator transition using bulk-sensitive photo-electron and O-K x–ray absorption spectroscopies. Our measurements reveal a giant transfer of spectral weight, much more pronounced than shown in previous reports, and even more than that in V_2O_3 [26]. Particular spectral features signal that the transition is not of the standard Peierls nor single-band Mott-Hubbard type. The valence band spectrum of the metallic phase is characterized by two structures in the V $3d$ contribution which can be identified with the coherent and incoherent parts of the spectrum. The symmetry and energies of the bands are discussed in connection to the recently determined orbital occupation [27] and to the importance of the k-dependence of the self-energy correction [28]. This analysis reveals the decisive role of the V $3d$ orbital degrees of freedom. The orbital switching is the key for opening a band gap that is much larger than the energy scale of the transition temperature. Comparison to recent realistic many body calculations within the dynamical mean field theory using a two-site cluster, shows that much of the k-dependence of the self-energy correction can be cast within a dimer model.

The results of the bulk-sensitive photoemission study of the low temperature insulating phase of Ti_2O_3 using both soft and hard x–ray photons are presented in chapter 4. We find in both the valence band and the Ti $2p$ core level spectra structures that have not been reported in the literature yet. The Ti $3d$ spectral weight displays a two peak structure in the insulating state, which can be identified with the bonding- and antibonding contributions associated with the c axis Ti–

dimers in the crystal structure. Also in the Ti $2p$ core level spectra we observe additional satellites at lower binding energies. We can find qualitative understanding of these satellites in terms of non-local screening effects from the hydrogen molecule model.

Finally, in chapter 5 another cobaltate system, the recently synthesized $GdBaCo_2O_{5.5}$, is presented. The Co ions possess the same $3d^6$ configuration as in $LaCoO_3$, however the distinct crystalline environment leads to considerably different properties. With a bulk-sensitive high resolution x–ray photoemission investigation in the temperature range of 80 - 380 K we are able to give reliable information on the electronic properties and the temperature dependence of the spin state in this system. We find that the gap remains finite up to 380 K, implying that the high temperature phase above the so-called metal-insulator transition is actually not metallic, in contrast to opposite claims of previous XPS investigations of $TbBaCo_2O_{5.5}$. We show furthermore that the dominating low-spin contribution commonly claimed for the octahedral site at low temperatures does not show up in the valence band spectra. From the line shape and the weak temperature dependence in comparison with $LaCoO_3$ we can derive an upper bound for the low spin contribution of 25% at 80 K. These findings cast doubts on most of the current models proposed to explain the complex magnetic and transport behaviour of the layered cobaltates.

Chapter 2

Bulk vs. Surface electronic structure of LaCoO$_3$

2.1 Introduction

The perovskite transition metal oxides have always been important model systems in the field of solid state physics, as they exhibit a wide range of physical properties and unusual phenomena. One of the most prominent examples of this class is LaCoO$_3$, showing a complicated and still not well understood thermal behaviour in the electronic transport and magnetism properties [29, 30]. It was noticed in the earliest studies in the 1950s already, that these peculiarities are closely related to the $3d^6$ electronic configuration of the Co^{3+} ions [31], which has several closely lying configurations with different *spin state* character. LaCoO$_3$ is also important since it can be considered as the parent compound to a wide range of related systems with interesting properties, like the giant–magentoresistance systems of the doping series La$_{1-x}$Sr$_x$CoO$_3$ [4], and the oxygen deficient systems RBaCo$_2$O$_{5+\delta}$ (R = rare earth, see chapter 5). It also represents a model system for the currently very popular unconventional superconductor Na$_x$CoO$_2 \cdot y$H$_2$O [32]. This means that the complete comprehension of LaCoO$_3$ is of enormous meaning for the field of cobalt based materials.

   The crystal structure of LaCoO$_3$ is a slightly distorted rhombohedral perovskite with two formula units per unit cell, in which the two Co sites are equivalent [33]. The weak distortion seems to have no significant influence on the electronic properties. The resistivity and magnetic susceptibility in the temperature range up to 800 K are shown in figure 2.1 [34]. The resistivity shows a quite unusual behaviour with a thermally activated decrease up to 200 K, followed by a plateau, and an again steeper slope around 400 K. At the same time, the magnetic susceptibility is essentially zero at $T = 0$ (contributions from impurities in the raw data, open circles in figure 2.1, can be well described by a Curie law, and subtracted, solid circles), increases at finite temperature up to a maximum at ≈ 100 K, before it turns down again with seemingly a Curie–Weiss behaviour up to another anomaly spread over the range from 400 K to around 600 K.

   The vanishing magnetic susceptibility at $T = 0$ suggests that the ground state of LaCoO$_3$ is non–magnetic, i. e. $S = 0$, consistent with the absence of any long–range
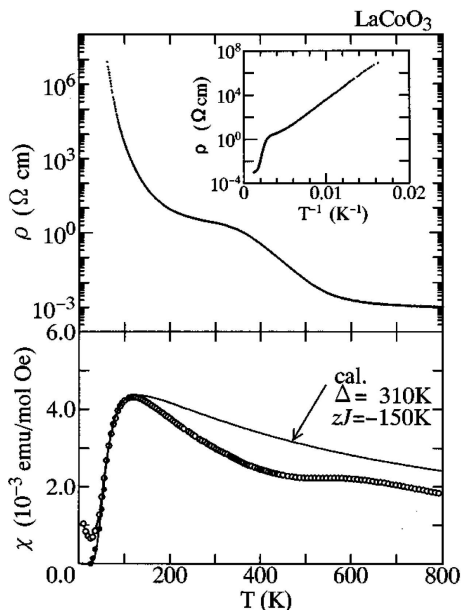
Figure 2.1: Temperature dependence of electrical resistivity (upper panel) and magnetic susceptibility (lower panel) for a crystal of LaCoO$_3$. The inset in the upper panel shows the Arrhenius plot of the resistivity (ρ). Closed circles below 100 K for the susceptibility represent the result of the subtraction of the contribution from Curie–like impurities. A solid line in the lower panel shows the calculated curve based on the molecular field approximation with an energy level separation Δ between the $S = 0$ (low–spin) and $S = 2$ (high–spin) state of the Co ion and with the antiferromagnetic interaction (zJ) between the neighboring high–spin ($S = 2$) Co ions. From Yamaguchi *et al.* [34].

magnetic ordering down to the lowest temperatures [35]. As temperature rises, some magnetic moment evolves, this means the electronic configuration must rearrange such that a finite spin moment results. In the $3d^6$ configuration, three different spin states are possible, as demonstrated schematically in figure 2.2. In a cubic crystal field $10Dq$, the $3d$ levels split into a threefold degenerate t_{2g} level lowered in energy by $-4Dq$ with respect to the energy center of gravity, and a twofold degenerate e_g level at $6Dq$. For a large value of the crystal field, the lowest $3d^6$ configuration would be t_{2g}^6, which results in $S = 0$, denoted as the low–spin state (LS). On the other hand, Hund's rule demands a high–spin state (HS) given by $t_{2g\uparrow}^3 e_{g\uparrow}^2 t_{2g\downarrow}^1$ with $S = 2$ and an energy gain J_H per pair of parallel spins. Which spin state is lower in energy depends on the ratio of crystal field to exchange energy: for $10Dq \ll J_\mathrm{H}$, the HS is favoured, in the opposite case the LS. The two become degenerate in this simple ionic picture with cubic crystal field for $10Dq = 2J_\mathrm{H}$. There exists another possible configuration, namely the intermediate–spin state (IS) $t_{2g\uparrow}^3 e_{g\uparrow}^2 t_{2g\downarrow}^1$ with $S = 1$, which doesn't seem to be relevant for an isolated ion in a cubic crystal field, as the energy diagram in figure 2.2 shows, because in any case it will be higher in energy than either the LS for a large crystal field, or the HS for a small one. However, the IS configuration may very well be stabilized by lower symmetry crystal fields, or due to band formation in the solid.

The earliest models proposed to explain the resistivity and magnetism of LaCoO$_3$ considered a single excited higher spin state to reproduce the observed temperature dependence in a qualitative way: the increase in magnetic susceptibility up to 100 K is explained by thermal population of either an IS [30] or HS [31, 35] less than 100 meV higher in energy than the LS, and the higher temperature behaviour is attributed to ordering of spin states [31]. The extremely small energy separation between the different spin states must be the result of a very delicate balance of the crystal field and the exchange interaction about the point of cross over [36]. The IS scenario was however claimed to be incompatible with early resistivity measurements [37] and not considered anymore in following investigations for a long time. In early
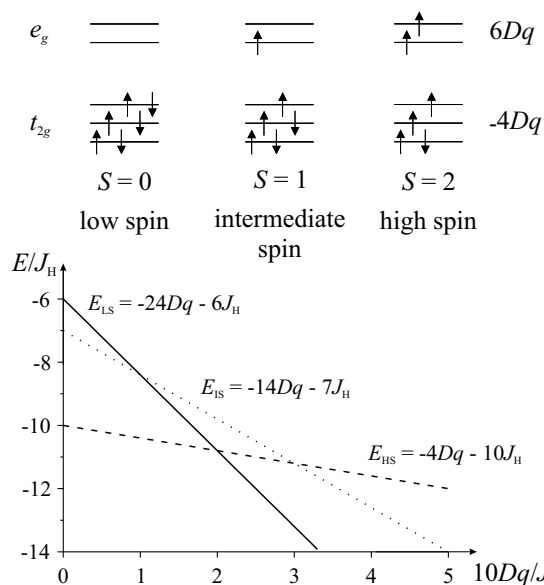
Figure 2.2: Possible spin states in the $3d^6$ configuration and corresponding energy level diagram for an isolated ion in a cubic crystal field $10Dq$ in energy units of J_H.

studies, also the decay of a pair of Co^{3+} ions into a Co^{2+} and a Co^{4+} has been considered to be essential for the transport properties at higher temperatures [7, 38].

The predictions of the early models, however, could not be validated by experiment, because neither spin state ordering [33] nor charge disproportionation [39–41] could be observed experimentally. Moreover, spectroscopic investigations claimed a LS up to 420 K and a gradual increase in the HS component at higher temperatures [41], which contradicts the magnetic susceptibility results of a spin state transition around 100 K [34]. Only in the mid 1990s, a twist in the discussion of $LaCoO_3$ was triggered by the theoretical proposal of an IS ground state configuration in the Co^{4+} charge transfer system $SrCoO_3$ [42]. As indicated above, hybridization of cobalt ions with oxygen ligands lowers the IS in the $3d^5$ configuration with respect to LS and HS. Since this material is assumed to have predominantly a $3d^6\underline{L}$ configuration, its electronic structure should be very similar to $LaCoO_3$. A following investigation of $LaCoO_3$ using band structure calculations on the basis of the density functional theory (DFT) in the local density approximation (LDA) including on–site repulsion U, has supported this suggestion, and proposed a completely new scenario for $LaCoO_3$ [43]. Like in the early models, the band structure calculations yield a LS ground state (i. e. at $T = 0$) responsible for the non–magnetic low temperature behaviour. The first excited states, however, are found to be IS, while the lowest configuration of HS appears at noticeably larger total energy. With rising temperature, the crystal lattice expands and as a result, the IS configuration with a singly occupied e_g orbital is stabilized by the energy gain due to strong hybridization with the oxygen ligands. The band structure calculations for changing lattice constants show a level crossing at the value corresponding to a temperature of 150 K, as displayed in figure 2.3. This means, that for larger lattice parameters, the lowest configuration is the IS, and in turn, a spin state transition from LS to IS takes place at the crossing point. The IS solution was taken to be orbitally ordered, so that it becomes semiconducting, in agreement with the experimental finding of insulating behaviour below $T = 400$ K. The orbital order is assumed to become unstable with
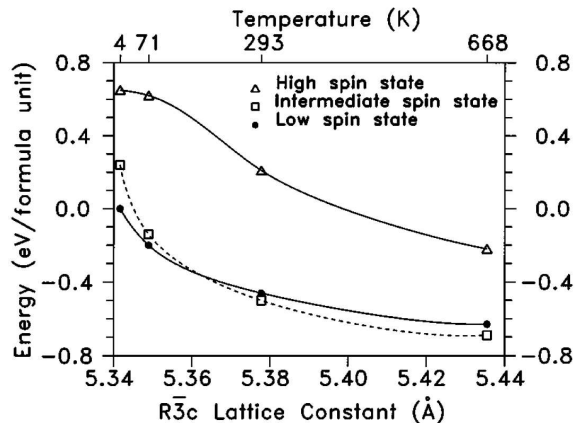
Figure 2.3: The total energies for various spin states of LaCoO$_3$ relative to the energy of the $t_{2g}^6 e_g^0$ state at 4 K vs. the $R\overline{3}c$ lattice constant. The corresponding temperatures are also marked. Taken from Korotin *et al.* [43].

respect to the metallic solution at higher temperatures. However, no evidence for orbital ordering has been found experimentally so far [44]. Moreover, the parameter $U = 7.8$ eV used in the band structure calculations, is considerably larger than the value of 5.5 eV extracted from spectroscopy [45], and consequently the energy gap at $T = 0$ of 2.06 eV is much too large as compared to experimental values ranging from 0.2 eV in optical spectroscopy [46] to 0.9 eV in electron spectroscopy [41, 47]. Nevertheless, the impact of this work was so influential, that many experimental results on LaCoO$_3$ and related systems have been investigated in terms of models involving the transition to the IS [5, 44, 48–55]. We would like to note that very recently, an LDA+U band structure investigation considering several magnetic configurations and also coexistence of different spin states found a mixed state of LS and HS to be lower in energy than both a uniform IS and a mixed LS and IS state [56]. This indicates that the predictive power of LDA/LDA+U investigations on the spin state of LaCoO$_3$ strongly depends on the details of the calculation and therefore should not be overvalued. Very recent experimental studies of the magnetic circular dichroism in the Co-$L_{2,3}$ x–ray absorption spectra support the very early proposal of a temperature dependent energy separation between the spin states [30, 57]. These results suggest a model of a LS ground state with thermal population of HS according to this temperature dependence.

Some confusion about LaCoO$_3$ also stems from discrepancies in experimental results of different techniques. As already mentioned, an early soft–x–ray absorption spectroscopy investigation failed to observe a spin state transition below 500 K, which is incompatible with the observed magnetic susceptibility [41]. It has to be noted, that x–ray absorption and photoemission spectra are in principle very sensitive to the spin state, as is demonstrated by the Co $3d$ photoemission valence band spectrum calculated for a CoO$_6$ cluster in the three different spin states shown in the left panel of figure 2.4 [48]. The spectra are clearly distinguishable, in particular the one corresponding to the LS initial state is characterized by a strong low energy line originating from the dominant process $t_{2g}^6(^1A_1) + h\nu \rightarrow t_{2g}^5(^2T_2) +$ photoelectron, well separated from the higher lying final states. The IS and HS spectra show a noticeable multiplet structure more equally spaced in energy, leading to broad features. Therefore a change in the experimental spectrum from purely LS at low temperature to the one at higher temperature with a thermally mixed in contribution of higher spin states, is expected to be clearly observable. However, the results of a
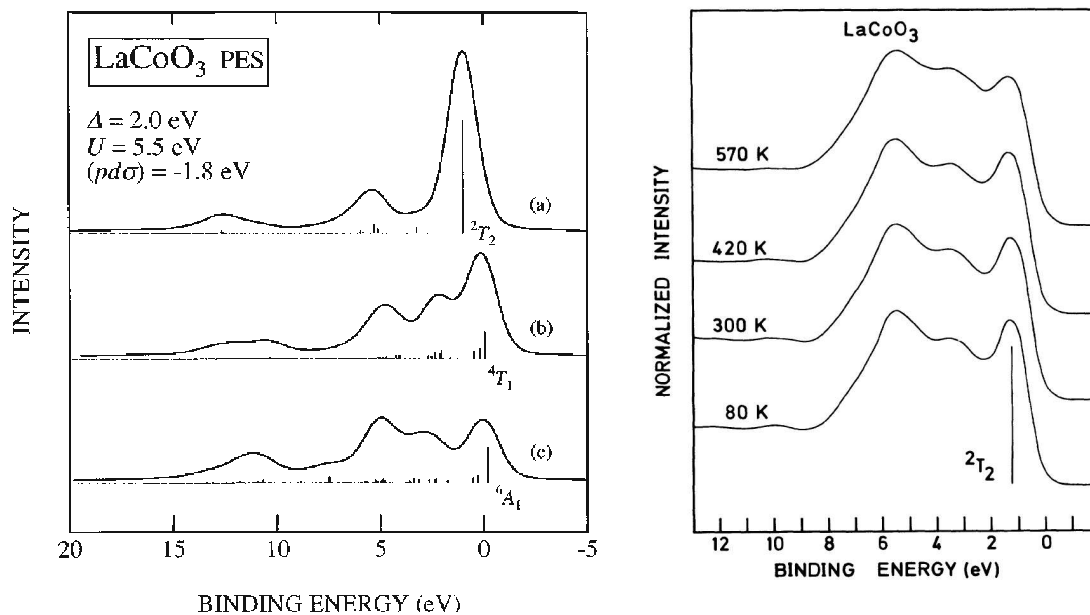
Figure 2.4: Left: Calculated Co $3d$ photoemission spectra of $LaCoO_3$ assuming the (a) LS, (b) IS, and (c) HS initial states within the full–multiplet configuration–interaction cluster model (from Saitoh *et al.* [48]). Right: Valence band x–ray photoelectron spectra of $LaCoO_3$ taken at different temperatures (from Abbate *et al.* [41]).

photoemission study by Abbate *et al.* in the temperature range up to 570 K shown in the right panel of figure 2.4, hardly display any temperature dependence below 420 K, suggesting that the system remains in the same spin state all the way up to this temperature, interpreted as the LS [41]. This result clearly contradicts the finding of a finite magnetic susceptibility at temperatures down to at least 50 K, see figure 2.1. Moreover, the expected dominant peak at low binding energies in the low–spin spectrum is not observed. Also many other photoemission studies do not show such a peak [39, 40, 48, 58–60]. This is very puzzling, and to make things worse, the experimental spectra show in fact a striking resemblance with the calculation for the HS.

Considering, on the one hand, the known problem of surface sensitivity in PES, which is particularly important for correlated systems, and, on the other hand, the small energy separation between the spin states in the case of $LaCoO_3$, the question arises whether the surface could take a different spin state than the bulk [58, 61]. Looking at the energy level diagram of the simple ionic model in figure 2.2 it is evident, that a reduction of the crystal field at the surface of the order 100 meV will definitely drive the system in the HS. In order to clarify the role of the surface in the photoemission of $LaCoO_3$, we have carried out bulk sensitive measurements, and from the analysis of spectra of different degrees of surface sensitivity, we extract the bulk and surface electronic structure.

2.2   Experimental

Single crystals of LaCoO$_3$ have been grown and characterized by C. Zobel, using a floating zone mirror furnace [62]. In order to avoid excessive charging in the photoemission experiment at low temperatures, the samples were doped by 0.2% Sr. This doping level is so low that it has minimal effect on the magnetic properties: the magnetization curve still is very similar to that of undoped LaCoO$_3$. We were able to collect reliable photoemission spectra at temperatures down to 65 K using soft–x rays with energies in the 450 – 1000 eV range at beam line ID08 of the ESRF, Grenoble. The overall experimental resolution using a Scienta SES 2002 electron energy analyzer and a photon energy of 700 eV was set to 200 meV. For the calibration of binding energies, Fermi cut–off spectra of polycrystalline silver have been taken. Samples were cleaved *in–situ* and measured at normal emission and at an angle of 60° off normal at 65 K, 110 K and 300 K. In order certify the sample quality, core level PES in the O 1s and Co 2p regions, as well as x–ray absorption spectra on the Co–$L_{2,3}$ edge have been taken repeatedly. Surface contamination at low temperature detected in the core level spectra could be removed by heating the sample to 240 K for half an hour. The base pressure in the spectrometer chamber was in the low 10^{-10} mbar range throughout the measurements.

Additional measurements were performed using a VG twin–crystal monochromatized Al K_α x–ray source (hν = 1486.6 eV) and a Scienta SES 100 hemispherical electron energy analyzer at temperatures of 100 K and 300 K. The overall experimental energy resolution was set to 360 meV, and the base pressure was in the low 10^{-10} mbar range. The sample was first cleaved *in–situ* and measured at normal emission, in order to obtain the highest possible degree of bulk sensitivity, and subsequently scraped *in–situ* with a diamond file, simulating the conditions of previous studies. The sample quality was monitored by repeatedly measuring core level spectra, reproducibility has been checked several times. For calibration of binding energies, Fermi cut–off spectra of polycrystalline silver have been used.

Even more bulk sensitive photoemission spectra were taken at the ID16 beam line of the ESRF, Grenoble, using 6 keV photons and the VOLPE (an acronym for volume photoemission) spectrometer [63] in the temperature range of 70 – 300 K. At a photon energy of 5931 eV, the overall experimental resolution was set to 365 meV. The pressure was below 5×10^{-9} mbar throughout the experiment. The sample was cleaved *in–situ* and measured at normal emission. The 300 K spectra before and after the low temperature measurement proved to be reproducible. As an energy calibration we used a Fermi cut–off spectrum of a polycrystalline gold sample at room temperature and reference spectra of the Au 4f core levels every few hours to correct for energy drifts. The process of aging of the sample was monitored by repeated O 1s spectra alternating with the measurement of the valence band region. No significant changes during the entire experiment were observed.

2.3   Temperature dependence: bulk sensitive photoemission

The valence band spectra of $LaCoO_3$ taken with 700 eV photon energy at 65 and 300 K are shown in figure 2.5. The measurement geometry was chosen such that the sample faces the analyzer, i. e. oriented to normal emission. The angle between the surface normal and the beam is 35° by construction of the chamber. We would like to emphasize two decisive differences between our spectra and the previously published results. First of all, we observe a distinctively different line shape, characterized by a dominant and sharp peak at 0.8 eV binding energy. In comparison with the cluster model calculations, we notice that this feature corresponds to the LS spectral weight, in agreement with the assumption of a LS ground state at low temperature according to the magnetic susceptibility. Secondly, this feature displays a weak but clear temperature dependence, consistent with current models of a spin state transition in this temperature range from predominantly LS at low temperature to a thermally populated higher spin state.
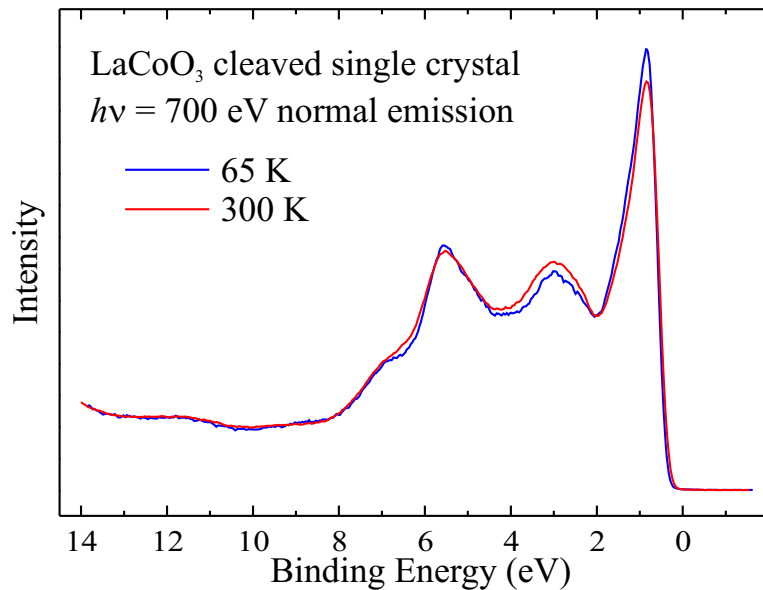
Figure 2.5: Valence band photoemission spectra of a cleaved $LaCoO_3$ single crystal at 65 K (blue line) and 300 K (red), taken at normal emission using 700 eV photon energy.

Our results show distinctive differences to the literature data, and we suspect that the issue of surface sensitivity is the reason for this discrepancy. As was pointed out above, we have taken much care about bulk sensitivity in our experiment, by choosing high photon energies, thus providing a large enough escape depth of the photoelectrons due to the higher kinetic energies, using high quality single crystals cleaved *in–situ* and measured at normal emission. Still we expect to see an appreciable surface contribution in our spectra taken at 700 eV photon energy. In order to maximize the bulk signal, it is preferable to use the highest possible photon energies, since this would provide an extremely large escape depth. The recent
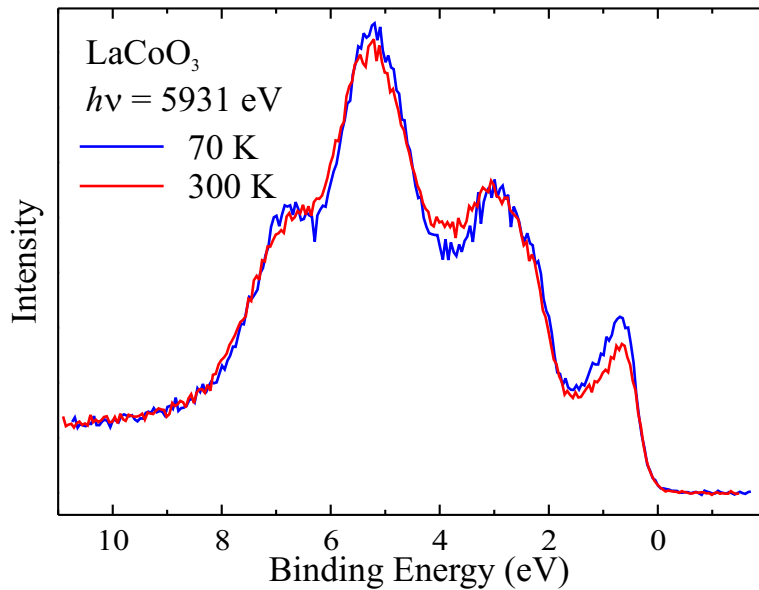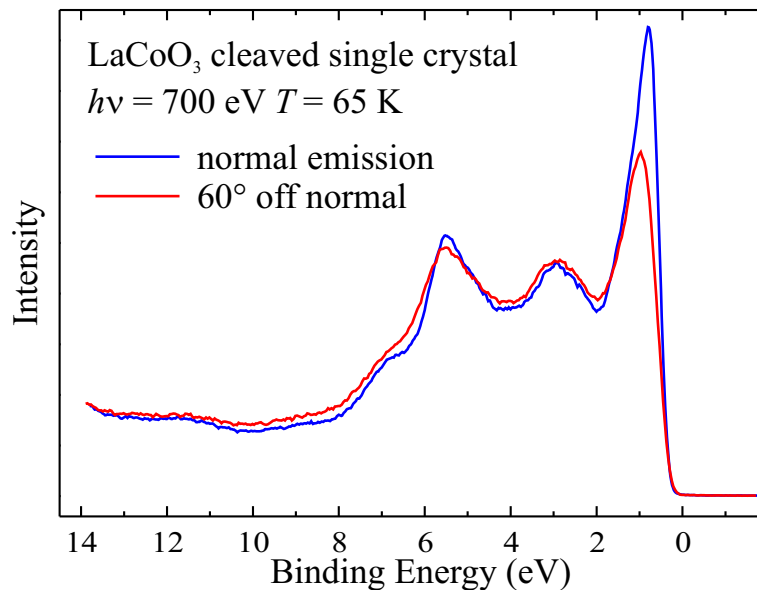
Figure 2.6: Valence band photoemission spectra of a cleaved LaCoO$_3$ single crystal taken with 5931 eV photon energy at normal emission at 70 K (blue line) and 300 K (red).

progress in the field of HAXPES permits the use of photon energies of several keV with reasonable resolution and escape depths of more than 50 Å, thus reducing the surface contribution to the total photoemission intensity to a few percent [64, 65]. In figure 2.6, the valence band spectra of LaCoO$_3$ are shown, taken with a photon energy of 5931 eV at 70 K and room temperature. First of all we note a strongly modified line shape as compared to the spectra taken at 700 eV photon energy, see figure 2.5. We discuss the photon energy dependence in a later section, and focus at the moment on the temperature dependence of the spectra. Consistent with the spectra taken with 700 eV photon energy, we again observe a clear temperature dependence primarily in the low binding energy range up to 2 eV, which corresponds to LS spectral weight. The decrease in this peak from 70 K to 300 K is, however, much more pronounced than in the lower photon energy spectra. We relate this observation to the higher degree of bulk sensitivity in the spectra taken with 6 keV, indicating that the transition from LS to a higher spin state is a property of the bulk and absent at the surface. This could explain why the previously published results did not observe a temperature dependence below room temperature, if they were dominated by the surface contribution. Besides, it suggests that the different line shapes of the literature spectra and ours could be due to a different spin state at the surface as compared to the bulk. We will investigate this conjecture extensively in the following sections.

2.4   Emission angle dependence: unraveling the bulk and surface contributions

As we have seen above, the issue of bulk sensitivity plays a major role in the interpretation of the photoemission results of $LaCoO_3$. From the truly bulk sensitive spectra taken at high photon energy, however, a precise determination of the spin states, or the weight of excited spin states in the spectrum, is inhibited by the low Co $3d$ signal as compared to the large oxygen background. Therefore, we try to extract the bulk contribution from the lower photon energy spectra by subtraction of the surface contribution. For this purpose, we have performed emission angle dependent measurements with a photon energy of 700 eV in the temperature range of 65 – 300 K. As was discussed in chapter 1, the surface contribution to the spectrum is considerably enhanced for emission angles far away from the sample surface normal. In figure 2.7, we show the valence band spectra of $LaCoO_3$ at 65 K taken at normal emission and at an angle of 60° off normal. We observe a dramatic decrease in intensity of the 0.8 eV binding energy LS peak in the spectrum taken at grazing emission as compared to normal emission. Indeed, this result confirms the assumption made above, that the surface contribution is different from the bulk.

Figure 2.7: Valence band photoemission spectra of a cleaved $LaCoO_3$ single crystal taken at 65 K with 700 eV photon energy at normal emission (blue line) and at 60° off normal (red).

In order separate the bulk and surface contributions in the spectra, we subtract the more surface sensitive grazing emission spectrum with a suitable weight from the more bulk sensitive normal emission spectrum. The choice of the weight is determined by the ratio of the surface and bulk contributions in the spectra. For a quantitative analysis, we have to consider the photoemission intensity at a given

energy and an emission angle θ as the integral over the probing volume,

$$
\begin{aligned}
I(\theta) &= \int_0^\infty \rho(z)\mathrm{e}^{-\frac{z}{\lambda\cos\theta}}\,\mathrm{d}z \\
&= \lambda\cos\theta\left(\rho_\mathrm{s}(1-\mathrm{e}^{-\frac{a}{\lambda\cos\theta}}) + \rho_\mathrm{b}\mathrm{e}^{-\frac{a}{\lambda\cos\theta}}\right),
\end{aligned}
\tag{2.1}
$$

with the escape depth λ as defined in (1.8), the thickness of the surface layer approximated by the lattice constant a, the energy dependent spectral density ρ, and the respective surface and bulk contributions ρ_s and ρ_b. Note that the intensities integrated over binding energy are proportional to the cosine of the emission angle due to the larger attenuation in grazing emission, which has to be corrected for in the subtraction of the spectra *normalized* to the integral. Since in the present setup the angle of the surface normal to the beam is almost the same for normal and grazing emission, a correction for the projected light spot size on the sample surface can be neglected. With the emission angles $\theta = 0$ and $60°$, we find from (2.1) for the intensities of the normalized spectra in normal (N/E) and grazing emission (G/E), respectively,

$$
I_\mathrm{N/E} = \quad I(0) \quad = \lambda\rho_\mathrm{s}(1-\mathrm{e}^{-\frac{a}{\lambda}}) + \lambda\rho_\mathrm{b}\mathrm{e}^{-\frac{a}{\lambda}}
\tag{2.2}
$$

$$
I_\mathrm{G/E} = \quad 2I(60°) \quad = \lambda\rho_\mathrm{s}(1-\mathrm{e}^{-\frac{2a}{\lambda}}) + \lambda\rho_\mathrm{b}\mathrm{e}^{-\frac{2a}{\lambda}}.
\tag{2.3}
$$

This means that we can extract the true bulk and surface contributions by suitable subtractions of the normal and grazing emission spectra,

$$
\begin{aligned}
I_\mathrm{N/E} - \gamma I_\mathrm{G/E} &= \frac{\lambda}{1+\mathrm{e}^{\frac{a}{\lambda}}}\rho_\mathrm{b} \\
I_\mathrm{G/E} - \delta I_\mathrm{N/E} &= \lambda(1-\mathrm{e}^{-\frac{a}{\lambda}})\rho_\mathrm{s},
\end{aligned}
$$

with the weights $\gamma = \frac{1-\mathrm{e}^{-\frac{a}{\lambda}}}{1-\mathrm{e}^{-\frac{2a}{\lambda}}}$ and $\delta = \mathrm{e}^{-\frac{a}{\lambda}}$, according to (2.1 - 2.3). Assuming reasonable values of $a \approx 4$ Å for LaCoO$_3$ and $\lambda \approx 8$ Å at 700 eV photon energy, we find $\gamma \approx \delta \approx 0.6$. The results of corresponding difference spectra for 65 K, 110 K and 300 K are shown in figure 2.8. First of all, we notice in the bulk contribution, shown in the top panel, an even enhanced intensity at the 0.8 eV binding energy LS peak as compared to the raw data (see figure 2.5). The temperature dependence also is significantly more pronounced, in line with the assumption that the surface contribution is temperature independent. This is confirmed by the difference spectra in the bottom panel of figure 2.8 corresponding to the surface contribution, which show hardly any temperature dependence. The surface and bulk contributions display distinctively different line shapes, not only in the low binding energy range attributed to the LS peak. Comparison with the cluster calculations shown in figure 2.4 strongly suggests that the bulk spectrum is dominated by the LS, with an increasing contribution of higher spin states with temperature, while the surface spectrum very well agrees with the calculations of the HS. The experimental results of previous investigations clearly match to the surface spectra, not only in line shape, but also in the fact that they do not show temperature dependence. We
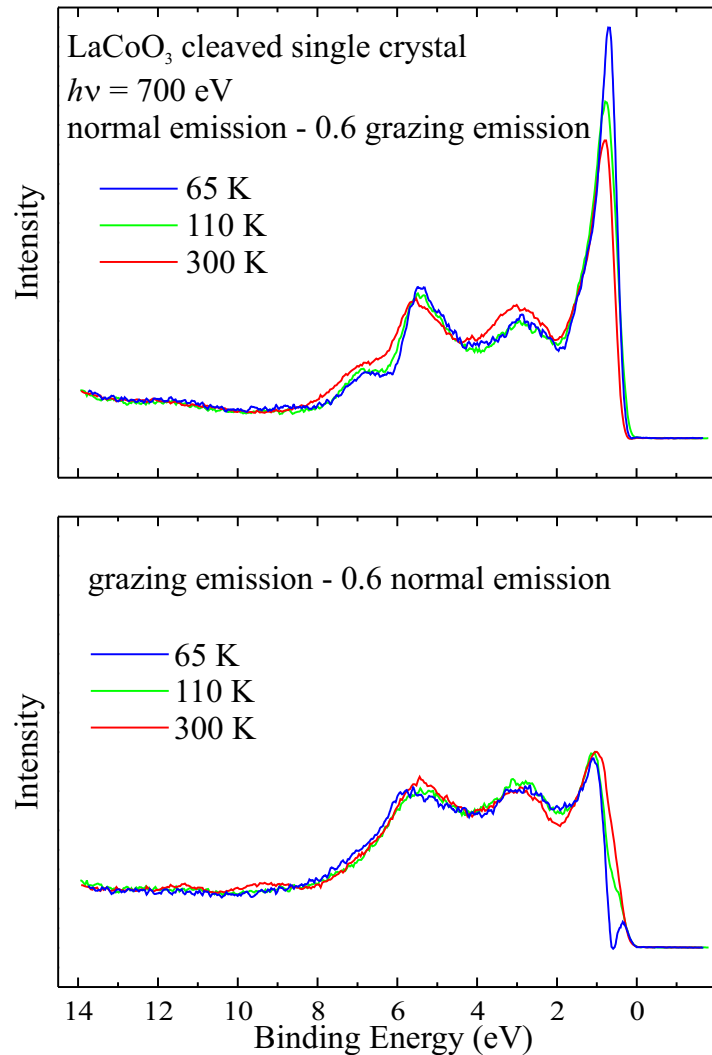
Figure 2.8: Difference spectra of the valence band spectra of LaCoO$_3$ taken at 65 K (blue lines), 110 K (green) and 300 K (red) with 700 eV photon energy. Top: difference of normal emission spectra and grazing emission spectra with a weight of 0.6, corresponding to the bulk contribution. Bottom: difference of grazing emission spectra and normal emission spectra with a weight of 0.6, corresponding to the surface contribution.

thus find our initial assumption verified, that the surface is in a different spin state than the bulk, independent of temperature, and that the spectra in the literature mostly show this surface contribution.

We have checked that the results are hardly affected by energy shifts and also depend only weakly on the particular choice of the weights γ and δ. We attribute the odd line shape at low binding energies ≤ 0.6 eV in the 65 K surface contribution difference spectrum to difficulties in the energy calibration and problems due to broadening of the surface sensitive grazing emission spectra. This effect is also seen in the 110 K difference spectrum, but less clear. Nevertheless, our conclusions are not affected. Note also, that the difference spectra contain an ill defined amount of oxygen spectral weight. This however is assumed to be hardly temperature dependent on the one hand, and to be the same at the surface and in the bulk, on the other hand, such that it is supposed to have no influence on the conclusions either. Moreover, the photoionization cross section of O $2p$ is more than an order of magnitude smaller than for Co $3d$ at a photon energy of 700 eV [66], such that the total oxygen contribution has only little weight in the spectra.

2.5   Importance of surface treatment

We have repeated the temperature dependent photoemission investigation of LaCoO$_3$ using Al K_α radiation ($h\nu = 1486.6$ eV). The results for 100 K and 300 K, shown in figure 2.9, qualitatively agree with the 700 eV spectra, in particular a pronounced sharp peak at 0.8 eV binding energy is observed, which loses intensity with increasing temperature, and thus can be identified with Co 3d LS spectral weight. The
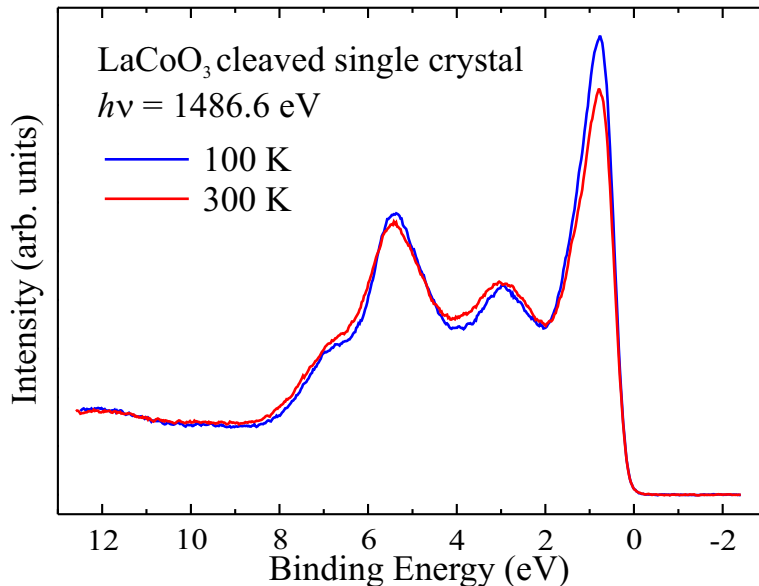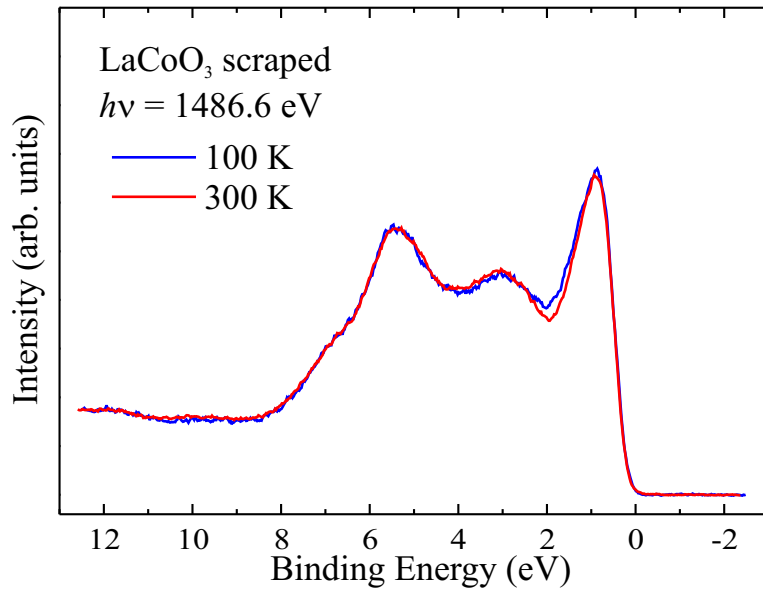

Figure 2.9: Valence band Photoemission spectra of a cleaved LaCoO$_3$ single crystal at 100 K (blue line) and 300 K (red) taken at normal emission with 1486.6 eV photon energy.

assumption of an enhanced bulk sensitivity due to the larger escape depth at the photon energy of 1486.6 eV as compared to 700 eV is verified by the more pronounced temperature dependence of the spectra, since the surface contribution, according to the results of the previous section, is temperature independent. Another interesting difference to the 700 eV spectra is the reduced spectral weight at the 3 eV binding energy peak. This remarkable photon energy dependence of the spectral line shape will be addressed in detail later on.

An issue to be investigated is the significant difference between our spectra and the large number of mostly consistent results in the literature, obtained under seemingly similar experimental conditions [39–41, 48, 58, 59]. While it is well known that low photon energy spectra may give misleading results due to the small escape depth of the photoelectrons, the measurements in the literature quoted here were mostly taken with Al K_α or Mg K_α ($h\nu = 1253.6$ eV) radiation and should therefore result in a comparable escape depth as in our experiment. There are however two decisive factors, that distinguish our approach from previous ones. On the one hand, the sharp Co 3d LS peak suffers considerably from low experimental resolution of order of 1 eV, as was standard up to ten years ago. This would lead to a general broadening of the spectra with respect to our results, but it still cannot explain the observed discrepancies completely. On the other hand, especially the earliest studies

have not taken much care about the surface preparation of their samples. In most cases, polycrystalline samples were used, providing badly defined surfaces of large area from the outset. As a surface treatment, if any, the samples were simply either annealed [39, 58], or scraped *in–situ* [40, 48, 59], to remove surface contamination.

In order to check whether we can reproduce the literature results, we simulated their experimental conditions by scraping our sample *in–situ* after it had been measured with a cleaved surface. In figure 2.10, the spectra taken at 100 K and 300 K are shown, which can be directly compared to the results taken of the same sample with a cleaved surface, shown in figure 2.9. First of all, we note that the characteristic Co


Figure 2.10: Valence band Photoemission spectra of $LaCoO_3$ at 100 K (blue line) and 300 K (red) after scraping the surface, taken in normal emission at 1486.6 eV photon energy. The sample is the same as the one used for the spectra shown in figure 2.9.

$3d$ LS peak at 0.8 eV binding energy has substantially lost weight as compared to the cleaved spectra. Considering the poor resolution of most older literature results, we find a convincing agreement with the spectra of the scraped surface. In particular, the reported temperature independence of the spectra below room temperature [41] is reproduced in the scraped spectra. This means, as we spoil the bulk sensitivity by increasing the surface area, we can resolve the discrepancy between the literature results and ours, indicating the poor bulk sensitivity of the published data. This also means, that the significance of the previous analyses has to be put into question.

2.6 Ionic considerations on the spin state at the surface

As the previous sections have shown, the electronic structure of $LaCoO_3$ is remarkably different from surface to bulk. The bulk contribution has been shown to be temperature dependent between 65 K and room temperature, but within this range

$$E$$

x^2-y^2		$6Dq$
$3z^2$-r^2		$6Dq$ - Δ_{e_g}
xy		$-4Dq$
yz,zx		$-4Dq$ - $\Delta_{t_{2g}}$

$3d$ $10Dq$ Δ_{e_g} $\Delta_{t_{2g}}$
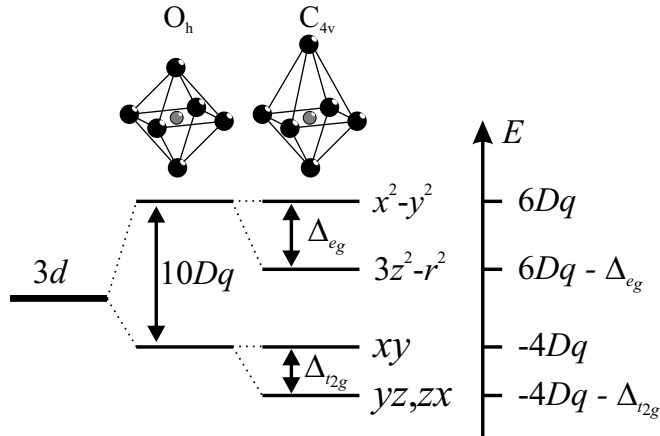
Spin State of lowest $3d^6$ configuration ($10Dq = 2J_H$):

$\Delta_{t_{2g}}/J_H$

LS

IS

HS

1

1   Δ_{e_g}/J_H
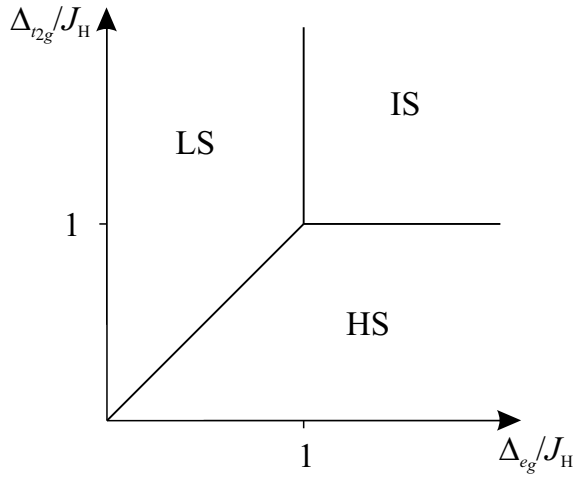
Figure 2.11: Top: energy level diagram for $3d$ electrons in a cubic crystal field $10Dq$ with additional splitting of e_g and t_{2g} levels at the surface given by Δ_{e_g} and $\Delta_{t_{2g}}$, respectively. The sketches show the arrangement of the ions in the bulk CoO$_6$ octahedron (O_h symmetry) and the distorted surface cluster (C_{4v} symmetry), oxygen represented by big black spheres, cobalt by small grey ones. Bottom: resulting phase diagram of the surface spin state for the lowest $3d^6$ configuration in the ionic model at the crossing point $10Dq = 2J_H$.

dominated by the LS. The surface, in contrast, is temperature independent and does not appear to possess a large LS contribution. The surface layer tends to lose oxygen, thus possibly creating Co^{2+} sites which usually take a HS. This effect, however, cannot be quantified reliably from the spectra, and therefore will not be discussed here. On the other hand, a relaxed surface Co–O bond length results in a modified crystal field at the cobalt site, which is expected to have a significant influence on the spin state of the Co^{3+} ions. Whether the spin state at the surface is predominantly HS or IS, cannot be determined unambiguously from the spectra, although the results exhibit an outstanding resemblance to the calculations for the HS, see figure 2.4. This means, in order to resolve the surface spin state, we have to look more carefully to the details of the model calculations.

First of all, we note that from the ionic energy level diagram shown in figure 2.2, the crystal field is somehow effectively reduced at the surface with respect to the bulk value, since in the opposite case, the LS would be even stabilized. As we have discussed above, the model of an isolated ion in a cubic crystal field would result in a HS is this case, but may be unreliable due to the different local symmetry of the Co ion at the surface. For that purpose we consider a modified model consisting of a Co^{3+} ion surrounded by six O^{2-} ions, but now with one of them, namely the top–apical oxygen, having a somewhat larger Co–O bond length than the other

ones, see sketch in figure 2.11. As a result, the electrostatic repulsion of the Co $3d$ orbitals pointing towards the apical oxygen, will be reduced, and the energies of the respective orbitals are lowered. We take this into account by introducing parameters Δ_{e_g} and $\Delta_{t_{2g}}$, which act on the $3z^2 - r^2$ and yz, zx orbitals, respectively, as shown in the corresponding energy level diagram in figure 2.11. Assuming the cubic crystal field splitting to be close to the crossing point $10Dq = 2J_{\mathrm{H}}$, i.e. in the case of degeneracy of the HS and LS, the energy difference between the two is $\Delta_{t_{2g}} - \Delta_{e_g}$, between IS and the LS it is $J_{\mathrm{H}} - \Delta_{e_g}$, and between IS and HS $J_{\mathrm{H}} - \Delta_{t_{2g}}$. As a result, the HS becomes stabilized for $\Delta_{t_{2g}} < \Delta_{e_g} \wedge J_{\mathrm{H}}$, and the IS for $J_{\mathrm{H}} < \Delta_{e_g} \wedge \Delta_{t_{2g}}$, as illustrated by the phase diagram in figure 2.11. To make a first statement, it is quite unlikely that the low symmetry crystal field energy gain $\Delta_{t_{2g}}$ for the t_{2g} orbitals would be greater than $J_{\mathrm{H}} \approx 0.7$ eV. This means that an IS at the surface will not be supported by the ionic model. The second statement which we can make is that it is quite natural that the low symmetry crystal field splitting for the e_g orbitals is larger than for the t_{2g} since the $3z^2 - r^2$ orbital is pointing more to the apical oxygen than the yz/zx orbitals. The immediate implication of $\Delta_{e_g} > \Delta_{t_{2g}}$ is that the Co ion at the surface will be HS if the Co ion in the bulk is at the degeneracy crossing of LS/HS.

2.7   Photon energy dependence

The choice of photon energy determines the results of a photoemission experiment in several ways. On the one hand, as was emphasized before, the escape depth of the photoelectron depends on their kinetic energy, therefore the degree of bulk sensitivity changes as a function of photon energy, in general increasing with it. On the other hand, photoionization cross sections are energy dependent, which means that the weights of specific elements or orbitals change differently with photon energy, and as a result the sensitivity of the spectra to the respective element or orbital can be suppressed or enhanced. In principle, all cross sections go down with rising energy, however, the results of atomic calculations show that the O $2p$ cross section is expected to decrease more steeply than the cross sections of transition metal $3d$ electrons [66, 67]. Thus, the sensitivity of valence band PES to the transition metal contribution is assumed to increase with photon energy, which is considered advantageous in most cases. Note that in special cases of resonant conditions, cross sections can be anomalously enhanced, such that the general relations may not hold anymore, but this occurrence is restricted to very narrow energy ranges only, and is not considered in this section.

The valence band PES taken at 65 K with photon energies of 450 eV, 700 eV and 1000 eV are shown in figure 2.12. For comparison, the 450 eV and 700 eV spectra have been broadened with a Gaussian of FWHM of 250 meV and 215 meV, respectively, in order to account for the smaller line width of the 450 and 700 eV photons as compared to the 1000 eV photons. We have made these broadenings in order to obtain similar effective overall experimental resolution when comparing the data. The spectra show significant changes with photon energy, especially the 450 eV spectrum shows enhanced intensity in the strong peak at 0.8 eV binding energy,
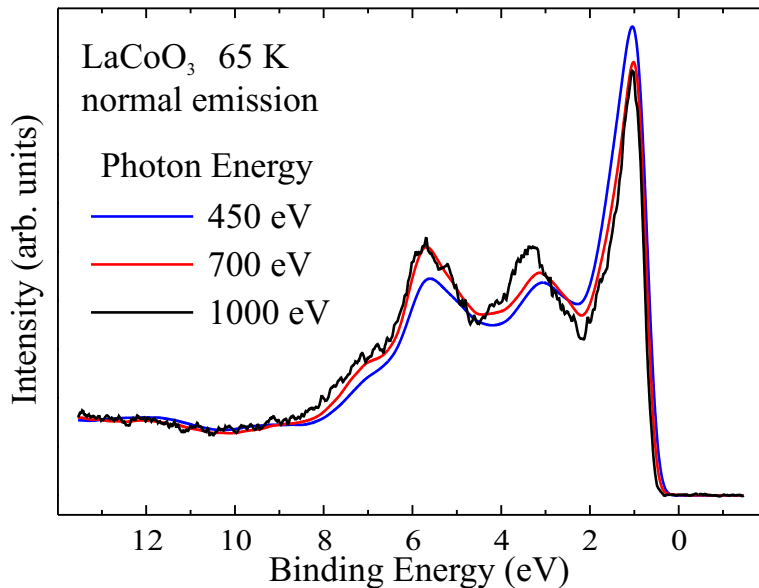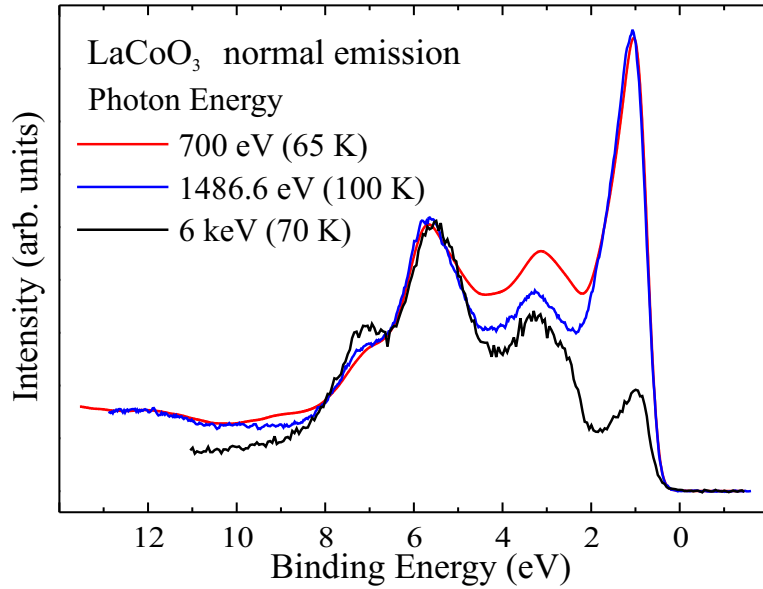
Figure 2.12: Valence band photoemission spectra of LaCoO$_3$ at 65 K taken at normal emission with 450 eV (blue), 700 eV (red) and 1000 eV (black) photon energy. For comparison, the 450 eV and 700 eV spectra were broadened with a Gaussian of FWHM of 250 meV and 215 meV, respectively.

corresponding to Co 3d LS weight. This is opposite to the expectation that the lower the photon energy, the less sensitive one is to the Co 3d spectral weight, and the more sensitive to the surface which has no LS main peak at 0.8 eV. Moreover, the line shapes of the 700 eV and 1000 eV spectra are rather similar, except for the region of 3 – 4 eV binding energy, i.e., not showing an increased LS 0.8 eV peak intensity for the higher photon energy. We infer that the cross sections do not follow the predictions of the atomic calculations.

As a next step, we consider even higher photon energies. In figure 2.13, we show the spectra taken at 700 eV together with the 100 K spectra taken with Al K_α radiation ($h\nu = 1486.6$ eV), and 70 K spectra taken at 6 keV excitation energy. These latter two spectra were taken with an almost identical experimental resolution of 360 meV, therefore the 700 eV spectrum was broadened by a Gaussian of FWHM of 300 meV. For comparison, all spectra are scaled to the peak at 5.6 eV binding energy. The line shapes show in this range an extreme photon energy dependence, in particular the 6 keV spectrum displays a largely suppressed Co 3d LS peak as compared to the lower energy spectra, in gross contrast to the expectation. Calculations of cross sections predict a gain of four orders of magnitude in the sensitivity to Co 3d over O 2p from 1 to 6 keV photon energy [67]. This implies that the calculations for the photoionization cross sections cannot be correct. Although we assume that the observed valence band spectrum is to be built up from the Co 3d and O 2p spectral weights only, there is also the possibility that other orbitals may show up at 6 keV while being invisible at lower photon energies. There are reports [64, 65] that the photoionization cross section of the transition metal 4s becomes more pronounced for hard x–rays relative to the 3d orbitals. This may mean that we have to seriously

Figure 2.13: Valence band photoemission spectra of $LaCoO_3$ taken at normal emission with 700 eV photon energy at 65 K (red), 1486.6 eV and 100 K (blue), as well as 6 keV and 70 K (black). The 700 eV spectrum was broadened with a Gaussian of FWHM 300 meV to account for the better resolution. All spectra are scaled to the peak at 5.6 eV binding energy for comparison.

consider the contribution of Co $4s$ to the valence band spectrum taken at 6 keV. To test these ideas, we have performed very recently 7.7 keV experiments on Cu_2O and ZnO. These materials are simple band semiconductors and may therefore serve as model systems. The analysis of the spectra is in progress.

2.8   Conclusions

We have addressed the issue of the relation between the bulk and surface electronic structures of $LaCoO_3$ with a detailed PES study in the range from 65 K to room temperature, using photon energies between 450 eV and 6 keV and varying degrees of surface sensitivity. We observe a prominent low binding energy peak showing a clear temperature dependence. This can be connected to the LS character of $LaCoO_3$ at low temperatures. By contrast, these features are not present in previously published results of various groups. We can show that the literature results are not representative for the bulk material.

By analyzing the emission angle dependence of the spectra, we have been able to separate the bulk and surface contributions. The bulk spectrum shows the characteristic LS peak with a temperature dependence in agreement with magnetic susceptibility data. At the same time, the surface spectrum is temperature independent. We infer that the Co ions at the surface are in the HS state.

The valence–band spectra taken at different photon energies exhibit surprising cross section effects contradictory to predictions of the widely accepted *atomic* calculations. The results clearly demonstrate the need to redo the calculations for the

photoionization cross sections using perhaps wave functions which are more realistic for a solid state system. This is particularly important for the young field of hard x–ray photoemission.

Chapter 3

Metal–Insulator Transition in VO_2: New insight from bulk sensitive electron spectroscopies

Partly published in Phys. Rev. Letters 97, 116402 (2006) [68]

3.1 Introduction

VO_2 forms an important benchmark problem for solid state physics [6, 69, 70]. It has been known for decades to show a dramatic drop in the resistivity of five orders of magnitude at $T_{\mathrm{MIT}} = 340$ K, referred to as a metal–to–insulator transition (MIT), see figure 3.1 [71–73]. The crystal lattice is shown in figure 3.2 left. At high temperature, the system takes the orthorhombic rutile (TiO_2) structure and is metallic, as expected from one–electron theory for a $3d^1$ configuration of vanadium with the formal valence 4+. In this so–called R phase, vanadium ions are octahedrally surrounded by six oxygen ions and form chains of edge sharing octahedra along the crystallographic c axis. Crossing the transition, the crystal undergoes a structural distortion to the monoclinic M_1 phase, indicated by arrows in figure 3.2. The vanadium ions form pairs along the chains and these *dimers* incline from the c axis in a zig–zag pattern. In turn, the periodicity of the crystal lattice is doubled along the c axis, which can induce a MIT according to the Peierls mechanism in one–electron theory [74]. In order to make this mechanism work in VO_2, the lowest d level must be non–degenerate, i.e. half filled in the metallic phase, and consequently becomes completely filled and insulating when it splits due to the Peierls distortion. The $3d$ levels split in a cubic crystal field into twofold degenerate e_g^σ and lower lying threefold degenerate t_{2g} states. In the R phase, the tetragonal crystal field further splits the t_{2g} levels into a low lying a_{1g} and higher lying e_g^π orbitals. Hence the lowest level is non–degenerate, and moreover possesses a distinctive polarization parallel to the bonding axis. This makes the chains particularly unstable against a Peierls transition.

Still, the simple one–band model does not appear to represent an appropriate description of VO_2, as it fails to explain a number of details of the electronic properties. First of all, the resistivity of a single occupied a_{1g} band is supposed to be
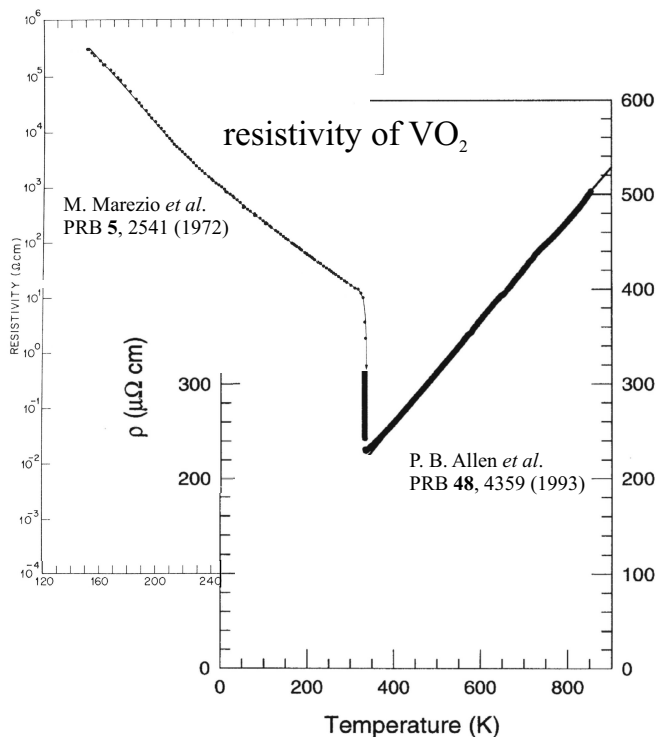
Figure 3.1: The resistivity of VO_2 as a function of temperature shows a jump of several orders of magnitude and a change of sign in the slope at $T_{MIT} = 340$ K. Figure composed of the measurements of Marezio *et al.* for $T \leq T_{MIT}$ [72] and of Allen *et al.* for $T \geq T_{MIT}$ [73]. Note the logarithmic scale in the low temperature data in contrast to the high temperature part.

rather anisotropic, in contrast to experimental results [76]. This indicates the occupation of e_g^π states in the metallic phase which consequently must be overlapping with the a_{1g} levels. Goodenough proposed a modified band structure model taking into account this overlap [69]. Here, the direct cation–cation–interaction is assumed to drive the MIT [77]. The energy level diagram is shown in figure 3.2 (a) for the metallic R phase, and (b) for the insulating M_1 phase. In the metallic phase, the a_{1g} and e_g^π levels, for which we will from now on adopt Goodenough's notation $d_\parallel$ and π^*, respectively, overlap and form a narrow but metallic conduction band. Due to strong hybridization of the $d_\parallel$ orbitals on neighbouring vanadium ions along the chains, a molecular orbital singlet can be formed locally on a pair, resulting in the experimentally observed dimerization in the insulating phase. The $d_\parallel$ band splits into the bonding and antibonding subbands, however, in order to open a gap in the low temperature phase, Goodenough pointed out the importance of an antiferroelectric distortion accompanied with the zig–zag–pattern in the M_1 phase. As a consequence of this distortion, the hybridization of the π^* orbitals with the neighbouring oxygen ions is increased. Since these are antibonding states, their energies will be raised, such that, according to Goodenough's model, the overlap with the occupied $d_\parallel$ states is suppressed and the gap opens.

While these Peierls–like models are conceptually beautiful [78, 79], it is somehow sobering to discover that band structure calculations based on the density functional theory in the local density approximation, cannot produce a gap for the M_1 phase. These calculations take fully into account the lattice displacements and the corresponding changes in the transfer integrals as well as the doubling of the unit cell. Apparently, the distortions are not strong enough to create a band gap. Doubts about this model of non–interacting particles also arose when the occurrence of two more structural phases M_2 and T with unexpected magnetic properties was observed
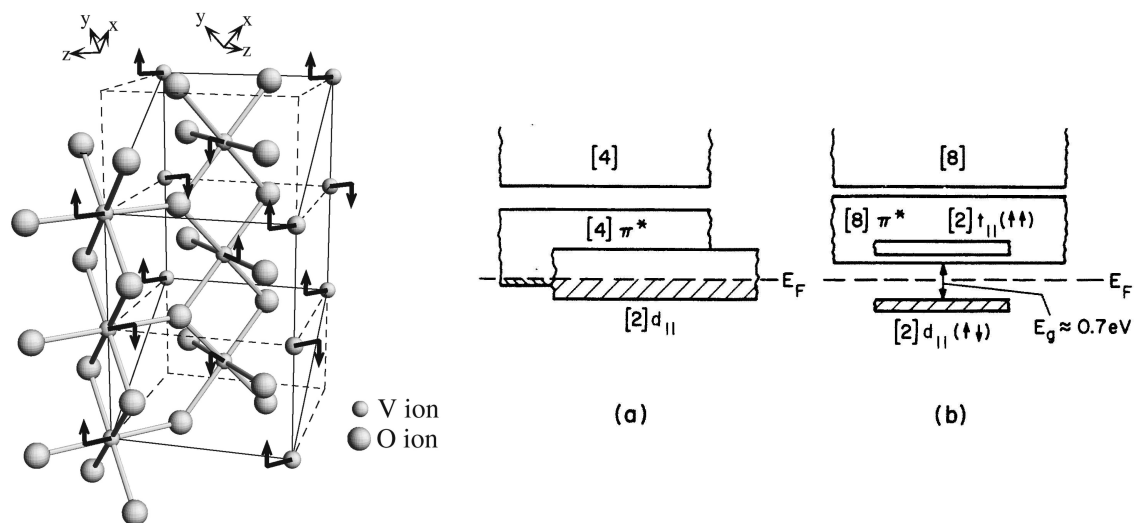
Figure 3.2: Left: The crystal lattice of VO_2: small spheres represent vanadium ions, big ones oxygen. Displacements of vanadium ions in the M_1 phase are indicated by arrows, edges of the corresponding unit cell by solid lines (from Tanaka [75]). Right: Energy level diagram of the Goodenough band–structure model in (a) the metallic R phase, and (b) the insulating M_1 phase [69].

upon either doping, e. g. with chromium, or application of uniaxial pressure in [110] direction [72, 80]. Pure VO_2 at ambient conditions is regarded as non–magnetic as it shows only a small and temperature independent Van–Vleck susceptibility in the insulating phase. The magnetism in the insulating M_2 and T phases, however, suggests localized V $3d$ moments and therefore cannot be described by one–electron theory. It was argued, that the total energies of the alternative insulating phases M_2 and T must be close to that of the M_1 phase, as very little doping, or low pressure, is already sufficient to stabilize them [80, 81]. Therefore, the strong influence of correlation effects present in these phases is assumed to exists also in the non–magnetic M_1 phase. The claim is then that the MIT should be regarded as essentially a Mott transition [82, 83]. Very recently, a twist to this debate is provided by a new study using cluster dynamical mean field theory (CDMFT) [28] asserting that both the singlet pairing and the strong Coulomb interactions are needed to open the gap.

One of the most direct methods to critically test the validity of the different models, is to determine the excitation spectrum associated with the introduction of an extra particle into the system [84]. Several direct–photoemission (PES) experiments have been reported in the literature [85–90], but surprisingly, none of the available spectra provides a satisfactory match with the calculated density of states [79, 91–94] or imaginary part of the Green's function [28, 94, 95]. The question arises whether the proper experimental spectrum still has to be collected, or whether none of the theories was able to catch the physics essential for the MIT of VO_2. Our objective is to obtain valence band and conduction band spectra which can be considered as truly representative of bulk VO_2, both below and above T_{MIT}.

3.2 Experimental

High quality single crystals of VO_2 were prepared by W. Reichelt using the chemical vapour transport technique [96]. Samples grow with natural specular [111] and less stable [110] surfaces. Clean surfaces for measurement have been obtained by post–cleaving. The samples were oriented with the c axis in plane, i. e. perpendicular to the x–ray beam.

High resolution, bulk sensitive photoemission spectra were taken at the ID08 beam line of ESRF in Grenoble. The crystals were cleaved *in-situ* exposing a [110] surface with an area of $\approx 3{\times}2$ mm^2. The probing depth is maximized by measuring at normal emission. The photon energy was set to 700 eV, sufficiently high to ensure bulk sensitivity [13, 18, 97]. The overall energy resolution was set to 0.16 eV and the Fermi level E_F was calibrated using a polycrystalline Ag reference sample. The angular acceptance of the Scienta SES 2002 electron energy analyzer is about $\pm\ 7°$, which covers more than one Brillouin Zone at 700 eV kinetic energy thereby yielding essentially angle-integrated spectra. Resonant photoemission at V–$2p$ resonance has been performed using the same setup. Core level, as well as lower resolution valence band spectra were taken in our Cologne laboratory with a VG twin crystal monochromatized Al K_α x–ray source ($h\nu$ = 1486.6 eV), and a Scienta SES 100 analyzer. For Fermi–level calibration, spectra of a polycrystalline silver sample were taken before and after the experiment, indicating the stability of the conditions during measurements within 50 meV. The experimental energy resolution with this setup was set to 370 meV. The pressure in the spectrometer chambers was kept in the low 10^{-10} mbar range throughout the experiment for both setups.

The XAS measurements were carried out at the ID08 beam line of the ESRF. VO_2 single crystals were mounted with the c axis perpendicular to the Poynting vector of the light. By either rotating the samples around the Poynting vector or changing the polarization of the beam from horizontal to vertical, the orientation of the electric field vector can be varied from $\vec{E}\|c$ to $\vec{E}\perp c$. This measurement geometry ensures that the optical path of the incoming beam is independent of the polarization, guaranteeing a reliable comparison of the spectral line shapes as a function of polarization. Bulk representative spectra were collected by using the total electron yield method on *in–situ* cleaved single crystals.

During measurement, the sample quality was checked repeatedly with either O–K XAS (at ESRF), or core level XPS (Cologne). We take the reproducibility of all spectra even for different crystals as a clear indication for the high quality of the samples and consequently the reliability of the data presented in this work.

3.3 Valence band

Figure 3.3 shows the valence band PES spectra of VO_2 taken at 300 and 348 K, i.e. below and above T_{MIT}. It can be clearly seen that the low temperature M_1 phase is an insulator with negligible spectral weight at E_F and that the high temperature R phase, by contrast, is a metal with an extremely high spectral weight at E_F. These spectra are quantitatively and qualitatively different from the ones published so far. Not only is the V $3d$ vs. O $2p$ spectral weight ratio larger than previously observed
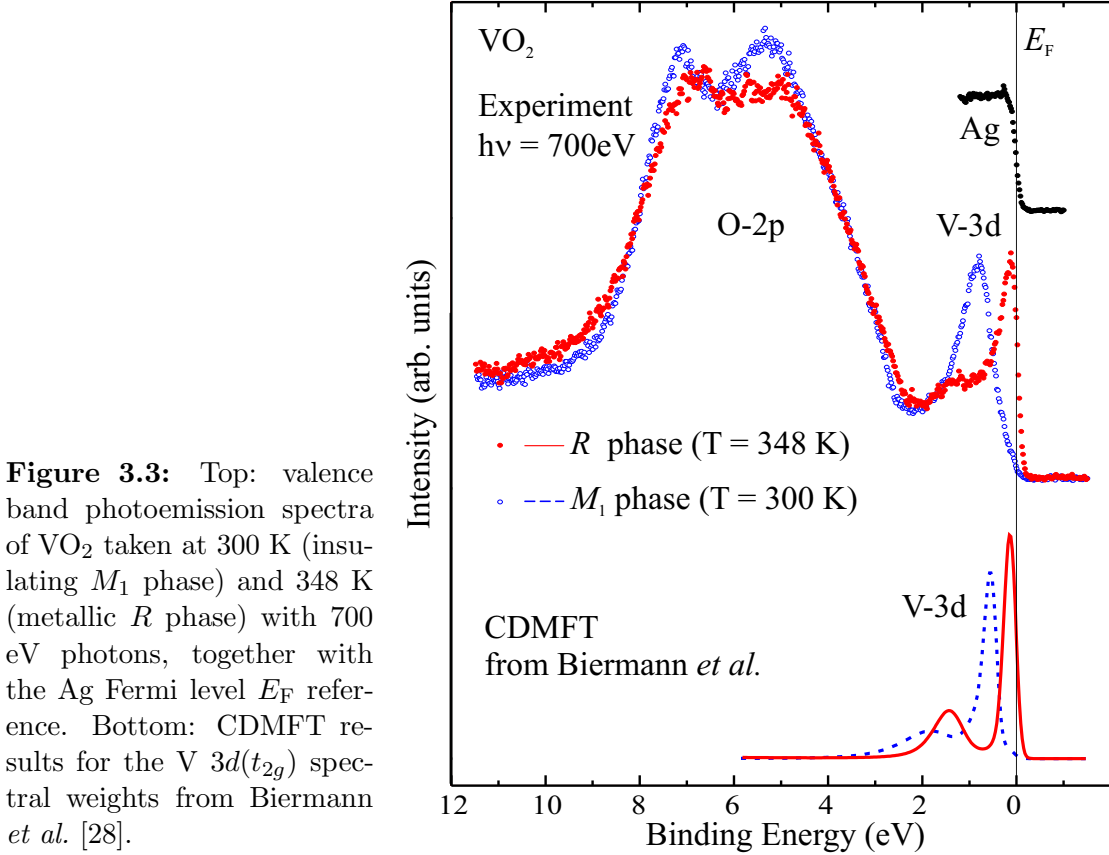
Figure 3.3: Top: valence band photoemission spectra of VO$_2$ taken at 300 K (insulating M_1 phase) and 348 K (metallic R phase) with 700 eV photons, together with the Ag Fermi level E_F reference. Bottom: CDMFT results for the V $3d(t_{2g})$ spectral weights from Biermann et al. [28].

thereby giving a clearer view on the most relevant states, but also the V $3d$ peak at 0.9 eV of the insulator is more resolved from the O $2p$ band [85–90].

Most important is, however, the exceptionally high peak at E_F of the metal together with the presence of a small but distinguishable satellite at 1.3 eV. This line shape has not been observed before [85–90]. It is also quantitatively different from the one taken under the V $2p \rightarrow 3d$ *resonance* conditions reported recently [98]. We notice that also our resonant PES spectra presented in the next section, have a smaller main peak to satellite ratio and larger widths than the *direct* PES spectrum of figure 3.3. This effect can be attributed to incoherent Auger emission accompanying resonant PES [99].

We also would like to point out that the satellite of the metal has a *different* energy than the main peak of the insulator. This shows that our samples are free from poor quality surfaces which could remain insulating above T_{MIT}. This in turn demonstrates that our spectra are indeed representative for the bulk [13].

In comparing the PES spectra with band structure calculations using the LDA method [79, 91, 93], we can see obvious discrepancies: these calculations always produce a metal, i.e. not only for the R but also for the M_1 phase. In addition, the gap between the V $3d$ and O $2p$ bands in the calculated density of states is not present in the experimental spectra. These aspects are direct indications for strong electron correlation effects in the material. Using the LDA+U approach [93, 94], the gap between the V $3d$ and O $2p$ bands disappears, and the spectral line shape of the M_1 phase becomes reasonably reproduced, but at the price that not only the M_1

but also the R phase are calculated to be insulators. Resorting to the LDA+DMFT method, one still finds unsatisfactorily metallic solutions for both phases if one assumes a realistic value of 4 eV for U [94]. It is nevertheless interesting to note that the satellites in the calculated R and M_1 spectra have energies close to that of the satellite in the experimental R phase and the main peak of the M_1 phase, respectively. This at least suggests that the parameters which define the energy positions are reasonably estimated, and that the problem rather lies in how to transfer the spectral weight more rapidly across the MIT [94].

To resolve this theoretical problem, Biermann *et al.* [28] attempted to include the k–dependence of the self–energy correction by implementing the CDMFT approach, in which the V–dimer is taken as the cluster. The underlying idea is that the essential part of the k–dependence can be found within these V–dimers when the material enters the insulating M_1 phase. We have reproduced their results [28] in figure 3.3 after multiplication with the Fermi function for 300 K and 348 K, respectively, and convolution with the experimental overall resolution of 0.16 eV. Comparison with our experimental spectra yields a very good agreement. The extremely high spectral weight at E_F as well as the satellite at 1.3 eV in the metallic R phase are well reproduced. Moreover, the insulating nature of the M_1 phase is now also well explained. The calculated position of the M_1 main peak is somewhat off from the experimental one, but this may be a matter of fine tuning the parameters. The small satellite in the CDMFT is not visible in the experimental spectrum as this is probably hidden by the intense O $2p$ band.

Important for the physics of the MIT in VO$_2$ is the finding that the insulator peak has a lower binding energy than the satellite of the metal. This suggests directly that the MIT cannot be described within the often used single–band Hubbard model, in which the satellite of the metal develops into the lower Hubbard band at equal or slightly higher energies when increased correlation effects turn the metal into an insulator [6]. This suggestion is further supported by the CDMFT which shows that the imaginary part of the self–energy does not diverge towards zero frequency. These findings strongly point out that another degree of freedom must play an important role. Very recently, polarization dependent XAS experiments on the V–$L_{2,3}$ edges revealed that in going from the metallic to the insulating state, the orbital occupation changes in a manner such that the material switches its electronic structure from 3–dimensional to effectively 1–dimensional [27]. This makes the system more susceptible to a Peierls–like transition. This orbital switching could also have a massive influence on the intersite exchange interactions with large consequences for the effective Hubbard U for nearest neighbor charge fluctuations [75, 100] and effective band widths [100].

3.4   Conduction band

We also carried out polarization dependent XAS measurements at the O–K edge. This technique is complementary to PES, since by probing the "unoccupied" O $2p$ partial density of states we in fact study the conduction band. Figure 3.4 depicts the spectra taken with the polarization vector $\vec{E}\|c$ and $\vec{E}\perp c$ at 300 and 348 K,

Figure 3.4: O–K x–ray absorption spectra (XAS) of VO$_2$ taken with the polarization vector $\vec{E}\|c$ (solid lines) and $\vec{E}\perp c$ (dashed lines) at 300 K (blue lines, insulating M_1 phase) and 373 K (red lines, metallic R phase). The inset shows the temperature dependence of the $d_\|$ peak across the metal–insulator–transition at 340 K.
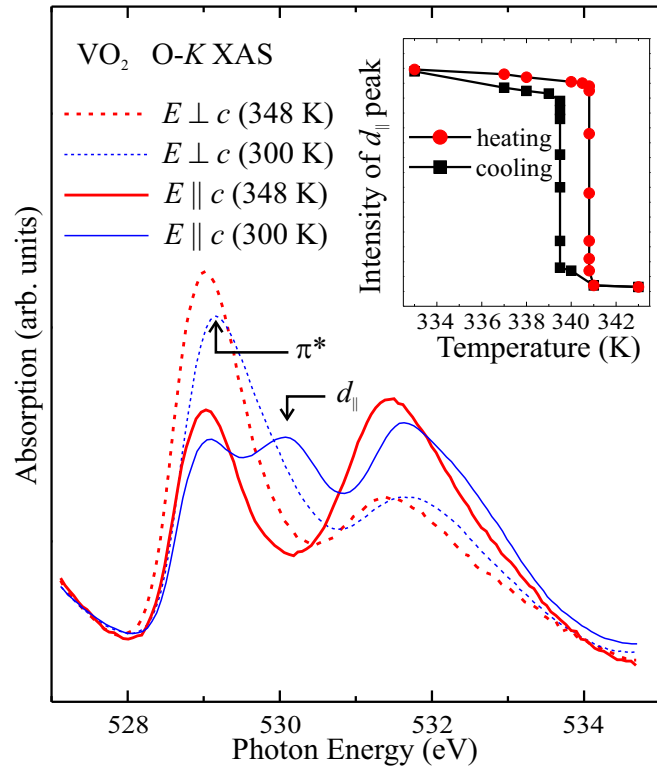
i.e. both below and above the MIT. The spectra show a very strong polarization dependence (solid vs. dashed lines), and for each polarization also a clear temperature dependence (blue vs. red lines). In going to the metallic phase, one observes in particular a shift of about 0.2 eV towards lower energies for the leading edge of the spectra. Together with the shift of roughly 0.4 eV in the opposite direction for the leading edge of the PES valence band spectra shown in figure 3.3, we thus find that the MIT involves the closing of a band gap of about 0.6 eV [101]. This is an anomalously large energy if one compares it to the energy scale of T_{MIT}, which is of order 30 meV. Such a discrepancy in energy scales has also been recognized for the V$_2$O$_3$ system [100], and this forms in fact yet another indication that the MIT cannot be described within the framework of the single–band Hubbard model.

To address specifically the possible role of the orbital degrees of freedom, we now focus on the polarization dependence of the O–K XAS spectra. For the $\vec{E}\|c$ spectra (solid lines), we observe that the peak labeled as $d_\|$ in figure 3.4 disappears in going from the insulating (blue line) to the metallic (red line) phase. The inset in figure 3.4 shows in detail the temperature dependence of the intensity of this peak. The sharp hysteresis across the MIT at 340 K confirms not only the high quality of the samples, but also that the occurrence of this peak is intimately linked to the MIT. The O–K structures are due to transitions from the O $1s$ to the O $2p$ orbitals that are mixed into the unoccupied V $3d$ t_{2g} and e_g states [102]. Following the proposal by Abbate *et al.* [103], the first peak at 529.1 eV can be assigned to the t_{2g}–π^* orbital and the second at 530.1 eV to the t_{2g}–$d_\|$. These assignments can now be confirmed by our polarization dependence data: the $d_\|$ peak can be seen with $\vec{E}\|c$ polarization only since mainly the O $2p$ orbitals with z symmetry (with z along c) have sufficient

hybridization with the $d_\parallel$ state which, as we will discuss below, is made up of the anti–bonding state of pairs of $d_\parallel$ orbitals [69].

The observation of the $d_\parallel$ peak as a main characteristic for the MIT strongly supports the conclusions of the recent orbital occupation study mentioned above [27]. There it was found that the orbital occupation is almost isotropic in the metallic phase, but that it becomes essentially pure $d_\parallel$ in the insulating phase. It is then quite natural to expect that this electronically 1–dimensional chain undergoes a Peierls transition and forms bonding/anti–bonding states of pairs of $d_\parallel$ orbitals. Important is the assertion that such a change in orbital occupation can only be made if the system is so strongly correlated that in fact it is already close to a Mott transition [27]. This can now be quantified from the spectra of figures 3.3 and 3.4. The energy separation between the bonding and anti–bonding $d_\parallel$ peaks can be estimated from the energy position of the insulator peak in the PES spectrum plus that of the $d_\parallel$ peak with respect to the onset of the XAS spectrum. This totals to roughly 2.5–2.8 eV. In a pure one–electron approximation, the energy separation equals $2t$, where t is the intra–dimer hopping integral. Using the LDA estimate of $t \approx 0.7$ eV [28], the separation would be 1.4 eV, a value which is clearly too small and which partially illustrates why LDA does not reproduce the insulating state of VO$_2$. Using instead the simple hydrogen–molecule model presented in chapter 4.4, to include explicitly correlation effects, the energy separation is given by $\sqrt{U^2 + 16t^2} - 2t$. Using $U \approx 4$ eV [28], we obtain a value of about 3.0 eV, which is satisfactorily close to the experiment.

The band gap itself of VO$_2$ is not determined by the $d_\parallel$ bonding/anti–bonding separation. While the first ionization state is given by the $d_\parallel$ bonding state, the first affinity state is in the simplest approximation mainly set by the π^* state, which lies about 1 eV lower in energy than the $d_\parallel$ anti–bonding state as can be seen from figure 3.4. This is also the general finding from the CDMFT study [28]: the π^* band dominates the lower part of the conduction band, while the $d_\parallel$ band centers at higher energies. Nevertheless, details in the band structure may lead to some fine tuning: the CDMFT predicts that there is some amount of $d_\parallel$ at the very onset of the conduction band. This is shown in figure 3.5, where we have replotted the CDMFT curves [28] after multiplication with the Fermi function for 300 K and convolution with the experimental resolution of 0.15 eV. To address this issue experimentally, we have also replotted in figure 3.5 the XAS spectra but now rescaled to the height of the first peak. In the metallic phase, the first peak for the $\vec{E}\|c$ spectrum (red solid line) falls on top of that of the $\vec{E}\perp c$ (red dashed), confirming that the orbitals have similar energies and are similarly occupied [27]. For the insulating phase on the other hand, we can clearly see that the top of the first peak of the $\vec{E}\|c$ spectrum (blue solid line) lies ≈ 0.1 eV lower than that of the $\vec{E}\perp c$ (blue dashed), indicating that the former is not of pure π^* character as the latter is. This in turn strongly suggests that there must be a state of different symmetry, i.e. $d_\parallel$, making up the low energy side of the peak, precisely as predicted by the CDMFT. It would be interesting to find out whether this sharp low lying state could represent a heavy quasi–particle if one dopes VO$_2$ in the M_1 phase with electrons.
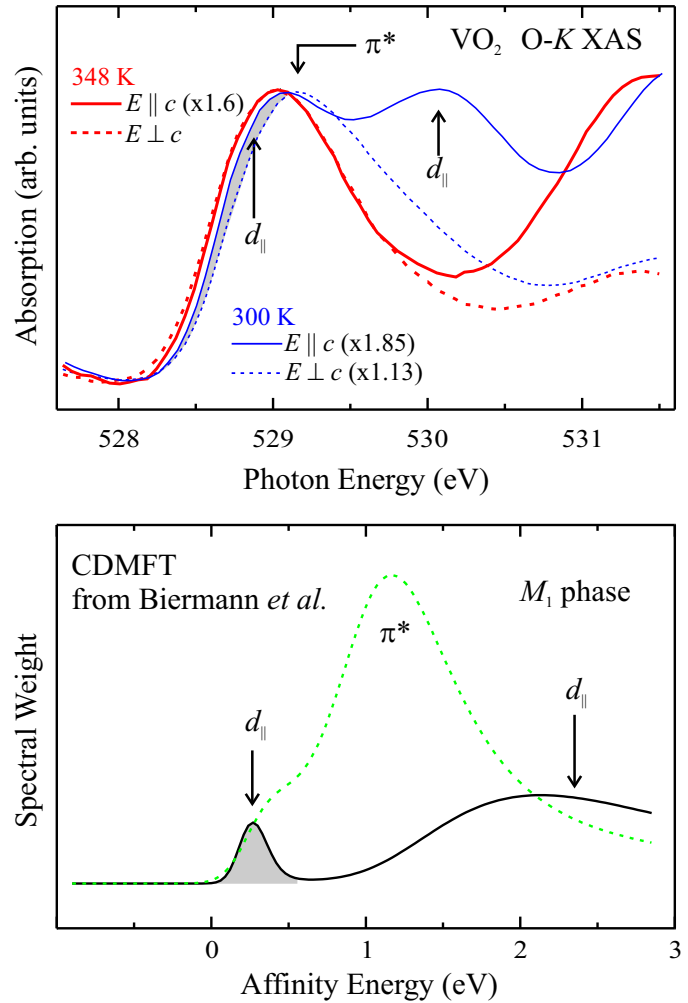
Figure 3.5: Top: O–K x–ray absorption spectra (XAS) of VO_2 from figure 2, rescaled to the maximum of the first peak. Bottom: CDMFT results for the V $3d(t_{2g})$ spectral weights as reproduced from Biermann *et al.* [28].

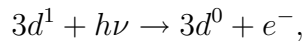## 3.5 Resonant Photoemission

In order to investigate the electronic structure of systems like transition metal oxides by means of photoelectron spectroscopy, one is usually most interested in the transition metal $3d$ contributions to the valence band spectra. These are unfortunately not always easily accessible, since their binding energies are close to, or even overlapping with low lying ligand states, in this case O $2p$. The latter tend to exhibit large photoemission intensities due to not only the relatively large number of electrons in the $2p$ band, but depending on the photon energy, also large photoionization cross sections. This means that the properties of the transition metal $3d$ electrons may be difficult to extract from the experimental spectra, and reliable statements can in some cases hardly be made [90].

With the choice of photon energy to coincide with core level absorption, however, cross sections can increase significantly, and since the absorption process is element specific, the spectroscopic sensitivity to the transition metal is enhanced. This can be easily understood by considering that besides the *direct* photoemission process, on resonance another *indirect* excitation channel involving core level absorption and subsequent Auger–decay contributes to the spectral weight [104–106]. For the example of the V–$2p$ resonance in VO_2, this means that in addition to direct
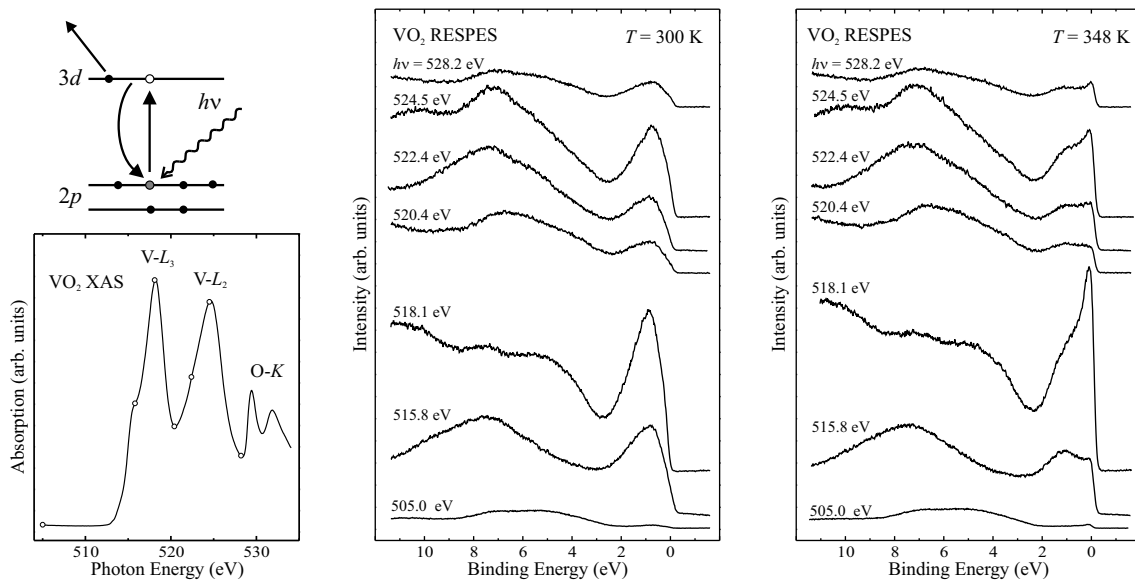
Figure 3.6: Left top: Schematic illustration of the indirect PES process at V–$2p$ resonance: electron occupation in the d^1 initial state is indicated by filled symbols, intermediate d^2 configuration due to resonance absorption of the grey–shaded electron is indicated by the open symbol. Left bottom: XAS spectrum of VO$_2$ at V–$L_{2,3}$ and O–K edges. Photon energies used for RESPES are indicted by open circles. Center, right: Valence band RESPES of VO$_2$ at V–$2p$ resonance in the insulating phase, $T = 300$ K, and in the metallic phase, $T = 348$ K, respectively.

photoemission,

$$3d^1 + h\nu \rightarrow 3d^0 + e^-,$$

the indirect process,

$$2p^6 3d^1 + h\nu \rightarrow 2p^5 3d^2 \rightarrow 2p^6 3d^0 + e^-$$
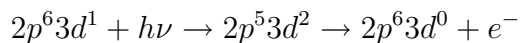
can take place, as illustrated in figure 3.6, left top. Since the two channels involve both the same initial and final states, they interfere coherently, possibly resulting in resonantly enhanced photoemission matrix elements [104, 107, 108]. Therefore, resonant photoemission (RESPES) has been used to increase photoemission intensities and gain sensitivity specifically for a certain element in the sample, e. g. in copper oxides [108–110], or even a particular spectral feature, e. g. the famous valence band satellite in nickel [111].

The resonance photon energies are chosen from the x–ray absorption spectrum. The spectrum of VO$_2$ shown in figure 3.6, left bottom, exhibits the V–L_3 and V–L_2 absorptions, consisting of two strong peaks at photon energies of 518.1 eV and 524.5 eV, respectively, and weak low energy shoulders at 515.8 eV and 522.4 eV, respectively. Structures at photon energies above 528.5 eV belong to O–K edge absorptions. We show the RESPES spectra of VO$_2$ in figure 3.6, for the insulating phase (center) and the metallic phase (right), taken at photon energies indicated by open circles in the XAS spectrum.

All spectra have been normalized to the integrated measuring time. We focus on the insulating phase first. Far away from resonance, at $h\nu = 505$ eV, the photo-emission intensity is very weak. At the shoulder in the V–L_3 peak, the intensity is strongly enhanced, with maxima at binding energies of around 0.9 eV and 7.5 eV. The latter lies within the broad feature observed in direct photoemission at $h\nu = 700$ eV shown in figure 3.3, which was attributed to mainly O–$2p$ character. We notice a significantly modified line shape of this feature in comparison with off–resonance spectra, suggesting that the resonating behaviour in this energy range is due to hybridization of V $3d$ with O $2p$. Furthermore, the ratio of the peak heights is considerably increased in favor of the low binding energy peak attributed to mainly V–$3d$ character, as compared to the off–resonance spectra. The increase of this structure is particularly large at photon energies corresponding to absorption maxima at $h\nu = 518.1$ eV and 524.5 eV, while it is relatively low in the absorption minima at $h\nu = 520.4$ eV and 528.2 eV. With varying photon energy, the line shape at binding energies above 3 eV changes noticeably and in a non systematic way, an explanation of which is still missing. On the other hand, the peak at 0.9 eV changes in height with photon energy, but not in shape.

As we turn to the metallic phase, we notice that the photon energy dependence of the line shape in the higher binding energy region is equal to the low temperature phase. This means that the electronic properties in this energy range are not affected by the MIT. In contrast, the V $3d$ peak shows a dramatic photon energy dependence not only in peak height, like in the insulating phase, but also and more striking, in line shape. In particular, the resonant enhancement of the incoherent satellite is exceptionally strong for photon energies of 515.8 eV and 522.4 eV corresponding to the low energy shoulders in the XAS spectrum. Although a detailed interpretation of the RESPES data is lacking, it is clear from the RESPES measurement that the low energy (< 3 eV) features in the valence band are related to the V $3d$ spectral weight. This is an important confirmation justifying that we can compare the low energy features of the direct photoemission ($h\nu = 700$ eV) with the V $3d$ spectral weights from the cluster–DMFT. It would be, however, extremely dangerous to use RESPES as a means just to obtain enhanced photoemission intensities with the hope to interpret these spectra as the direct representative for the V $3d$ spectral weight [98]. The photon energy dependence of the low energy features shown in figure 3.6 already demonstrates that this cannot be done.

Also the comparison between the RESPES spectra and the direct photoemission spectrum reveals important discrepancies. In figure 3.7, we show the direct photo-emission spectra taken at $h\nu = 700$ eV from figure 3.3 together with the RESPES (appropriately scaled to the direct PES) taken at the photon energy of the V–L_3 absorption peak *white line*, $h\nu = 518.1$ eV, for both the insulating and the metallic phase. The V $3d$ structure is much broader in the RESPES spectra (solid lines) than in the direct PES (dashed) for both phases, although the line width of the incoming light is even smaller for the lower photon energy. Furthermore, the line shape, especially in the metallic phase, is quite different in the RESPES. The inco-herent contribution appears as a broad shoulder on the wide high energy tail of the coherent peak. As a result, a quantitative analysis of the splitting and peak ratio, i.e. relative weights of the coherent and incoherent peaks, as one could do on the
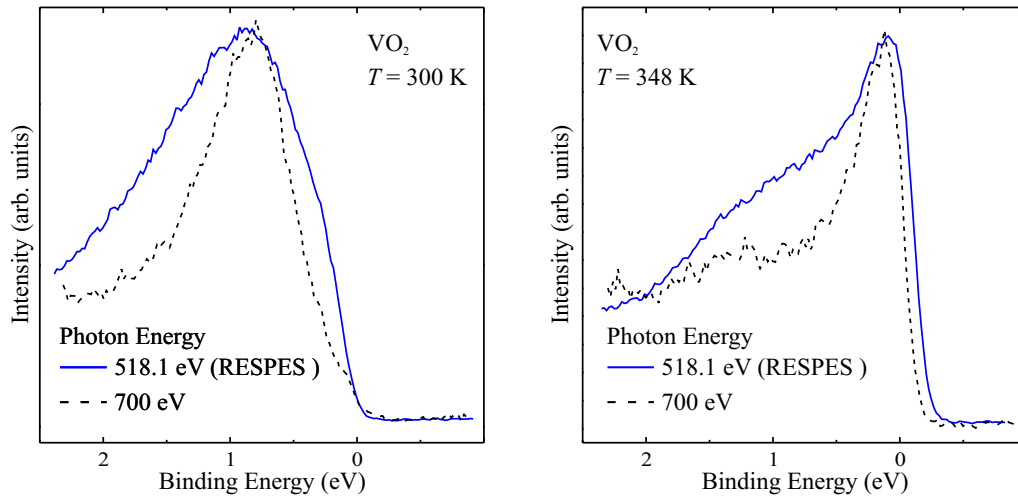
Figure 3.7: Valence band RESPES spectra of VO$_2$ ($h\nu$ = 518.1 eV, solid lines), in comparison with direct PES ($h\nu$ = 700 eV, dashed), for the insulating phase (left, T = 300 K), and the metallic phase (right, T = 348 K).

basis of the direct PES spectra, is not feasible from the RESPES.

This strong modification of the line shapes may be due to the dependence of the spectral weight on Auger transition matrix elements involved in the indirect process. Because of the localized nature of the core hole intermediate configuration appearing in the indirect process, the resonance effect is supposed to be stronger for excitations from more localized contributions to the ground state, while more delocalized contributions will not gain as much from the resonance. Moreover, also incoherent Auger emission might overlap with the RESPES signal [99]. Another aspect is the intrinsic line shape originating from the interference of the direct with the indirect process [107].

3.6   Valence band and core level XPS

In order to further check our photoemission results obtained at a photon energy of 700 eV, we repeated the measurements using monochromatized Al–K_α radiation with the energy of 1486.6 eV. The valence band spectra shown in figure 3.8 agree well with the results shown in figure 3.3, taking into account the lower resolution of this spectrometer, and a different cross section ratio between the V 3d and O 2p contributions. The weaker resolving power of this setup as compared to the measurements at ESRF hinders the observation of the incoherent peak in the metallic phase. Nevertheless, the line shapes of the V 3d weight including the very high intensity at the Fermi level for the metallic phase confirm the findings of the 700 eV experiments.

In line with our findings for LaCoO$_3$ in chapter 2, and in agreement with reports in the literature [85], we observe a noticeable deviation of the cross section ratio from the predictions of atomic calculations [66]. In particular, instead of an increased sensitivity to V 3d contributions, we observe a reduced relative V 3d intensity in the

Figure 3.8: Valence band spectra of VO$_2$ in the insulating ($T = 320$ K, open symbols) and metallic phase ($T = 350$ K, solid) measured with 1486.6 eV photon energy, together with the Ag Fermi level reference.
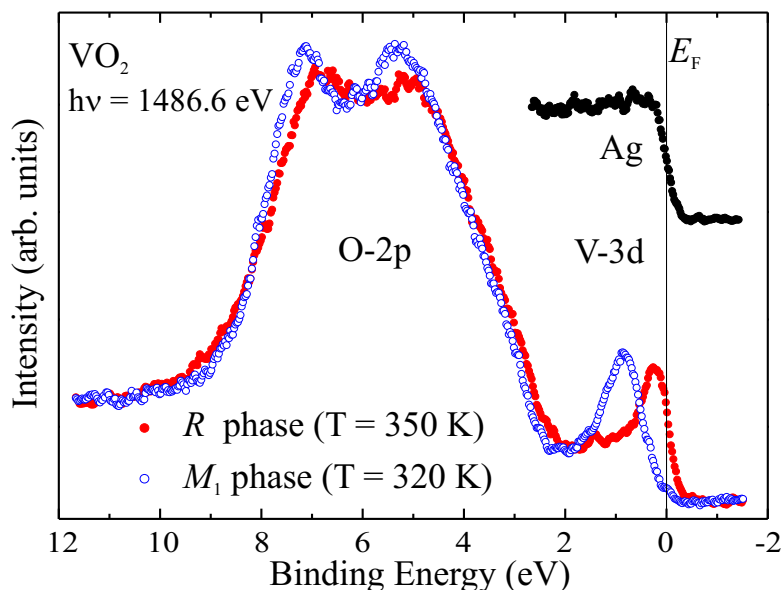
spectra taken with 1486.6 eV photons in comparison with the one taken at 700 eV.

In figure 3.9, the core level spectra of VO$_2$ are shown, taken with 1486.6 eV photon energy at 320 and 350 K, corresponding to the insulating and metallic phase, respectively. At first, we focus on the low temperature spectrum (dashed), which shows a strong peak at 529.7 eV attributed to O $1s$. Two smaller, and noticeably broader peaks at 515.8 and 523.4 eV represent the spin–orbit split V $2p$ excitations. We observe slightly asymmetric line shapes with a wider high energy side, especially for the V $2p_{3/2}$ peak, which are assumed to be due to multiplet structure. In contrast to the common feature of charge transfer satellites in the $2p$ core level spectra of transition metal oxides [112, 113], here such satellites cannot be identified clearly. This is however not an unusual observation for vanadium oxides [26, 114], which is related to the fact that the V $2p$ core levels are close in energy to the O $1s$. For instance, the positions of the charge transfer satellites in V$_2$O$_3$ determined by configuration–interaction cluster model calculations happen to lie on the tails of the V $2p_{1/2}$ and the O $1s$ peaks, respectively [114], and therefore can hardly be resolved in experiment [26]. Assuming a similar main–line to satellite separation as in V$_2$O$_3$ of ≈ 9.5 eV also in VO$_2$, we expect the satellite of the V $2p_{3/2}$ peak on the tail of the V $2p_{1/2}$ main line. This may be an explanation for the apparently more symmetric line shape of the latter as compared to V $2p_{3/2}$. The charge transfer satellite of the V $2p_{1/2}$ peak would in this case exactly coincide with the weak shoulder on the high energy side of the O $1s$ peak. In principle, the origin of this structure could be due to surface contamination with water. In such a case, the intensity of this peak usually increases noticeably with time, and should be very small in the beginning. However, we have not observed any significant time dependence of this shoulder, which strongly suggests to identify it with the charge transfer satellite of V $2p_{1/2}$.

Crossing the MIT, remarkable changes in the spectra take place. A considerable transfer of spectral weight to lower binding energies in the metallic phase (solid line) is observed for both the V $2p$ main lines as well as the O $1s$ peak. The asymmetric line shape of the O $1s$ peak in the metallic phase, with a steep low binding energy
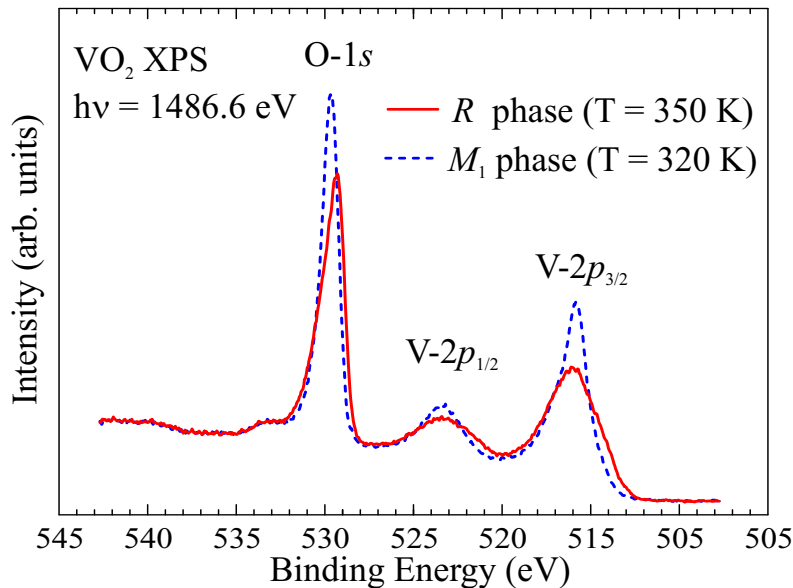
Figure 3.9: Core level spectrum of VO_2 in the insulating (T = 320 K, dashed) and metallic phase (T = 350 K, solid line) measured with 1486.6 eV photon energy.

side and a rather wide high binding energy tail, can be explained by the model of Doniach and Šunjić, which takes into account low energy electron–hole pair excitations in a metallic valence band during the photoemission process [115]. The transfer of spectral weight across the MIT is even larger at the V $2p$ main lines. The line shapes are not of Doniach–Šunjić–type, but rather seem to be due to additional contributions on the low binding energy sides of the peaks, resulting in weak shoulders. Again we can compare our findings with the results for V_2O_3, that show close similarities [26]. Park discussed the appearance of such low binding energy shoulders in the V $2p$ core level spectra of V_2O_3 on the basis of a two–impurity model, similar to the hydrogen molecule model presented in chapter 4.4. Within this approach, the presence of low binding energy satellites in the metallic phase is explained qualitatively by charge fluctuations in the valence band of the type $(d^2d^2) \rightarrow (d^3d^1)$ for V_2O_3 and $(d^1d^1) \rightarrow (d^2d^0)$ for VO_2, resulting in a well–screened contribution to the core–hole final state, which has only a small photoemission matrix element [26]. This means, we can directly observe the MIT and its influence on the electronic structure from the core level spectra. For a quantitative analysis of our results, however, detailed full–multiplet cluster calculations accounting for the many–body effects which shown up in the spectra, are indispensable.

3.7   Conclusions

Using bulk sensitive photoelectron spectroscopy, we observe a tremendous transfer of spectral weight in the valence band spectra of VO_2 across the MIT. From quantitative analysis as well as comparison to recent realistic many–body calculations, we find that a dimer approach represents a reasonable model to capture the essential electronic properties of VO_2. Together with the results of O–K x–ray absorption spectroscopy, which tells us that the orbital degrees of freedom play a decisive role in the MIT, we conclude that neither a simple Peierls transition nor a single–band Hubbard model can explain the MIT. Instead, a cooperative mechanism, making use of

both the lattice distortion and the orbital rearrangement due to strong correlations, drives the transition.

Chapter 4

Dimer formation in the low temperature phase of Ti$_2$O$_3$

4.1 Introduction

In order to motivate the interest in the issue of dimers in Ti$_2$O$_3$, we first turn our attention to the related system V$_2$O$_3$. This system has attracted a lot of interest in the last sixty years, as documented by more than 500 publications. V$_2$O$_3$ is one of the most important model systems in solid state physics and a benchmark problem in the study of many-body effects. It takes this excellent position due to its interesting physical properties and the very rich phase diagram. Pure V$_2$O$_3$ shows a dramatic drop of the resistivity by 7 orders of magnitude at $T_{\mathrm{MIT}} = 150$ K with long–range antiferromagnetic order in the low temperature insulating phase [116–118]. At the same time, the crystal lattice distorts from the high temperature corundum (α– Al$_2$O$_3$) structure to a monoclinic phase with a reduced c/a ratio. Most remarkable was the discovery of a paramagnetic insulating phase at higher temperatures which occurs in lightly chromium doped V$_2$O$_3$. Since this MIT does not go together with a change in the lattice symmetry, it was claimed to be one of the first experimental discoveries of the correlation driven Mott transition [119]. As a result, the metallic state has to be considered highly correlated as well, even in the undoped system. Moreover, also the antiferromagnetic insulating phase displays unexpected properties with an unusually large magnetic moment of 1.2 μ_{B} per V site [120].

Very early considerations of Goodenough concerning direct cation–cation inter-action (as opposed to interactions mediated by ligand ions) suggest the pairing of transition metal ions to play an important role especially for the low temperature properties. As is shown in figure 4.1, the metal ions are arranged in hexagonal planes perpendicular to the crystallographic c axis, alternating with hexagonal planes of oxygen. The stacking order of the metal planes results in pairs of metal ions along the c axis which promoted the assumption of dimerization as an explanation for the MIT. The standard model proposed for V$_2$O$_3$ is based on the formation of a molecular orbital singlet on the c axis pair [121]. The configuration of the V^{3+} ions is $3d^2$. A trigonal distortion splits the t_{2g} orbitals in a doubly degenerate e_g^π orbital and a non–degenerate a_{1g} orbital, as illustrated with the energy level diagram in figure 4.1. The a_{1g} orbital is extended along c direction. Therefore, assuming a
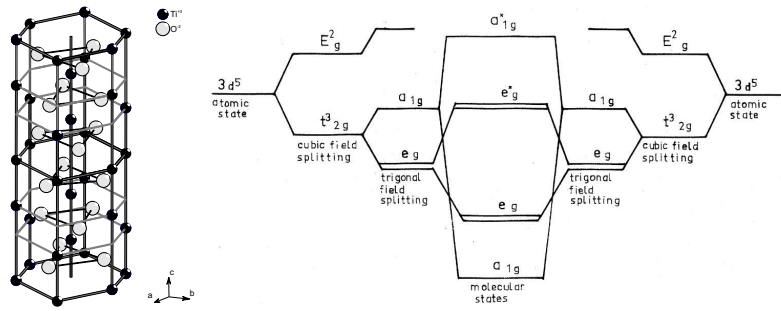
Figure 4.1: (Left) Corundum structure of Ti_2O_3 at $T = 300$ K in the insulating phase. Titanium (oxygen) sites are indicated by black (white) spheres. To show hexagonal planes, bonds to non–existing sites have been added. (Right) Energy level diagram of V_2O_3 proposed by Castellani *et al.* [121] for a c axis pair of vanadium sites. One–electron orbitals of each site are shown on the left and right sides, and the two–site molecular orbitals in the center.

strong hybridization between the a_{1g} electrons of the c axis pair vanadium ions, a lower lying local molecular orbital singlet can be formed, which does not contribute to the long–range ordered magnetic moment. Thus the experimental value can be interpreted as the covalency enhanced magnetic moment of a single e_g^π electron per site, and the physics of the system can be described in a one-band Hubbard model.

This elegant approach, however, could not be verified experimentally. Instead, a local spin $S = 1$ and considerable changes of the orbital occupation across the MIT were observed in polarization dependent XAS investigations [100]. In particular, the occupation of the a_{1g} orbital was found to be not more than $1/2$ per site for all temperatures. As a consequence, the existence of a molecular orbital singlet state and the proposed single-band Hubbard model description of V_2O_3 with the a_{1g} orbitals considered as inactive, can be ruled out. Moreover, band–structure calculations have shown that the hybridization to nearest neighbours in the ab plane is equally strong as the c axis hybridization, clearly disproving the existence of an electronic dimer [122]. If the hybridization were of importance for the MIT, one expects a shorter atomic distance of the c axis pair below the transition. For V_2O_3, however, the bond length decreases with rising temperature [117]. On the other hand, not only the opposite behaviour is observed for Ti_2O_3, but also the absolute value of the distance between the ions along the c axis is shorter than in V_2O_3 by about 5% at room temperature (which is low for Ti_2O_3 but high for V_2O_3) [123, 124]. Thus, it seems plausible to look for the presence of dimers in Ti_2O_3.

Also Ti_2O_3 shows a change in conductivity with temperature from insulating to metallic [71]. But instead of a sharp drop at the transition temperature, a gradual change is observed in the interval from $300 - 500$ K. Along with the transition, the crystal lattice only changes moderately. In particular, a change in symmetry is not observed [124]. The earliest models proposed to explain the low temperature insulating phase of Ti_2O_3 assumed a band splitting due to antiferromagnetic long–range order at low temperature [71]. However, no experimental evidence for a magnetic ordering was found [125, 126]. Instead, the increase of the trigonal splitting as a result of the shortening bond length of the c axis pair at lower temperature was

proposed to open the gap [77, 127]. This model is again contradicted by LDA band structure calculations showing that the overlap of the a_{1g} and e_g^π orbitals can only be suppressed for an unrealistically short bond length [128]. However, it is not unusual for transition metal oxides that normal LDA is not able to reproduce the electronic properties especially of insulating phases correctly because of the breakdown of the one–electron approximation for correlated systems. In turn, we can conclude that electronic interactions play a decisive role in establishing the insulating phase of Ti_2O_3.

Several groups have investigated the electronic structure of Ti_2O_3 experimentally using photoelectron spectroscopy [129–133]. Previously published results using either UV–light or soft x–rays, as well as resonant PES, show quite convincing agreement in the valence band spectra , while the Ti $2p$ core level spectra in the literature display noticeable differences [132]. The reliability of the spectra appears to be questionable, in the case of the low photon energy experiments due to the enhanced surface sensitivity, and because of uncontrolled line shape effects at resonant photoemission [99, 131]. Consequently, different conclusions have been drawn by the various authors. In order to obtain reliable information on the electronic structure and the possible existence of dimers in the insulating phase, we have studied the valence band and core level spectra using bulk sensitive photoelectron spectroscopy of high quality Ti_2O_3 crystals at room temperature with photon energies of both 1.5 and 6 keV.

4.2 Experimental

Single crystals of Ti_2O_3 were grown by H. Roth using a floating–zone mirror furnace, and subsequently characterized by x–ray diffraction and thermogravimetric analysis. No impurities or foreign phases in the samples were detected, which was also confirmed by wide range photoemission. All measurements were taken at room temperature on *in–situ* cleaved samples. The 1.5 keV photoemission spectra (in the following referred to as XPS) were collected using a VG twin–crystal monochromatized Al K_α x–ray source (hν = 1486.6 eV) and a Scienta SES 100 hemispherical electron energy analyzer. The overall experimental energy resolution was set to 350 meV. The pressure in the spectrometer chamber was below 2×10^{-10} mbar during the measurement. The 6 keV photoemission spectra (in the following referred to as VOLPE) were taken at the ID16 beam line of the ESRF, Grenoble, using the VOLPE spectrometer [63]. At a photon energy of 5931 eV, the overall experimental resolution was set to 365 meV. The pressure was kept below 5×10^{-9} mbar throughout the experiment. The process of aging of the sample was monitored by repeated O1s spectra alternating with the measurement of the valence band region. No significant changes during the entire experiment (48 hrs. in case of XPS and 12 hrs. for VOLPE) were observed.
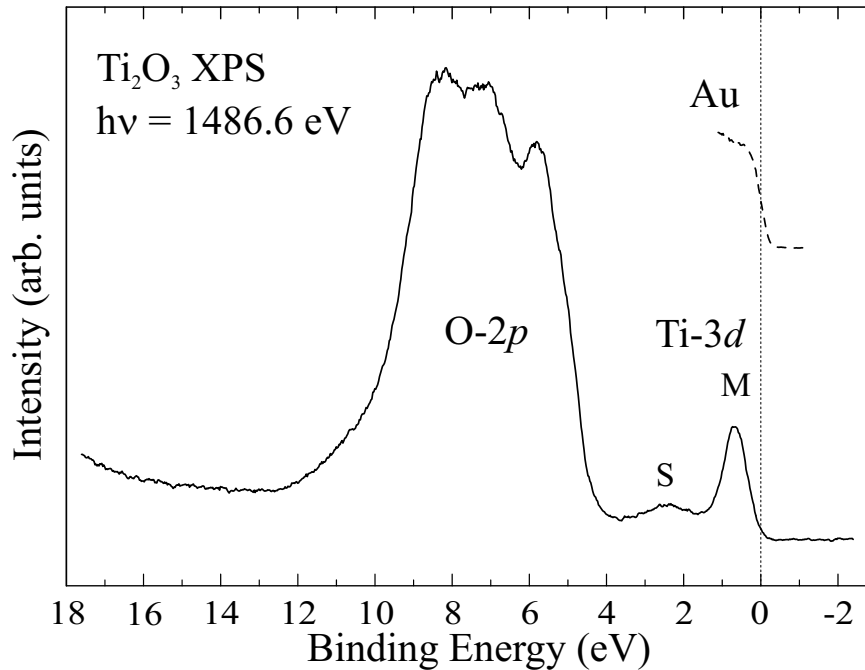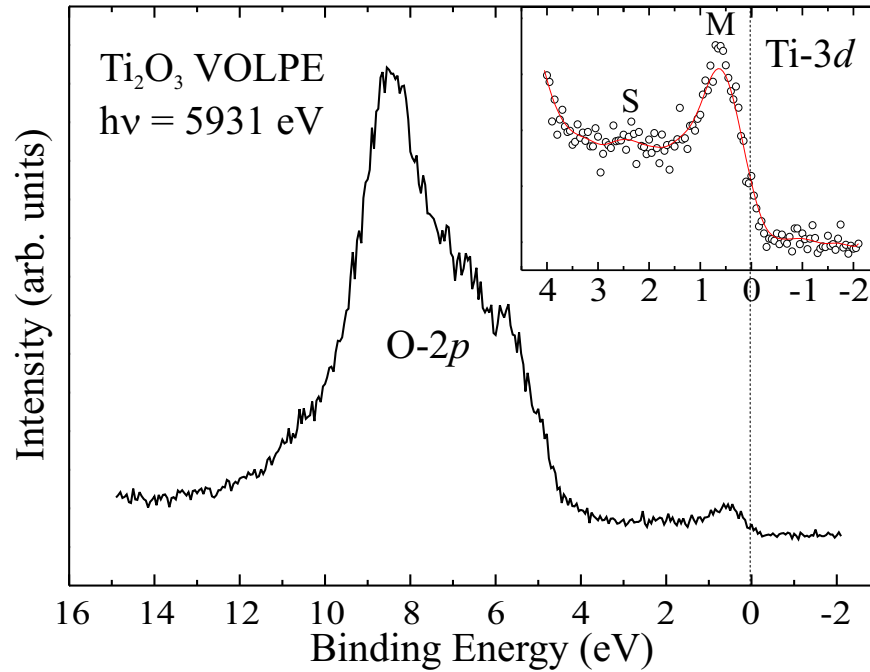
Figure 4.2: Room temperature valence band photoemission spectrum of Ti_2O_3 taken at 1486.6 eV photons. The Ti $3d$ contribution at binding energies up to 4 eV shows two discrete features. The large contribution at higher binding energies is attributed to O $2p$ excitations. The Fermi level was determined on a polycrystalline gold sample shown by the dashed line.

4.3   Results and Discussion

The room temperature XPS valence band spectrum is shown in figure 4.2. The large spectral weight at 4 - 10 eV binding energies is supposed to be mainly of O $2p$ character and will not be considered for the moment. Instead, we focus on the lower energy region from the Fermi level up to 4 eV, which consists of Ti $3d$ contributions. This part of the spectrum is characterized by two distinct structures. The main line (M) is a quite symmetric peak with a width of $\approx$ 0.8 eV FWHM centered at about 0.7 eV. The semiconducting or insulating nature of the system at room temperature [134] is reflected by the fact that the spectral weight vanishes close to the Fermi level. The second feature is a weak but clearly noticeable satellite (S) at around 2.4 eV binding energy. The existence of this satellite has not been reported in the literature before, and it bears strong implications on theoretical predictions. A detailed discussion hereof follows in the next section.

One of the concerns with respect to the results reported in the literature is related to the surface sensitivity of PES for low photon energies. One can estimate that the probing depth is no more than 7 – 10 Å for ultra violet photons. At 1.5 keV photons, the probing depth is estimated to be around 20 Å. For a more bulk sensitive measurement, we have repeated the experiment with x–rays of 5931 eV photon energy. In this case, the escape depth is considerably increased to at least 50 Å [63]. Figure 4.3 shows the valence band spectrum of Ti_2O_3 taken with the

**Figure 4.3:** VOLPE spectrum of Ti_2O_3 valence band taken at room temperature using 5931 eV photons. The weak Ti $3d$ signal shown as a blow up in the inset has been measured five times longer. As a guide to the eye, the solid line shows the data after convolution with a Gaussian of $\sigma = 180$ meV.

VOLPE spectrometer at room temperature. The spectrum is dominated by the O $2p$ band (4 – 10 eV binding energy) while the Ti $3d$ contribution (0 – 3 eV binding energy) is quite weak. Since photoionization cross sections decrease strongly with photon energy, photoemission at 6 keV is an extremely low count rate experiment. Therefore, the Ti $3d$ contribution was measured again, but now five times longer in order to get a reasonable signal–to–noise ratio, and the result is shown in the inset of figure 4.3. We now can see the main peak (M) and, be it faintly, the satellite (S), supporting the XPS findings.

An intriguing aspect of the VOLPE spectra, is the small Ti $3d$ photoionization cross section relative to that of O $2p$. This is in strong contrast to the calculations by Yeh and Lindau [66], and Scofield [67], both predicting that the cross section for O $2p$ decreases faster with photon energy than for Ti $3d$. This discrepancy is a common observation in hard x–ray photoemission [135, 136] and has been reported already for 1.5 keV photons by Sawatzky and Post long ago [85]. It agrees qualitatively with our observation of the photon energy dependence in the spectra of $LaCoO_3$, presented in chapter 2, as well as VO_2 in chapter 3. The clear differences between VOLPE and XPS in the region of 4 – 8 eV binding energy may be explained by cross section effects as well. This region is attributed to mostly O $2p$ character. But hybridization mixes in some Ti contributions, which in the VOLPE spectrum are suppressed for $3d$, but may be strongly enhanced in case of $4s$.

In figure 4.4, the Ti $2p$ core level spectra are presented. The VOLPE spectrum, displayed by open circles, agrees well with the XPS result within noise. Besides
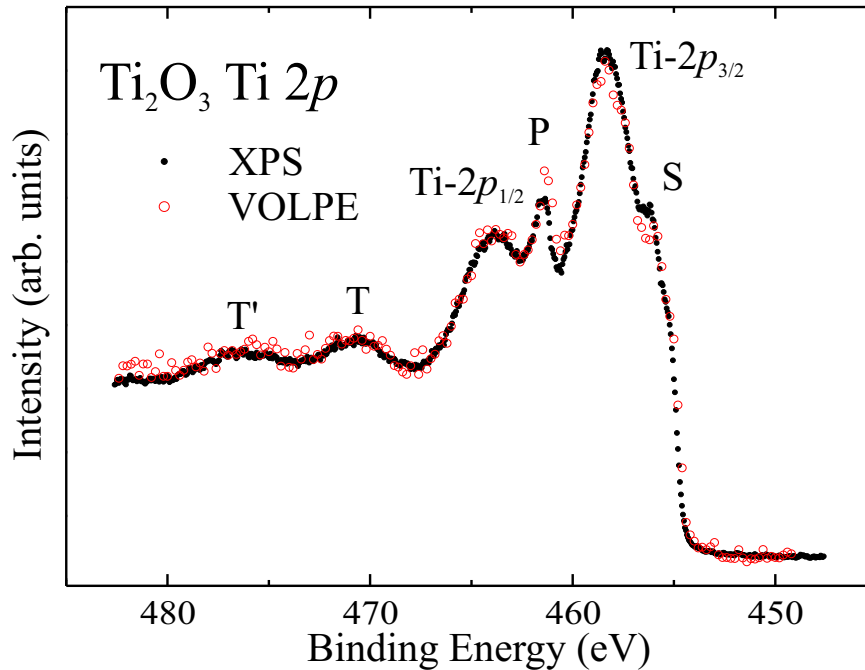
Figure 4.4: The XPS (solid) and VOLPE (open) Ti $2p$ core level spectrum of Ti_2O_3 at room temperature shows the spin orbit split Ti $2p_{3/2}$ and $2p_{1/2}$ peaks and two high energy satellites (T, T'). Additionally, we observe a shoulder (S) and a sharp peak (P).

the spin–orbit split two–peak structure at 458.3 eV and 463.8 eV binding energy, the spectrum shows a low–energy shoulder S at 456.2 eV and a pronounced and sharp additional peak P at 461.5 eV. These features have not been reported in the literature so far. In order to check whether the origin of these structures could be due to non–stoichiometry, we have partially oxidized the sample using an oxygen radical source. However, both features survive unaffected while the main peaks change strongly in shape and position. We therefore conclude that the observed spectra cannot be due to Ti^{4+} impurities, the most likely contamination to occur for Ti $3d^1$ oxides. The agreement between XPS and VOLPE furthermore rules out any explanation in terms of surface effects. So the additional features must be part of the bulk Ti_2O_3 spectrum.

We can simulate low binding energy satellites within the hydrogen molecule model calculation presented in the next paragraph. The origin of these satellites can be explained by non local screening involving the neighbouring titanium ion, as proposed by Veenendaal and Sawatzky for NiO and CuO [137]. Two more high energy satellites T at 470.5 eV and T' at 476.5 eV binding energy have been interpreted as charge–transfer satellites in a previous work [132]. This interpretation however requires an unusually high value of the charge transfer energy Δ of 6.5 eV. A quantitative analysis of our data by means of configuration interaction cluster model calculations on the basis of a Ti–Ti dimer is in progress.

4.4 The Hydrogen Molecule Model

As pointed out above, the presence of correlation effects is expected to be directly observable in PES. Previous photoemission studies of Ti_2O_3 did not observe the Ti $3d$ satellite at 2.4 eV binding energy. From a one–electron point of view, a single peak in the photoemission spectrum is expected for a $3d^1$ system. This expectation is met by the predictions of LDA band theory [128]. Taking into account correlation effects, a TiO_6 cluster also does not produce a two–peak structure separated from the ligand hole final states [138]. We therefore have to consider the formation of a molecular orbital on c axis titanium pairs to capture the essentials of the electronic structure. To do so, we will use a very simple model system, namely an isolated dimer equivalent to a hydrogen molecule.

This model consists of two electrons that can be distributed over two sites denoted by $i = 1, 2$. The ground state $|GS\rangle$ of the system can be described as a linear combination of a state $|\varphi_0\rangle$ in which the two electrons are on different sites coupled to a singlet, and another state $|\varphi_1\rangle$ in which both electrons are on the same site,

$$
\begin{aligned}
|GS\rangle &= \alpha|\varphi_0\rangle + \beta|\varphi_1\rangle \\
|\varphi_0\rangle &= \frac{1}{\sqrt{2}} \left(c_{1\uparrow}^\dagger c_{2\downarrow}^\dagger + c_{2\uparrow}^\dagger c_{1\downarrow}^\dagger \right) |0\rangle \\
|\varphi_1\rangle &= \frac{1}{\sqrt{2}} \left(c_{1\uparrow}^\dagger c_{1\downarrow}^\dagger + c_{2\uparrow}^\dagger c_{2\downarrow}^\dagger \right) |0\rangle.
\end{aligned}
$$

Here, $|0\rangle$ denotes the vacuum of the system out of which the operators $c_{i\sigma}^\dagger$ create an electron at site i with spin $\sigma =\uparrow, \downarrow$. The triplet states are not considered since they are higher in energy. The coefficients α and β are determined by diagonalizing the ground state Hamiltonian,

$$
\mathcal{H}_{GS} = \left(\begin{array}{cc} 0 & 2t \\ 2t & U \end{array} \right),
$$

in which U denotes the on–site Coulomb repulsion between two electrons at the same site, and t the hybridization energy. The energy of the ground state is

$$
E_0 = \frac{U}{2} \left(1 - \sqrt{1 + \left(\frac{4t}{U} \right)^2} \right).
$$

The photoemission process, in which an electron is removed, is represented by the annihilation operators $c_{i\sigma}$. In a basis of states with the remaining electron localized at one of the two sites, $c_{i\sigma}^\dagger|0\rangle$, $i = 1, 2$, the final state Hamiltonian and the corresponding eigenstates are given by

$$
\mathcal{H}_{FS} = \left(\begin{array}{cc} 0 & t \\ t & 0 \end{array} \right),
$$

$$
|FS^\pm\rangle = \frac{1}{\sqrt{2}} \left(c_{1\sigma}^\dagger \pm c_{2\sigma}^\dagger \right) |0\rangle.
$$

These final states are the well known bonding and antibonding states of the H$_2^+$ ion which are separated in energy by $2t$. Depending on the spin of the removed photoelectron, the final states can take two spin orientations σ of equal energy. One can see immediately that the photoemission spectrum of this system consists of two lines associated with the two final states, as is illustrated in figure 4.5. The separation
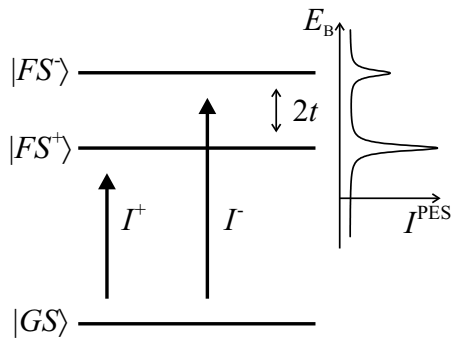
Figure 4.5: Total energy level diagram for the photoemission process in a hydrogen molecule model. The two accessible final states $|FS^+\rangle$ and $|FS^-\rangle$ yield two lines in the spectrum of intensities I^+ and I^-, respectively, according to the initial state coefficients α and β. The corresponding spectrum is indicated on the right.

of the peaks in the spectrum is given by the final state splitting $2t$. Their intensities depend only on the initial state coefficients α and β. A qualitative spectrum is sketched in figure 4.5 on the right with a lifetime broadening of the photoemission lines taken into account.

We calculate the spectrum as the intensity proportional to the square of the transition matrix elements for the photoemission process,[1]

$$
\begin{aligned}
I^\pm \;\; &\propto \;\; \|\langle FS^\pm|c_{i\sigma}|GS\rangle\|^2 \\
&= \;\; \left(\frac{\alpha}{2} \pm \frac{\beta}{2}\right)^2 \\
&= \;\; \frac{1}{4}\left(1 \pm \sqrt{1 - \frac{1}{1 + \left(\frac{4t}{U}\right)^2}}\right).
\end{aligned}
$$

It turns out that the intensities only depend on $(t/U)^2$, and we can immediately evaluate the relative intensities for two limiting cases. Firstly, for $t = 0$, both intensities become equal and the spectrum will consist of two equally high lines. In this case, however, the splitting vanishes and the two lines coincide. On the other side, for $U = 0$, I^- vanishes, and the spectrum will be given by a single line only.

Figure 4.6 shows the calculated photoemission spectra of the simple hydrogen molecule model in energy units of U with a lifetime broadening of $0.04U$ FWHM for t/U in the range from 0 to 0.3 from the bottom up. In the foreground, the case of $t/U = 0$ is shown. It seems to consist of a single line only. For finite values $t/U \ll 1$, two lines of nearly equal height and a very small splitting evolve. While the low binding energy peak increases with t/U, the high binding energy peak is fading away. As is shown in the left inset of figure 4.6, the intensity I^+ approaches

---

[1]Note that the sum of I^+ and I^- equals 1/4 instead of 1. Since there are four photoemission operators $c_{i\sigma}$ for $i = 1,2$ and $\sigma = \uparrow,\downarrow$, which naturally all yield the same intensities, the total intensity equals 1.
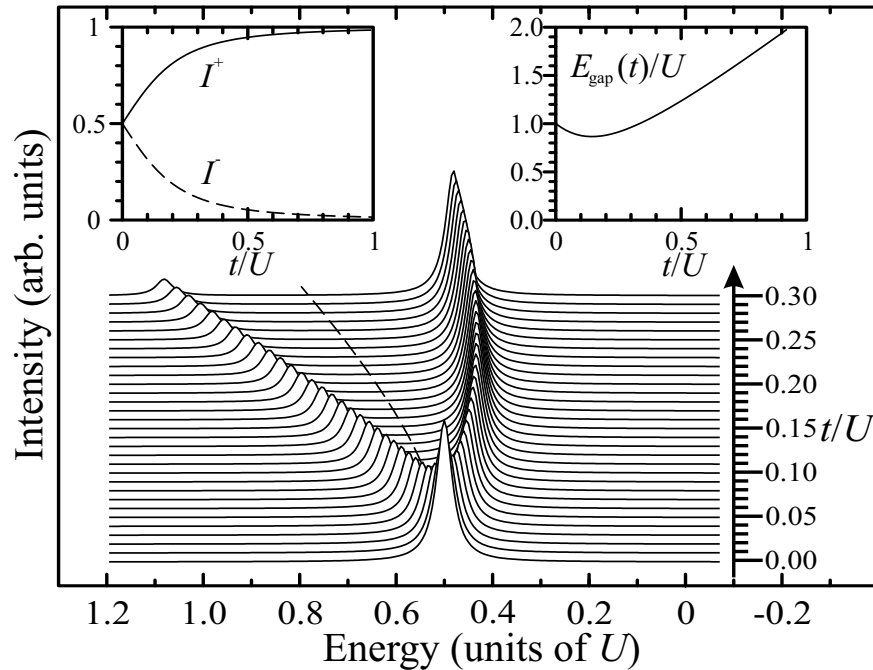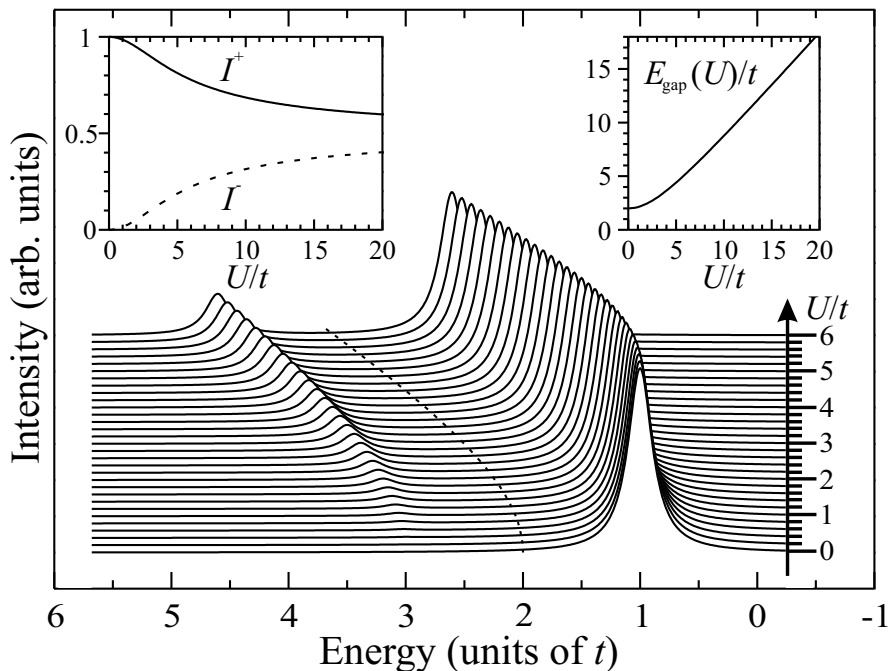
Figure 4.6: The calculated photoemission spectra of the hydrogen molecule model in energy units of U for $0 \leq t/U \leq 0.3$ with a lifetime broadening of $0.04U$. The dashed line indicates the center of the two peaks. Left inset: the variation of I^+ (solid line) and I^-(dashed) with t/U. Right inset: the energy gap in units of U as function of t/U.

one, and I^- is almost negligible already for $t/U \approx 1$. The reason for this suppression of the second peak is the quantum mechanical interference effect. Still, the system can take both the bonding and the antibonding final states. However, for $U = 0$ the photoemission intensity for the antibonding final state vanishes, because the ground state is given by $\alpha = \beta = \frac{1}{\sqrt{2}}$. This is equal to the doubly occupied bonding final state which has no overlap with the antibonding final state. In figure 4.7 we show the same calculations in energy units of t, i.e., coming from the opposite limit. In this representation, the splitting of the two lines in the spectrum is fixed at 2.

Note the peculiar similarity for the limiting cases, both represented by a single line with the same weight. The difference is that for $t = 0$, it actually consists of two lines at the same position with half the weight each, while for $U = 0$ the second line vanishes due to interference and all the weight goes to the other one. For all intermediate cases, the spectrum consists of two peaks of different intensity and an energy separation $2t$. The center of the peaks is indicated by a dashed line in figures 4.6 and 4.7. The energy scale is chosen such that the zero, given by the chemical potential μ, lies in the center of the energy gap shown in the right inset.

In order to determine the energy gap, excitations of negative binding energy have to be considered. The so–called *inverse* PES or IPS experiment yields the corresponding 3 particle excitation spectrum of the H_2 molecule which is symmetric to the PES, as illustrated in figure 4.8. The *total* energies of the final states depend in both cases on the on–site energy ε of the electrons. The gap is however independent of this on–site energy, as can be seen from PES and IPS displayed back to back

Figure 4.7: The calculated photoemission spectra of the hydrogen molecule model in energy units of t for $0 \leq U/t \leq 6$ with a lifetime broadening of $0.25t$. Otherwise, the representation is the same as is figure 4.6.

in figure 4.8(c). Since the combination of a PES and IPS process is equivalent to an electronic transport excitation, the energy difference of the lowest PES and IPS peaks is equal to the conductivity gap E_{gap},

$$E_{gap} = -2t + U\sqrt{1 + \left(\frac{4t}{U}\right)^2}.$$

Comparing this H_2 model calculation with the experimental results for Ti_2O_3, we can make the following statements. First of all, the hydrogen model seems to be appropriate for Ti_2O_3 because the qualitative feature of a two–peak structure is reproduced. Both systems have a formal occupation of one electron per site. The relevant unit of the model is a two–site cluster, or *dimer*. Consequently, such dimers seem to dominate the electronic properties of Ti_2O_3 at least in the low temperature insulating phase. If we take a closer look at the experimental spectra shown in figure 4.2 and the calculations in figures 4.6 and 4.7, we can deduce from the intensity ratio S:M a value of $t/U \approx 0.25$. Typical values of U for the early transition metal oxides range around $3 - 5$ eV. From the experimental splitting we deduce a value of $t = 0.85$ eV which reasonably agrees with the Harrison value of the σ hopping $V_{dd\sigma}$ for Ti^{3+} [139]. So we find indeed a ratio $t/U \approx 0.25$. Considering the simplicity of our model, this is a remarkable agreement.

We can go even further and try to reproduce the low binding energy satellites in the Ti $2p$ core level spectra, S and P. For this purpose we simulate the core hole by an energy reduction Q on the site carrying the photohole. Since the symmetry
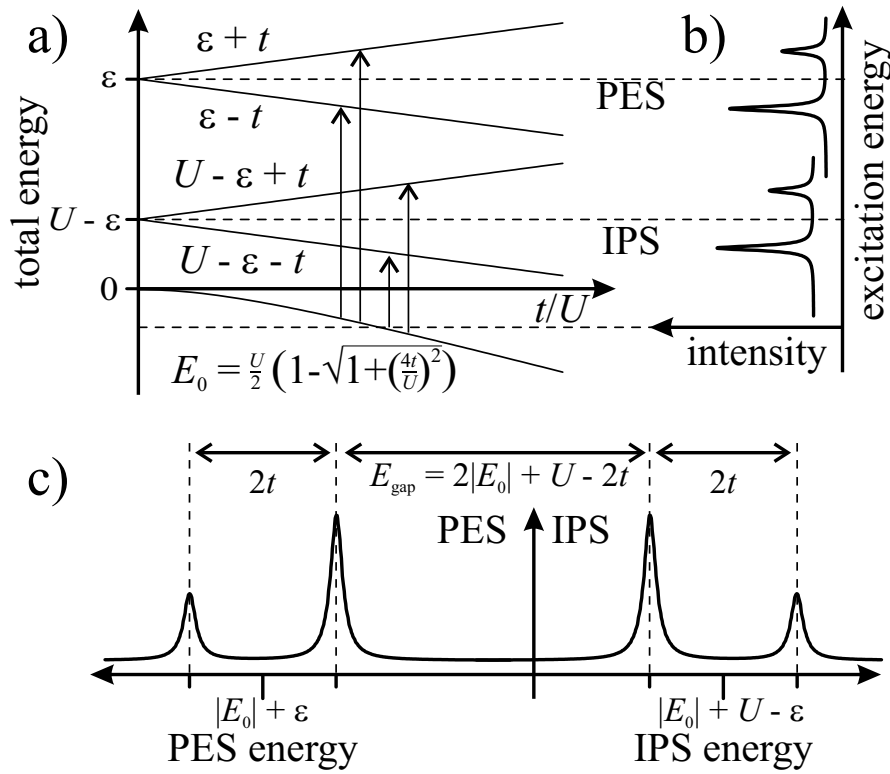
Figure 4.8: The PES and IPS energy level diagram for the H_2 molecule. Top left (a): total energies of ground state as well as PES and IPS final states. Right (b): respective spectral intensities as function of excitation energy. Bottom (c): IPS excitations in energy displayed to the right, PES to the left, with both zeros coinciding. The gap is the difference between the lower peaks of PES and IPS.

between the two sites is broken in this process, the compact 2×2 representation used above is not appropriate in this case. Instead, we represent the initial states in the following basis,

$$
\begin{aligned}
|\varphi_1\rangle &= c_{1\uparrow}^\dagger c_{1\downarrow}^\dagger |0\rangle \\
|\varphi_2\rangle &= c_{2\uparrow}^\dagger c_{2\downarrow}^\dagger |0\rangle \\
|\varphi_3\rangle &= \frac{1}{\sqrt{2}} \left(c_{1\uparrow}^\dagger c_{2\downarrow}^\dagger + c_{2\uparrow}^\dagger c_{1\downarrow}^\dagger \right) |0\rangle.
\end{aligned}
$$

We use the notation $q_{1\uparrow}$ as the annihilation operator of a core electron with spin up at site 1, and use as a basis for the final states $|\varphi_i'\rangle = q_{1\uparrow}|\varphi_i\rangle$, $i = 1, 2, 3$. The photoemission intensities are given by the transition matrix elements of the initial state with the three resulting final states,

$$
\begin{aligned}
|GS\rangle &= \alpha_0|\varphi_1\rangle + \beta_0|\varphi_2\rangle + \gamma_0|\varphi_3\rangle \\
|FS_j\rangle &= \alpha_j|\varphi_1'\rangle + \beta_j|\varphi_2'\rangle + \gamma_j|\varphi_3'\rangle, \quad j = 1, 2, 3 \\
I_j &= \left(\alpha_0\alpha_j + \beta_0\beta_j + \gamma_0\gamma_j \right)^2.
\end{aligned}
$$

The coefficients are determined by diagonalization of the respective Hamiltonian,

$$
\mathcal{H}_{GS} = \begin{pmatrix} U & 0 & \sqrt{2}t \\ 0 & U & \sqrt{2}t \\ \sqrt{2}t & \sqrt{2}t & 0 \end{pmatrix}, \quad \mathcal{H}_{FS} = \begin{pmatrix} U-2Q & 0 & \sqrt{2}t \\ 0 & U & \sqrt{2}t \\ \sqrt{2}t & \sqrt{2}t & -Q \end{pmatrix}.
$$

As a result, we find three photoemission lines for core level spectroscopy. For $Q = 0$, two of them have no intensity, because initial and final states are identical, and all intensity goes to the line with the lowest binding energy. We find however, that with increasing Q, the intensity of the lowest line is going down, and for $Q \geq U + 2t$ becomes less than the intensity of the higher lying one. This means, the roles of main line and satellite are exchanged, and the spectrum will show a low binding energy satellite.[2] The nature of this satellite is dominated by the configuration with both electrons on the site with the core hole. Its origin is the screening of the core hole due to transfer of charge from the neighbouring site. This process is similar to the well known charge transfer satellites in transition metal compounds involving the hybridization with ligand ions [112, 113], and the hybridization with neighbouring clusters [137], also called non-local screening effects.

4.5 Conclusions

We have investigated the low temperature phase of Ti_2O_3 with bulk sensitive photo-electron spectroscopy. We find a distinct two–peak structure in the Ti $3d$ contribution to the spectrum. In comparison of the valence–band spectra taken at different photon energies, we observe surprising cross section effects. Opposite to expectations from the widely accepted *atomic* calculations, the weight in the O $2p$ band region dominates over Ti $3d$ at high photon energies.

On the basis of a hydrogen model calculation, we can identify the satellite with the antibonding final state. Therefore we conclude, that the dimerization is strong at least in the insulating phase. Despite the simplicity of the model, a realistic value for $t/U \approx 0.25$ is found from comparison between experiment and calculation.

In the Ti $2p$ core level spectra we observe additional features that have not yet been reported in the literature. Any impurity explanation for the origin of these structures could be ruled out. We can find qualitative understanding of the low binding energy satellites in terms of non local screening effects from the H_2 model. A quantitative analysis on the basis of cluster calculations taking two titanium sites into account is pending.

---

[2] A third photoemission line corresponding to the highest final state has a much smaller intensity within the H_2 model and will give only a weak contribution on the high binding energy side.

Chapter 5

On the Metal–Insulator Transition in GdBaCo$_2$O$_{5.5}$

5.1 Introduction

The oxygen–deficient perovskite systems RBaCo$_2$O$_{5+\delta}$, R = rare earth, have attracted a lot of interest ever since the first reports on their synthesization almost ten years ago [5]. In particular, promising technological applications of their giant magnetoresistive (GMR) properties make these systems very appealing. The material can be derived from RCoO$_{3-\epsilon}$ by taking two formula units and replacing a trivalent R in one of them and by divalent barium. The oxygen content is reduced by $\epsilon = (1 - \delta)/2$, so the cobalt ions take an average valence of $2.5 + \delta$. As is shown in figure 5.1(a), the R and Ba ions order alternatingly along the crystallographic c axis. This results in a doubling of the unit cell with respect to the approximately cubic perovskite parent compound. Cobalt ions are surrounded by six oxygen ions forming octahedra which are corner sharing connected. At an oxygen vacancy, two octahedra are disconnected and truncated to pyramids.

In the special case of $\delta = 0.5$, for which every fourth perovskite cube misses an oxygen, the vacancies order on a square lattice in bc plane. This means, layers of octahedra and pyramids parallel to the ac plane alternate in b direction. Thereby another doubling of the unit cell is introduced. In this case, only one species of cobalt ions, namely Co^{3+} is present, in contrast to the famous CMR perovskites La$_{1-x}A_x$MnO$_3$, A = earth alkaline, or La$_{1-x}$Sr$_x$CoO$_3$ which involve transition metal ions of different valence. Therefore the double exchange mechanism, which has been proposed to explain the CMR effect in those systems [3, 4, 141, 142], is not applicable in RBaCo$_2$O$_{5+\delta}$, $\delta = 0.5$. On the other hand, the trivalent cobalt ion has a $3d^6$ electronic configuration introducing an additional spin state degree of freedom. It depends on the relative strength of the exchange coupling due to Hund's rule, J_{H}, compared to the cubic crystal field splitting $10Dq$ of the $3d$ electrons, as is detailed in chapter 2. For large crystal field splitting, all six electrons occupy the lower lying t_{2g} orbitals, and the Co ions take an $S = 0$ low–spin state. On the other hand, in a weak crystal field the electrons prefer a high–spin state, $S = 2$, due to Hund's rule. Another possible configuration is the intermediate–spin state with $S = 1$. For trivalent cobalt ions in octahedral coordination of oxygen ions like in LaCoO$_3$,
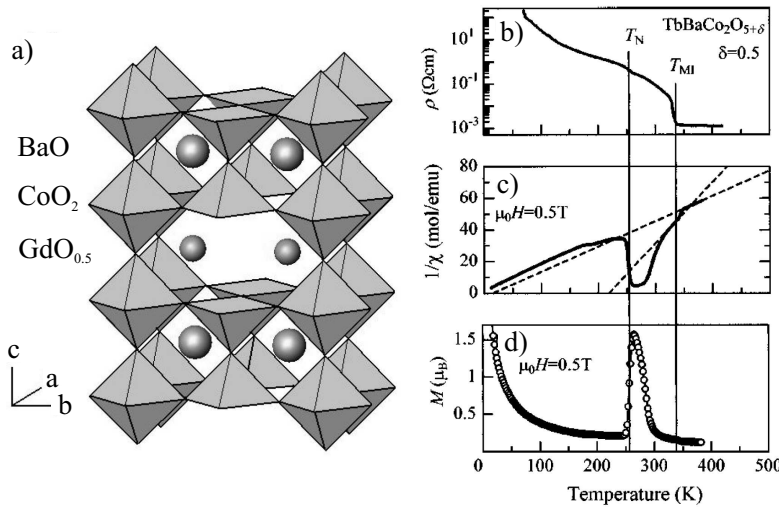
Figure 5.1: (a) The crystal structure of GdBaCo$_2$O$_{5.5}$: big spheres represent Ba, small ones Gd; Co ions reside in octahedra and pyramids formed by oxygen (not shown) (from Taskin *et al.* [140]). (b) Resistivity and (c,d) magnetism of RBaCo$_2$O$_{5+\delta}$, R = Tb, $\delta = 0.5$ from Moritomo *et al.* [54].

the ground state has a LS configuration. However, the energy separation to the excited states is so small that at room temperature a significant amount of cobalt ions may occupy the higher spin states. This so–called spin state transition has been discussed extensively for a wide range of cobaltate systems in the past. The situation is likely to change for cobalt ions in pyramidal coordination because of a reduction of the crystal field [143, 144]. This change in the delicate balance with the exchange interaction stabilizes the higher spin states and may possibly suppress the transition.

Besides the GMR effect, the class of RBaCo$_2$O$_{5+\delta}$ compounds shows a number of interesting phenomena and anomalies in electrical and magnetic properties. As an example, the resistivity and magnetic properties of the system with R = Tb, $\delta = 0.5$ is shown on the right in figure 5.1 [54]. A macroscopic magnetic moment appears in a narrow temperature region of a few tens of degrees below a transition temperature $T_c = 260 - 300$ K depending on composition, see figure 5.1(d). Furthermore, a metal to insulator transition has been reported in a very narrow range of $\delta = 0.5 \pm 0.1$ with a drop in the resistivity of an order of magnitude at transition temperatures in the range of $T_{\mathrm{MIT}} = 300 - 360$ K [145, 146], see figure 5.1(b). At the same time, the lattice parameters a and b become anisotropic. Maignan *et al.* have tried to explain the various phenomena [145]. They discuss a magnetic transition at T_{MIT} from paramagnetic to ferromagnetic or canted antiferromagnetic and propose as a mechanism for the magnetic transition a spin state transition from LS in the octahedral sites and IS in the pyramids at low temperature to HS for both. The magnetic susceptibility in fact reveals a finite ferromagnetic moment for all systems with $\delta > 0$ (i. e. even those that do not show a MIT), though only at considerably lower temperatures. On the other hand, a sharp bend in the inverse susceptibility at T_{MIT} is taken as evidence for the transition, see figure 5.1(c). However, this kink is also observed for R = Ho, $\delta = 0.3$ in which the MIT does not appear. The linear behaviour of the inverse susceptibility extrapolated to high temperatures is suggestive of a Curie–Weiss law. This is interpreted as antiferromagnetic interaction competing with the ferromagnetism and suppressing it at lower temperatures. It has to be noted that the inverse of the susceptibility is not necessarily a meaningful

quantity in terms of a Curie–Weiss law. The total magnetic moment is composed of contributions from the different constituents in these systems, in particular the rare earth ions, which are difficult to account for. Thus it is unclear whether the observed discontinuity in the inverse susceptibility is related to changes in the spin state of the cobalt ions, or if it is simply a consequence of the changes in the electronic properties due to the MIT.

After this early proposal, a long list of publications have addressed the question of the MIT in the layered perovskite cobaltates, many of which discussing different models involving ordering and/or transition of spin states [54, 140, 147–153]. For instance, a recently proposed spin blockade mechanism makes explicit assumptions about the ordering and a transition of the spin states in order to explain the MIT [151]. Most of the experimental investigations consider the spin state of pyramidal site Co^{3+} ions to be IS, while the spin state of the octahedral sites is claimed to make a transition from LS at low temperatures to a higher spin state. In contrast, band structure calculations find all Co ions in the HS, for high as well as the low temperature phase [154]. In this description, orbital ordering of minority spin t_{2g} orbitals is proposed below the MIT. An improved structural determination of $GdBaCo_2O_{5.5}$ by means of x–ray diffraction brought about a weak super structure at temperatures $T \lesssim T_{MIT}$, corresponding to a distortion of the oxygen sublattice [153]. From the displacements of the oxygen ions, an IS/HS chequerboard ordering in the pyramidal sites, together with orbitally ordered IS in the octahedra is proposed. The refined structural data has an effect also on the results of the band structure calculations. Unpublished results show that while the pyramidal sites are unaffected, the octahedral sites display a LS/HS ordering of chequerboard type in ac plane at $T = 0$ K [155]. This ordering is assumed to be quite unstable as temperature rises due to thermal depopulation of the LS on the one hand, and lattice relaxation in favour of HS on the other hand.

The multitude of different descriptions in the literature has created considerable confusion. Since all the mentioned experimental studies base their conclusions on measurements of transport and magnetic properties as well as diffraction, there is hope that direct information on the electronic structure from spectroscopy can help to resolve the puzzle. It has to be noted that most of the publications have not taken into account recent spectroscopic results for the spin state of cobalt ions in a pyramidal environment being HS at all temperatures instead of IS [144], a finding which is supported by certain band structure calculations [143, 156]. Besides, only little spectroscopic material is available so far, and the significance of the existing data is strongly reduced due to experimental shortcomings. Low photon–energy investigations, for instance, proposed the presence of some IS or HS component down to $T = 50K$ [157]. The use of low photon energy in combination with a rough scraped surface is known to enhance the surface sensitivity of the photoemission spectra. As is described in detail in chapter 2, this is particularly problematic for cobaltates, because the spin state of the bulk may not correspond to that on the surface. Another approach using high photon energy of $h\nu = 1486.6$ eV avoids these difficulties, but does not give solid answers because of the poor experimental resolution [158]. As a result, these studies do not make precise statements about whether or not there is a spin state transition.

In order to get detailed and reliable information on the electronic structure of the layered cobaltates and its temperature dependence, we have performed bulk sensitive photoemission measurements on high quality single crystals of GdBaCo$_2$O$_{5.5}$ in the temperature range of 80 – 380 K.

5.2   Experimental

Single crystals of GdBaCo$_2$O$_{5.5}$ are provided by S. N. Barilo. The preparation of these samples and the characterization of their magnetic and transport properties have been described in a previous publication of Zhou *et al.* [159], and detailed structural analyses were performed by Chernenkov *et al.* [152]. Precise oxygen content determination by iodometric titration results in $\delta = 0.47 \pm 0.02$. Photoemission spectra were recorded at beam line ID08 of the ESRF, Grenoble, using 700 eV photons and a Scienta SES 2002 electron energy analyzer. The overall experimental resolution was set to 110 meV. For the calibration of binding energies, Fermi cut–off spectra of polycrystalline silver have been taken for all temperatures. Samples were cleaved *in situ* and measured at normal emission at 80 K, 300 K and 380 K. Room temperature spectra taken after every high and low temperature measurements have shown to be reproducible. In order certify the sample quality, x–ray absorption spectra on the Co–$L_{2,3}$ and O–K edges have been taken repeatedly. The base pressure in the spectrometer chamber was kept in the low 10^{-10} mbar range throughout the measurement. Samples and measurement of LaCoO$_3$ are described in detail in chapter 2.

5.3   Results and Discussion

We show a survey spectrum of GdBaCo$_2$O$_{5.5}$ in figure 5.2. The room temperature spectrum taken with high photon energy of 700 eV (top, solid line) is displayed together with the low photon energy results of Flavell *et al.* (dashed, bottom) [157]. In the high photon energy spectrum, the contributions of the different constituents, especially gadolinium and barium, can be identified much more unambiguously. The spectrum is dominated by the Gd $4f$ peak at 7.8 eV binding energy which shows the characteristic asymmetric line shape of the $4f$ multiplet [160]. We observe also clearly the spin–orbit split Ba $5p$ contribution at 12.3 and 14.3 eV, as well as the overlapping O $2s$ and Gd $5p$ core levels in the range of 17 – 24 eV. As was shown by band structure calculations, the valence band spectral weight is made up of Co $3d$ and O $2p$ contributions almost exclusively [154]. In contrast, the low photon energy spectrum does not show corresponding structures. This discrepancy is presumably due to disadvantageous enhanced oxygen cross sections and the increased surface sensitivity of the spectra. In particular, the assignment of distinct structures (A–I), especially in the region from E_{F} to 2 eV binding energy as claimed by Flavell *et al.* does not appear to be meaningful.

A blow–up of the valence band region is displayed in figure 5.3. We show the spectra taken at 80 K, corresponding to the low temperature phase below the magnetic transition, and in the high temperature paramagnetic phase at 300 and 380
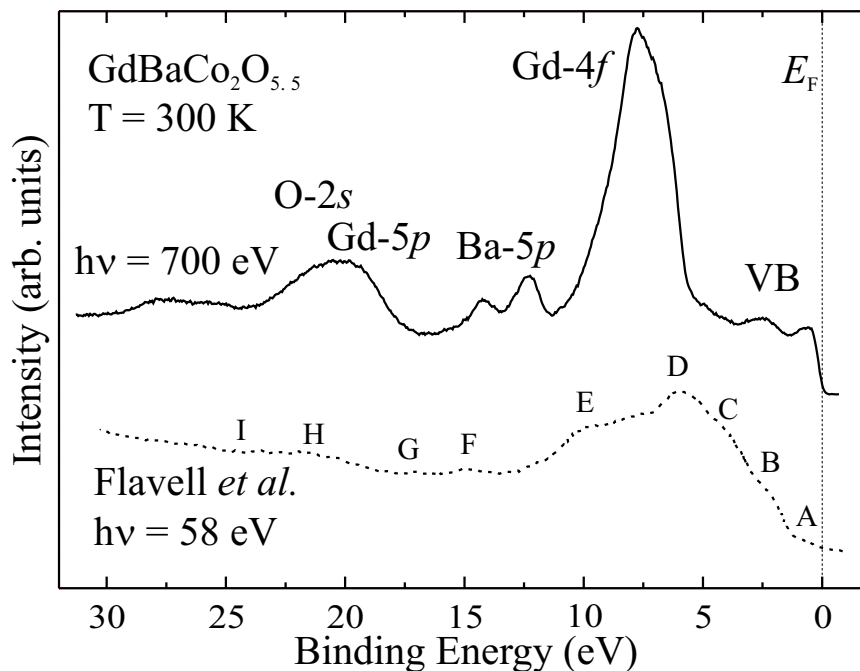
Figure 5.2: Solid line: overview spectrum of GdBaCo$_2$O$_{5.5}$ at 300 K, taken with 700 eV photons. Dashed line: the low photon energy spectrum from Flavell *et al.* in the same energy range with the assignment of nine structures A – I [157].

K, i.e. both below and above the MIT. A noticeable temperature dependence is observed only at binding energies below 1.5 eV. In the low temperature spectrum, a weak structure at 0.6 eV binding energy is observed, the weight of which is continuously decreased as temperature rises. Moreover, a transfer of spectral weight to lower binding energies of ≤ 0.3 eV is observed with rising temperature. The amount of transferred spectral weight is quite small and in particular does not lead to a complete closing of the gap at least at temperatures as high as 380 K. We cannot observe a clear Fermi cut-off. This means, that the system does actually not become a real metal. Rather it makes a gradual transition from a low temperature ($< T_{\mathrm{MIT}}$) insulating phase to a higher temperature, still insulating one with a smaller gap. It is conducting, but as a very bad metal. The claimed observation of the gap closing in a previous XPS investigation of TbBaCo$_2$O$_{5.5}$ can be explained by the poor experimental resolution of the data which artificially reveals spectral weight above E_{F} [158].

The very weak temperature dependence of the valence band spectra is particularly interesting in terms of the spin state of the cobalt ions and a possible spin state transition. The presence of a LS contribution can be seen as a sharp and pronounced peak at 1 eV binding energy. As we have shown for LaCoO$_3$, a spin state transition from LS to a higher spin state appears in a decrease of the weight of this peak as temperature rises, see chapter 2. For comparison, the low temperature valence band spectrum of LaCoO$_3$ is shown together with the low temperature spectrum of GdBaCo$_2$O$_{5.5}$ in figure 5.4. The dominant LS peak at 1 eV in the LaCoO$_3$ spectrum (dashed line) is clearly absent in the spectrum of GdBaCo$_2$O$_{5.5}$ (solid line). Any
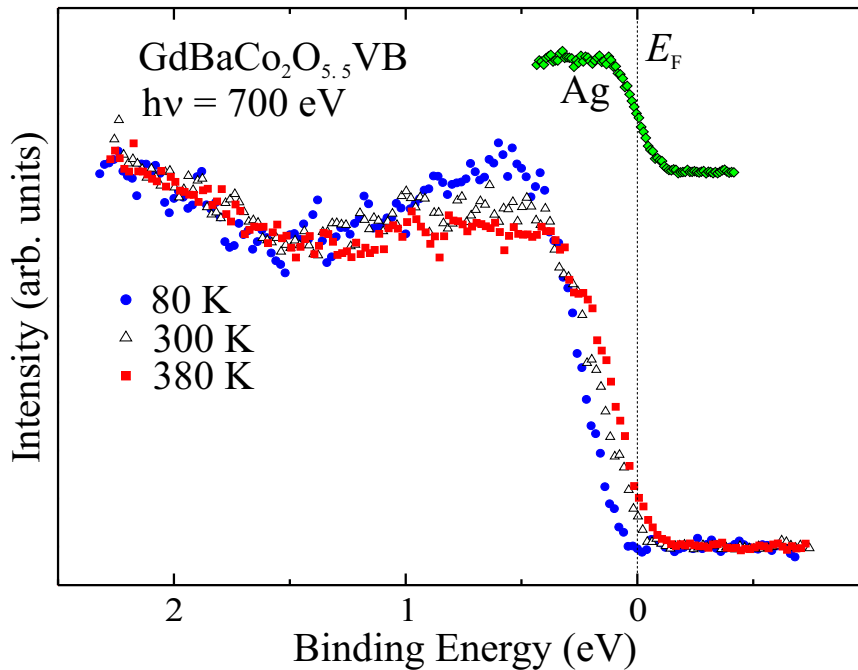
Figure 5.3: Valence band spectra of GdBaCo$_2$O$_{5.5}$ taken with 700 eV photons at 80 K (blue circles), 300 K (open triangles) and 380 K (red squares), together with a silver reference Fermi cut–off spectrum.

LS contribution in the latter must therefore be significantly smaller than 50%, in contradiction to most of the current models involving spin state transitions at the octahedral sites. A small LS contribution might be seen in the weak feature at 0.6 eV which shows a noticeable temperature dependence. However, this structure lies too low in binding energy compared to LaCoO$_3$. On the other hand, the two spectra align perfectly when the LaCoO$_3$ spectrum is shifted up by 0.4 eV to E_F. Then the top of the valence band lies at E_F, and the LS peak coincides with the weak structure in the low temperature GdBaCo$_2$O$_{5.5}$ spectrum. This surprising observation could be meaningless, though, because the HS contribution will be very different in the two systems, and therefore the matching at higher energies could be coincidental.

In order to quantify our results, we have simulated the Co $3d$ spectral weight in configuration–interaction cluster calculations performed for a CoO$_6$ octahedron (see figure 5.5 top right), assuming various ratios of spin states to contribute to the spectra. The calculations were performed using the values of $U_{dd} = 5.5$ eV for the on–site Coulomb repulsion between Co $3d$ electrons, the charge transfer energy $\Delta = 2.0$ eV and the Co $3d$–O $2p$ hopping integral $pd\sigma = -1.7$ eV, as determined from core level spectroscopy of LaCoO$_3$ [45], as well as the crystal field splitting $10Dq = 0.8$ eV and an O $2p$–O $2p$ hopping parameter $t_{pp} = 0.5$ eV, in accordance with x–ray absorption spectroscopy [57]. The calculated spectra are shown in figure 5.5, at the bottom the pure LS (black), IS (red) and HS (green) spectra, as well as the simulated spectra for equal occupation of LS and IS (a), equal occupation of LS and HS (b), and 25% LS : 75% HS occupation (c), separated by a constant offset for a clearer presentation. First of all we note that the pure LS spectrum
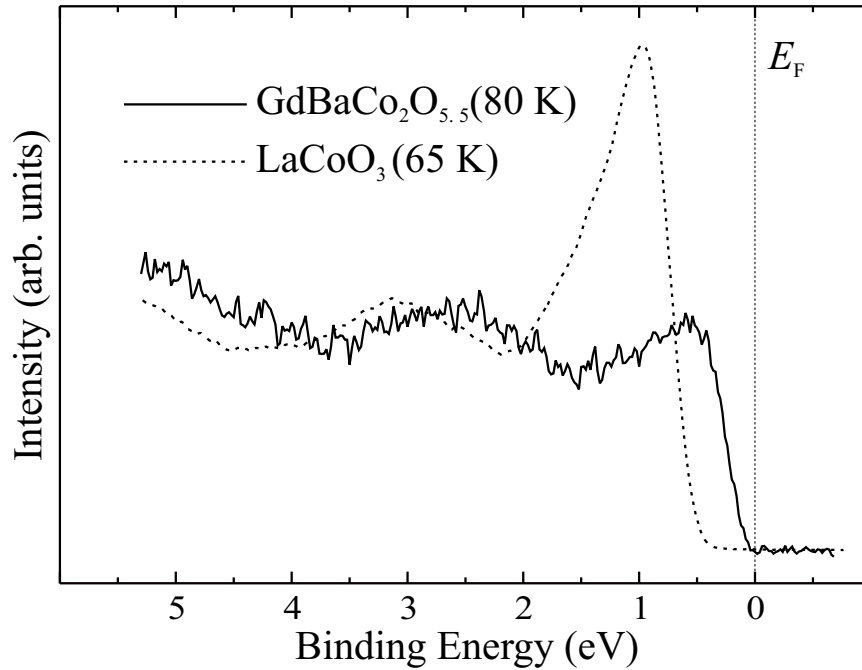
Figure 5.4: Valence band spectra of $GdBaCo_2O_{5.5}$ at 80 K (solid line) in comparison with $LaCoO_3$ at 65 K (dashed), both taken with a photon energy of 700 eV.

displays a pronounced peak at 1 eV binding energy, in contrast to the IS and HS spectra. This peak can be clearly observed in the low temperature spectrum of $LaCoO_3$, unlike $GdBaCo_2O_{5.5}$, see figure 5.4. In the simulations assuming a 50% occupation of LS, with the remaining Co sites taking either IS or HS, the 1 eV LS peak is still dominant. This result is obviously incompatible with the experimental spectra. Thus all the models, which assume a spin state ordering of a higher spin in the pyramidal sites, and the octahedral sites in the LS at low temperature, must be invalid. As a consequence, the proposed spin state transition in the octahedral sites from LS to a higher spin state, cannot take place. On the other hand, the simulation assuming 25% LS and 75% HS occupation qualitatively matches the experimental results in the sense that not a sharp peak but a broad, flat structure is shown in the range of up to 1 eV binding energy. It is important to note that the cluster calculations for a CoO_5 pyramid yield qualitatively very similar results, since only the orbitals pointing towards the oxygen vacancy are affected. But for a realistic simulation of the spectrum, the oxygen $2p$ contribution has to be taken into account. However, this is considered also to have only little effect in the low binding energy range, as the strongly oxygen–sensitive low photon energy spectra shown in figure 5.2 demonstrate. Therefore, we can give an upper bound of 25% for the LS contribution at $T = 80$ K. This result is consistent with the scenario of HS pyramidal sites with a LS/HS ordering in the octahedral sites at $T = 0$ K, as proposed by band structure calculations [155]. With increasing temperature, the LS will be depopulated in favour of the HS. Moreover, both off–stoichiometry, i. e. $\delta \neq 0.5$, and lattice distortions may reduce the LS occupation from the proposed 25% already at low temperatures, in line with the weak temperature dependence of
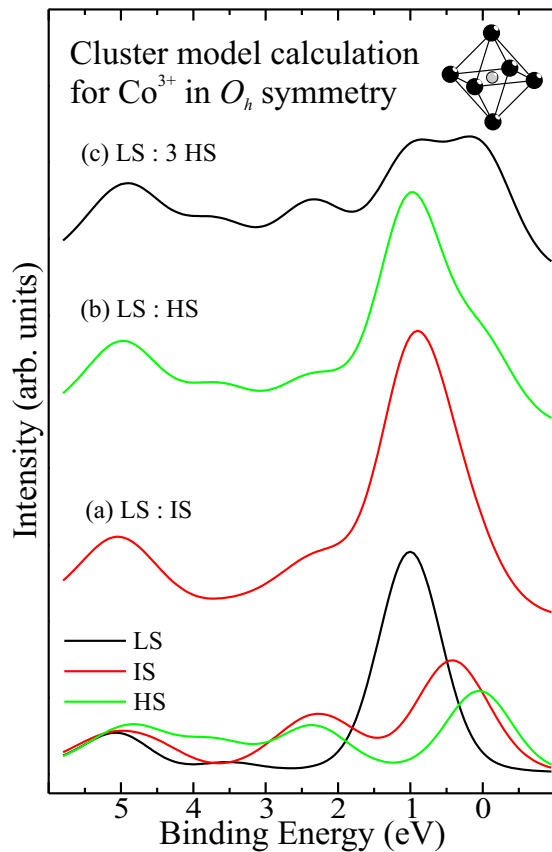
Figure 5.5: Configuration–interaction cluster model calculation of the $3d$ PES spectral weight for a Co^{3+} in O_h symmetry, see top right (black spheres denote O^{2-}, small grey sphere Co^{3+}). At the bottom, the spectra of the pure LS (black line), IS (red) and HS (green) are shown. Simulated spectra for (a) equal occupation of LS : IS (b) equal occupation of LS : HS and (c) 25% LS : 75% HS occupation have been shifted up by a constant offset for clearer presentation.

the experimental spectra.

5.4   Conclusions

We have carried out a bulk sensitive high resolution photoemission investigation of the layered perovskite GdBaCo$_2$O$_{5.5}$ in the temperature range of 80 – 380 K. We find, first of all, that the gap is not completely closed up to 380 K, there is at least no clear Fermi cut–off. This means the high temperature phase above T_{MIT} is actually not a good metal. Opposite claims of previous XPS investigations of TbBaCo$_2$O$_{5.5}$ are considered erroneous as a result of poor experimental resolution.

On the basis of configuration–interaction cluster model calculations for a CoO$_6$ octahedron, we can derive from the line shape and the weak temperature dependence an upper bound for the LS contribution of 25% at 80 K. This result is consistent with a spin state ordering of LS/HS in the octahedral sites at $T = 0$ K, and HS in the pyramidal sites at all temperatures, as proposed by a novel model currently developed on the basis of a combined approach of x–ray absorption spectroscopy and band structure calculations [155, 161].

Summary

Modern solid state research has focused to a considerable extent on the physics of strongly correlated electron systems, because here we find interesting phenomena arising from conditions far away from well understood limiting cases. Being such systems, the transition metal oxides have shown to be a very wide ranged field for researchers to find unexpected properties like unconventional superconductivity in the high-T_c cuprates [1] and the ruthenates [2], large magnetoresistance effects in manganites (CMR) [3], and cobaltates (GMR) [4, 5], as well as unusual phase transitions like metal-insulator- [6] or spin-state transitions [7], and many more. Transition metal oxides hence represent model systems for the development of theoretical descriptions, and therefore are essential for the progress of our understanding of nature. At the same time, the physical properties found in these materials are invaluable for technological applications, and in some cases even open up completely new possibilities. These properties can often be tuned in a wide range by external parameters like temperature, pressure, external electric or magnetic fields, or composition, e. g. by doping. In order to optimize the properties of a material for a specific application, a solid understanding of their physics is required.

The characteristics of a solid are to a large extent determined by the electronic structure. This includes the electronic configuration of the ground state of the system, as well as electronic excitations, which are responsible for the macroscopic properties like resistivity, magnetism and so on. The experimental investigation of the electronic structure is therefore an essential part in the attempt to understand the physical properties of a material. Photoelectron spectroscopy is a well established tool to investigate the electronic structure of solids and solid surfaces [8–10]. A key characteristic of this technique is its inherent surface sensitivity. This is advantageous for the study of surfaces and ultra thin films, but could be quite problematic for obtaining spectra which are representative of the bulk material, which we would like to study. This problem is most acute for strongly correlated materials, since their electronic structure depends strongly on their local environment: the properties of the bulk are very different from those of the near surface region. This thesis describes our efforts to obtain photoemission spectra which are representative of the bulk. We find data which are very different from the ones reported in the literature so far, thereby providing new insights important for the theoretical modeling.

We report in chapter 2 on a detailed study of the different contributions from surface and bulk to the valence band spectra of $LaCoO_3$ in the range from 65 K to room temperature, using photon energies between 450 eV and 6 keV and varying degrees of surface sensitivity. We observe a prominent low binding energy peak, which is characteristic of a Co^{3+} low spin state. The intensity of the peak is reduced

in going from low to high temperature. By contrast, previously published spectra of various groups do not show a pronounced peak in this energy region, and no temperature dependence up to room temperature either. We can show that the literature results are not representative for the bulk system. By analyzing the emission angle dependence of the spectra, we have been able to separate the bulk and surface contributions. We observe a temperature dependent, predominantly low-spin bulk spectrum, corresponding to the proposed spin state transition, in accordance with the magnetic susceptibility. At the same time, the surface is temperature independent. Based on the line shape analysis, we infer that the Co^{3+} ion at the surface is in a high spin state.

In chapter 3, we present a detailed study of the valence and conduction bands of VO_2 single crystals across the metal-insulator transition using bulk-sensitive photoelectron and O-K x–ray absorption spectroscopies. Our measurements reveal a giant transfer of spectral weight, much more pronounced than shown in previous reports, and even more than that in V_2O_3 [26]. Particular spectral features signal that the transition is not of the standard Peierls nor single-band Mott-Hubbard type. The valence band spectrum of the metallic phase is characterized by two structures in the V $3d$ contribution which can be identified with the coherent and incoherent parts of the spectrum. The symmetry and energies of the bands are discussed in connection to the recently determined orbital occupation [27] and to the importance of the k-dependence of the self-energy correction [28]. This analysis reveals the decisive role of the V $3d$ orbital degrees of freedom. The orbital switching is the key for opening a band gap that is much larger than the energy scale of the transition temperature. Comparison to recent realistic many body calculations within the dynamical mean field theory using a two-site cluster, shows that much of the k-dependence of the self-energy correction can be cast within a dimer model.

The results of the bulk-sensitive photoemission study of the low temperature insulating phase of Ti_2O_3 using both soft and hard x–ray photons are presented in chapter 4. We find in both the valence band and the Ti $2p$ core level spectra structures that have not been reported in the literature yet. The Ti $3d$ spectral weight displays a two peak structure in the insulating state, which can be identified with the bonding- and antibonding contributions associated with the c axis Ti–dimers in the crystal structure. Also in the Ti $2p$ core level spectra we observe additional satellites at lower binding energies. We can find qualitative understanding of these satellites in terms of non-local screening effects from the hydrogen molecule model.

Finally, in chapter 5 another cobaltate system, $GdBaCo_2O_{5.5}$, is presented. The Co ions possess the same $3d^6$ configuration as in $LaCoO_3$, however the distinct crystalline environment leads to considerably different properties. With a bulk-sensitive high resolution x–ray photoemission investigation in the temperature range of 80 - 380 K, we are able to give reliable information on the electronic properties and the temperature dependence of the spin state in this system. We find that the gap remains finite up to 380 K, implying that the high temperature phase above the so-called metal-insulator transition is actually not metallic, in contrast to opposite claims of previous XPS investigations of $TbBaCo_2O_{5.5}$. We show furthermore that a dominating low-spin contribution commonly claimed for the octahedral site at low

temperatures, does not show up in the valence band spectra. From the line shape and the weak temperature dependence in comparison with $LaCoO_3$, we can derive an upper bound for the low spin contribution of 25% at 80 K. These findings cast doubts on most of the current models proposed to explain the complex magnetic and transport behaviour of the layered cobaltates.

Our results of bulk-sensitive photoelectron spectroscopy on selected correlated materials demonstrate that indeed there is a need for this kind of investigations. A large number of systems yet remains to be studied in this respect for the future.

Zusammenfassung

Die moderne Festkörperforschung hat sich in großem Maße auf die Physik von Systemen stark korrelierter Elektronen konzentriert, da wir hier interessante Phänomene finden können, die aus Bedingungen weit ab von gut verstandenen Grenzfällen entspringen. Die Übergangsmetalloxidverbindungen sind solche Systeme, und erweisen sich daher als ein sehr umfangreiches Feld, in dem Forscher unerwartete Eigenschaften finden können, wie unkonventionelle Supraleitung in den High–T_c Kupraten [1] und den Ruthenaten [2], große Magnetwiderstandseffekte in Manganaten (CMR) [3] und Kobaltaten (GMR) [4, 5], sowie ungewöhnliche Phasenübergänge wie Metall–Isolator– [6] oder Spinzustandsübergänge [7] und viele weitere. Übergangsmetalloxide stellen folglich Modellsysteme für die Entwicklung theoretischer Beschreibungen dar, und sind deshalb wichtig für den Fortschritt unseres Verständnisses der Natur. Gleichzeitig sind die physikalischen Eigenschaften dieser Materialien unschätzbar für die technologische Anwendung, und eröffnen in einigen Fällen sogar ganz neue Möglichkeiten. Diese Eigenschaften können oft in einem weiten Bereich gezielt verändert werden durch äußere Parameter wie Temperatur, Druck, äußere elektrische oder magnetische Felder, oder die chemische Zusammensetzung, z.B. durch eine Dotierung. Um die Eigenschaften eines Materials für eine bestimmte Anwendung zu optimieren, ist ein solides Verständnis ihrer Physik erforderlich.

Die Charakteristika eines Festkörpers sind zu einem großen Teil durch seine elektronische Struktur bestimmt. Dies umfasst die elektronische Konfiguration des Grundzustandes des Systems, sowie elektronische Anregungen, die verantwortlich sind für makroskopische Eigenschaften wie Widerstand, Magnetismus und so weiter. Die experimentelle Untersuchung der elektronischen Struktur ist daher ein wesentlicher Bestandteil beim Versuch die physikalischen Eigenschaften eines Materials zu verstehen. Photoelektronenspektroskopie ist eine etablierte Methode zur Untersuchung der elektronischen Struktur von Festkörpern und Oberflächen [8–10]. Ein wesentliches Charakteristikum dieser Technik ist die immanente Oberflächenempfindlichkeit. Dies ist vorteilhaft für die Untersuchung von Oberflächen und ultradünnen Filmen, es könnte aber recht problematisch sein, wenn man Spektren erhalten möchte, die aussagekräftig sind für die Volumeneigenschaften, welche wir untersuchen möchten. Dieses Problem ist besonders schwer wiegend für stark korrelierte Materialien, da ihre elektronische Struktur stark von ihrer lokalen Umgebung abhängt: die Volumeneigenschaften sind sehr verschieden von denjenigen im Bereich nahe der Oberfläche. Diese Arbeit beschreibt unsere Anstrengungen, Photoemissionsspektren zu erhalten, die repräsentativ für das Volumenmaterial sind. Wir finden Daten, die sehr unterschiedlich sind zu den bisher

in der Literatur erschienenen, und dabei neue Einsichten gewähren, die wichtig sind
für die theoretische Modellierung.

Wir berichten in Kapitel 2 über die detaillierte Untersuchung der unterschiedlichen Beiträge von Oberfläche und Volumen zum Valenzbandspektrum von $LaCoO_3$ im Bereich von 65 K bis Raumtemperatur unter Verwendung von Photonenenergien zwischen 450 eV und 6 keV und mit verschiedenen Graden an Oberflächenempfindlichkeit. Wir beobachten einen markanten Peak bei niedriger Bindungsenergie, der charakteristisch ist für Co^{3+} im Niedrigspinzustand (low spin). Die Intensität dieses Peaks nimmt mit steigender Temperatur ab. Im Gegensatz dazu weisen früher veröffentlichte Ergebnisse verschiedener Gruppen weder einen ausgeprägten Peak in diesem Energiebereich auf, noch eine Temperaturabhängigkeit unterhalb der Raumtemperatur. Wir können zeigen, dass die Literaturergebnisse nicht repräsentativ für die Volumeneigenschaften sind. Durch die Analyse der Spektren in Abhängigkeit vom Emissionswinkel können wir die Oberflächen– und Volumenbeiträge trennen. Wir beobachten ein temperaturabhängiges und Niedrigspin–dominiertes Volumenspektrum, entsprechend dem vorhergesagten Spinzustandsübergang gemäß der magnetischen Suszeptibilität. Gleichzeitig ist die Oberfläche temperaturunabhängig. Aufgrund der Analyse der Linienform folgern wir, dass das Co^{3+}–Ion an der Oberfläche im Hochspinzustand ist.

In Kapitel 3 zeigen wir die detaillierte Untersuchung des Valenz– und Leitungsbands von VO_2–Einkristallen am Metall–Isolator–Übergang mittels volumenempfindlicher Photoelektronen– und $O–K$–Röntgenabsorptionsspektroskopie. Unsere Messungen zeigen einen enormen Transfer von spektralem Gewicht, viel ausgeprägter als in früheren Berichten und sogar noch deutlich mehr als in V_2O_3 [26]. Ungewöhnliche spektrale Merkmale zeigen an, dass der Übergang weder ein herkömmlicher Peierls– noch ein Einband–Mott–Hubbard–Typ ist. Das Valenzbandspektrum der metallischen Phase ist charakterisiert von zwei Strukturen im $V\ 3d$–Beitrag, die mit dem kohärenten und inkohärenten Beitrag des Spektrums identifiziert werden können. Die Symmetrie und Energien der Bänder werden diskutiert im Zusammenhang mit der kürzlich bestimmten orbitalen Besetzung [27] und der Bedeutung der k–Abhängigkeit der Selbstenergiekorrektur [28]. Diese Analyse enthüllt die entscheidende Rolle der orbitalen $V\ 3d$–Freiheitsgrade. Die orbitale Umbesetzung ist der Schlüssel für das Öffnen einer Bandlücke, die viel größer ist als die Energieskala der Übergangstemperatur. Der Vergleich mit jüngsten realistischen Vielteilchenrechnungen innerhalb der dynamischen Molekularfeldtheorie anhand eines Zweiplatzclusters zeigt, dass viel von der k–Abhängigkeit der Selbstenergiekorrektur in einem Dimermodell erfasst werden kann.

Die Ergebnisse der volumenempfindlichen Photoemissionsuntersuchung der isolierenden Tieftemperaturphase von Ti_2O_3 mittels sowohl weicher als auch harter Röntgenstrahlung werden in Kapitel 4 gezeigt. Wir finden sowohl im Valenzband– als auch im Ti $2p$–Rumpfniveauspektrum Strukturen, die bisher noch nicht in der Literatur berichtet worden sind. Das spektrale Gewicht von Ti $3d$ zeigt eine Zweipeakstruktur in der isolierenden Phase, die mit den bindenden und antibindenden Beiträgen identifiziert werden kann, welche mit den Ti–Dimeren auf der c–Achse in der Kristallstruktur verbunden sind. Wir beobachten auch im Ti $2p$–Rumpfniveauspektrum zusätzliche Satelliten bei niedrigeren Bindungsenergien. Wir

können ein qualitatives Verständnis dieser Satelliten im Rahmen von nicht–lokalen Abschirmungseffekten finden anhand des Wasserstoffmolekül–Modells.

Schließlich wird in Kapitel 5 ein weiteres Kobaltatsystem, das erst jüngst synthetisierte $GdBaCo_2O_{5.5}$, vorgestellt. Die Co–Ionen besitzen formal dieselbe $3d^6$–Konfiguration wie in $LaCoO_3$, allerdings führt die unterschiedliche kristalline Umgebung zu bemerkenswert anderen Eigenschaften. Mit einer volumenempfindlichen, hochauflösenden Röntgen–Photoemissionsuntersuchung im Temperaturbereich von $80 - 380$ K können wir zuverlässige Informationen über die elektronischen Eigenschaften und die Temperaturabhängigkeit des Spinzustands in diesem System liefern. Wir finden heraus, dass die Anregungslücke endlich bleibt bis 380 K, was darauf hindeutet dass die Hochtemperaturphase oberhalb des sogenannten Metall–Isolator–Übergangs in Wirklichkeit nicht metallisch ist, im Widerspruch zu gegenteiligen Behauptungen früherer XPS–Untersuchungen an $TbBaCo_2O_{5.5}$. Wir zeigen außerdem, dass ein dominierender Niedrigspinbeitrag, der allgemein für die Oktaederplätze bei tiefen Temperaturen behauptet wird, sich nicht in den Valenzbandspektren zeigt. Aus der Linienform und der schwachen Temperaturabhängigkeit im Vergleich mit $LaCoO_3$ können wir eine obere Schranke für den Niedrigspinbeitrag von 25% bei 80 K ableiten. Diese Befunde werfen Zweifel auf an den meisten der aktuell vorgeschlagenen Modelle um die komplexen magnetischen und Transporteigenschaften der geschichteten Kobaltate zu erklären.

Unsere Ergebnisse von volumenempfindlicher Photoelektronenspektroskopie an ausgewählten korrelierten Materialien demonstrieren, dass tatsächlich Bedarf nach solchen Untersuchungen besteht. Eine große Zahl von Systemen bleibt jedoch in dieser Hinsicht noch zu untersuchen in der Zukunft.

Bibliography

[1] J. G. Bednorz and K. A. Müller, Z. Phys. B **64**, 189 (1986).

[2] Y. Maeno, H. Hashimoto, K. Yoshida, S. Nishizaki, T. Fujita, J. G. Bednorz, and F. Lichtenberg, Nature **372**, 532 (1994).

[3] R. M. Kusters, J. Singleton, D. A. Keen, R. McGreevy, and W. Hayes, Physica B **155**, 362 (1989).

[4] S. Yamaguchi, H. Taniguchi, H. Takagi, T. Arima, and Y. Tokura, J. Phys. Soc. Jpn. **64**, 1885 (1995).

[5] C. Martin, A. Maignan, D. Pelloquin, N. Nguyen, and B. Raveau, Appl. Phys. Lett. **71**, 1421 (1997).

[6] M. Imada, A. Fujimori, and Y. Tokura, Rev. Mod. Phys. **70**, 1039 (1998).

[7] P. M. Raccah and J. B. Goodenough, Phys. Rev. **155**, 932 (1967).

[8] *Photoemission in Solids I*, Vol. 26 of *Topics in Applied Physics*, edited by M. Cardona and L. Ley (Springer–Verlag, Berlin, 1978).

[9] *Photoemission in Solids II*, Vol. 27 of *Topics in Applied Physics*, edited by L. Ley and M. Cardona (Springer–Verlag, Berlin, 1979).

[10] S. Hüfner, *Photoelectron Spectroscopy*, 2nd ed. (Springer–Verlag, Berlin, 1995).

[11] M. Prutton, *Introduction to Surface Physics* (Oxford University Press, Oxford, 1994).

[12] D. Briggs and M. P. Seah, *Practical surface analysis* (Wiley, Chichester, 1990), Vol. 1: Auger and X–ray photoelectron spectroscopy.

[13] A. Sekiyama, H. Fujiwara, S. Imada, S. Suga, H. Eisaki, S. I. Uchida, K. Takegahara, H. Harima, Y. Saitoh, I. A. Nekrasov, G. Keller, D. E. Kondakov, A. V. Kozhevnikov, T. Pruschke, K. Held, D. Vollhardt, and V. I. Anisimov, Phys. Rev. Lett. **93**, 156402 (2004).

[14] K. Kobayashi, M. Yabashi, Y. Takata, T. Tokushima, S. Shin, K. Tamasaku, D. Miwa, T. Ishikawa, H. Nohira, T. Hattori, Y. Sugita, O. Nakatsuka, A. Sakai, and S. Zaima, Applied Physics Letters **83**, 1005 (2003).

[15] Nucl. Instr. and Meth. A **547**, entire issue (2005).

[16] M. Taguchi, A. Chainani, K. Horiba, Y. Takata, M. Yabashi, K. Tamasaku, Y. Nishino, D. Miwa, T. Ishikawa, T. Takeuchi, K. Yamamoto, M. Matsunami, S. Shin, T. Yokoya, E. Ikenaga, K. Kobayashi, T. Mochiku, K. Hirata, J. Hori, K. Ishii, F. Nakamura, and T. Suzuki, Physical Review Letters **95**, 177002 (2005).

[17] C. Laubschat, E. Weschke, C. Holtz, M. Domke, O. Strebel, and G. Kaindl, Phys. Rev. Lett. **65**, 1639 (1990).

[18] A. Sekiyama, T. Iwasaki, K. Matsuda, Y. Saitoh, Y. Ônuki, and S. Suga, Nature **403**, 396 (2000).

[19] T. Yokoya, A. Chainani, T. Takahashi, H. Katayama-Yoshida, M. Kasai, and Y. Tokura, Phys. Rev. Lett. **76**, 3009 (1996).

[20] A. P. Mackenzie, S. R. Julian, A. J. Diver, G. J. McMullan, M. P. Ray, G. G. Lonzarich, Y. Maeno, S. Nishizaki3, and T. Fujita, Phys. Rev. Lett. **76**, 3786 (1996).

[21] A. Damascelli, D. H. Lu, K. M. Shen, N. P. Armitage, F. Ronning, D. L. Feng, C. Kim, Z.-X. Shen, T. Kimura, Y. Tokura, Z. Q. Mao, and Y. Maeno, Phys. Rev. Lett. **85**, 5194 (2000).

[22] J. W. Allen, S. J. Oh, O. Gunnarsson, K. Schönhammer, M. B. Maple, M. S. Torikachvili, and I. Lindau, Adv. Phys. **35**, 275 (1986).

[23] A. Fujimori, I. Hase, H. Namatame, Y. Fujishima, , Y. Tokura, H. Eisaki, S. Uchida, K. Takegahara, and F. M. F. de Groot, Phys. Rev. Lett. **69**, 1796 (1992).

[24] I. H. Inoue, I. Hase, Y. Aiura, A. Fujimori, Y. Haruyama, T. Maruyama, and Y. Nishihara, Phys. Rev. Lett. **74**, 2539 (1995).

[25] I. H. Inoue, O. Goto, H. Makino, N. E. Hussey, and M. Ishikawa, Phys. Rev. B **58**, 4372 (1998).

[26] J.-H. Park, Ph.D. thesis, University of Michigan, 1994.

[27] M. W. Haverkort, Z. Hu, A. Tanaka, W. Reichelt, S. Streltsov, M. A. Korotin, V. I. Anisimov, H. H. Hsieh, H.-J. Lin, C. T. Chen, D. I. Khomskii, and L. H. Tjeng, Phys. Rev. Lett. **95**, 196404 (2005).

[28] S. Biermann, A. Poteryaev, A. I. Lichtenstein, and A. Georges, Phys. Rev. Lett. **94**, 026404 (2005).

[29] G. H. Jonker and J. H. V. Santen, Physics **19**, 120 (1953).

[30] R. R. Heikes, R. C. Miller, and R. Mazelsky, Physics **30**, 1600 (1964).

[31] J. B. Goodenough, J. Phys. Chem. Solids **6**, 287 (1958).

[32] K. Takada, H. Sakurai, E. Takayama-Muromachi, F. Izumi, R. A. Dilanian, and T. Sasaki, Nature **422**, 53 (2003).

[33] G. Thornton, B. C. Tofield, and A. W. Hewat, J. Solid State Chem. **61**, 301 (1986).

[34] S. Yamaguchi, Y. Okimoto, H. Taniguchi, and Y. Tokura, Phys. Rev. B **53**, R2926 (1996).

[35] N. Menyuk, K. Dwight, and P. M. Raccah, J. Phys. Chem. Solids **28**, 549 (1967).

[36] J. B. Goodenough and P. M. Raccah, J. Appl. Phys. **36**, 1031 (1965).

[37] G. H. Jonker, J. Appl. Phys. **37**, 1424 (1966).

[38] V. G. Bhide, D. S. Rajoria, G. R. Rao, and C. N. R. Rao, Phys. Rev. B **6**, 1021 (1972).

[39] G. Thornton, A. F. Orchard, and C. N. R. Rao, J. Phys. C: Solid State Phys. **9**, 1991 (1976).

[40] B. W. Veal and D. J. Lam, J. Appl. Phys. **49**, 1461 (1978).

[41] M. Abbate, J. C. Fuggle, A. Fujimori, L. H. Tjeng, C. T. Chen, R. Potze, G. A. Sawatzky, H. Eisaki, and S. Uchida, Phys. Rev. B **47**, 16124 (1993).

[42] R. H. Potze, G. A. Sawatzky, and M. Abbate, Phys. Rev. B **51**, 11501 (1995).

[43] M. A. Korotin, S. Y. Ezhov, I. V. Solovyev, V. I. Anisimov, D. I. Khomskii, and G. A. Sawatzky, Phys. Rev. B **54**, 5309 (1996).

[44] K. Asai, A. Yonedaa, O. Yokokura, J. M. Tranquada, G. Shirane, and K. Kohn, J. Phys. Soc. Jpn. **67**, 290 (1998).

[45] T. Saitoh, A. E. Bocquet, T. Mizokawa, and A. Fujimori, Phys. Rev. B **52**, 7934 (1995).

[46] T. Arima and Y. Tokura, J. Phys. Soc. Jpn. **64**, 2488 (1995).

[47] A. Chainani, M. Mathew, and D. D. Sarma, Phys. Rev. B **46**, 9976 (1992).

[48] T. Saitoh, T. Mizokawa, A. Fujimori, M. Abbate, Y. Takeda, and M. Takano, Phys. Rev. B **55**, 4257 (1997).

[49] Y. Tokura, Y. Okimoto, S. Yamaguchi, H. Taniguchi, T. Kimura, and H. Takagi, Phys. Rev. B **58**, R1699 (1998).

[50] P. G. Radaelli and S.-W. Cheong, Phys. Rev. B **66**, 094408 (2002).

[51] C. Zobel, M. Kriener, D. Bruns, J. Baier, M. Grüninger, T. Lorenz, P. Reutler, and A. Revcolevschi, Phys. Rev. B **66**, 020402 (2002).

[52] P. L. Kuhns, M. J. R. Hoch, W. G. Moulton, A. P. Reyes, J. Wu, and C. Leighton, Phys. Rev. Lett. **91**, 127202 (2003).

[53] A. Ishikawa, J. Nohara, and S. Sugai, Phys. Rev. Lett. **93**, 136401 (2004).

[54] Y. Moritomo, T. Akimoto, M. Takeo, A. Machida, E. Nishibori, M. Takata, M. S. K. Ohoyama, and A. Nakamura, Phys. Rev. B **61**, R13325 (2000).

[55] D. J. Goossens, K. F. Wilson, M. James, A. J. Studer, and X. L. Wang, Phys. Rev. B **69**, 134411 (2004).

[56] K. Knížek, Z. Jirák, J. Hejtmánek, and P. Novák, J. Phys.: Condens. Matter **18**, 3285 (2006).

[57] M. W. Haverkort, Z. Hu, J. Cezar, T. Burnus, H. Hartmann, M. Reuther, C. Zobel, T. Lorenz, A. Tanaka, N. B. Brookes, H. H. Hsieh, H.-J. Lin, C. T. Chen, and L. H. Tjeng, accepted by Phys. Rev. Lett. 2006 (unpublished).

[58] L. Richter, S. D. Bader, and M. B. Brodsky, Phys. Rev. B **22**, 3059 (1980).

[59] S. R. Barman and D. D. Sarma, Phys. Rev. B **49**, 13979 13982 (1994).

[60] A. G. Thomas, W. R. Flavell, P. M. Dunwoody, C. E. J. Mitchell, S. Warren, S. C. Grice, P. G. D. Marr, D. E. Jewitt, N. Khan, V. R. Dhanak, D. Teehan, E. A. Seddon, K. Asai, Y. Koboyashi, and N. Yamada, J. Phys.: Condens. Matter **12**, 9259 (2000).

[61] J.-Q. Yan, J.-S. Zhou, and J. B. Goodenough, Phys. Rev. B **70**, 014402 (2004).

[62] C. Zobel, Ph.D. thesis, II. Physikalisches Institut, Universität zu Köln, 2002.

[63] P. Torelli, M. Sacchi, G. Cautero, M. Cautero, B. Krastanov, P. Lacovig, P. Pittana, R. Sergo, R. Tommasini, A. Fondacaro, F. Offi, G. Paolicelli, G. Stefani, M. Grioni, R. Verbeni, G. Monaco, and G. Panaccione, Rev. Sci. Instrum. **76**, 023909 (2005).

[64] S. Thiess, C. Kunz, B. C. C. Cowie, T.-L. Lee, M. Renier, and J. Zegenhagen, Solid State Commun. **132**, 589 (2004).

[65] G. Panaccione, G. Cautero, M. Cautero, A. Fondacaro, M. Grioni, P. Lacovig, G. Monaco, F. Offi, G. Paolicelli, M. Sacchi, N. Stojić, G. Stefani, R. Tommasini, and P. Torelli, J. Phys.: Condens. Matter **17**, 2671 (2005).

[66] J. J. Yeh and I. Lindau, At. Data Nucl. Data Tables **32**, 1 (1985).

[67] J. H. Scofield, Theoretical Photoionization Cross Sections from 1 to 1500 keV, Report UCRL-51326, Lawrence Livermore Laboratory, University of California, 1973.

[68] T. C. Koethe, Z. Hu, M. W. Haverkort, C. Schussler-Langeheine, F. Venturini, N. B. Brookes, O. Tjernberg, W. Reichelt, H. H. Hsieh, H.-J. Lin, C. T. Chen, and L. H. Tjeng, Phys. Rev. Lett. **97**, 116402 (2006).

[69] J. B. Goodenough, J. Solid State Chem. **3**, 490 (1971).

[70] N. F. Mott, *Metal–insulator Transitions*, 2nd ed. (Taylor & Francis, London, 1990).

[71] F. J. Morin, Phys. Rev. Lett. **3**, 34 (1959).

[72] M. Marezio, D. B. McWhan, J. P. Remeika, and P. D. Dernier, Phys. Rev. B **5**, 2541 (1972).

[73] P. B. Allen, R. M. Wentzcovitch, W. W. Schulz, and P. C. Canfield, Phys. Rev. B **48**, 4359 (1993).

[74] C. N. Berglund and H. J. Guggenheim, Phys. Rev. **185**, 1022 (1969).

[75] A. Tanaka, J. Phys. Soc. Jpn. **73**, 152 (2004).

[76] K. Kosuge, J. Phys. Soc. Jpn. **22**, 551 (1967).

[77] J. B. Goodenough, Phys. Rev. **117**, 1442 (1960).

[78] D. Adler and H. Brooks, Phys. Rev. **155**, 826 (1967).

[79] R. M. Wentzcovitch, W. W. Schulz, and P. B. Allen, Phys. Rev. Lett. **72**, 3389 (1994).

[80] J. P. Pouget, H. Launois, J. P. D'Haenens, P. Merenda, and T. M. Rice, Phys. Rev. Lett. **35**, 873 (1975).

[81] J. P. Pouget, H. Launois, T. M. Rice, P. Dernier, A. Gossard, G. Villeneuve, and P. Hagenmuller, Phys. Rev. B **10**, 1801 (1974).

[82] A. Zylbersztejn and N. F. Mott, Phys. Rev. B **11**, 4383 (1975).

[83] T. M. Rice, H. Launois, and J. P. Pouget, Phys. Rev. Lett. **73**, 3042 (1994).

[84] C.-O. Almbaldh and L. Hedin, in *Handbook on Synchrotron Radiation*, edited by E. E. Koch (Elsevier Science Ltd., Amsterdam, 1983), Vol. 1, Part B, p. 607.

[85] G. A. Sawatzky and D. Post, Phys. Rev. B **20**, 1546 (1979).

[86] S. Shin, S. Suga, M. Taniguchi, M. Fujisawa, H. Kanzaki, A. Fujimori, H. Daimon, Y. Ueda, K. Kosuge, and S. Kachi, Phys. Rev. B **41**, 4993 (1990).

[87] M. S. E. Goering, O. Müller, R. Barth, H. Paulin, M. Klemm, M. L. denBoer, and S. Horn, Phys. Rev. B **55**, 4225 (1997).

[88] E. Goering, M. Schramme, O. Müller, H. Paulin, M. Klemm, M. L. denBoer, and S. Horn, Physica B **230 - 232**, 996 (1997).

[89] E. Z. Kurmaev, V. M. Cherkashenko, Y. M. Yarmoshenko, S. Bartkowski, A. V. Postnikov, M. Neumann, L.-C. Duda, J. H. Guo, J. Nordgren, V. A. Perelyaev, and W. Reichelt, J. Phys.: Condens. Matter **10**, 4081 (1998).

[90] K. Okazaki, H. Wadati, A. Fujimori, M. Onoda, Y. Muraoka, and Z. Hiroi, Phys. Rev. B **69**, 165104 (2004).

[91] V. Eyert, Ann. Physik **11**, 650 (2002).

[92] M. A. Korotin, N. A. Skorikov, and V. I. Anisimov, Phys. Met. Metallogr. **94**, 17 (2002).

[93] M. Korotin, N. Skorikov, and V. Anisimov, cond–mat/0301347 v1 (2003).

[94] A. Liebsch, H. Ishida, and G. Bihlmayer, Phys. Rev. B **71**, 085109 (2005).

[95] M. S. Laad, L. Craco, and E. Müller-Hartmann, Europhys. Lett. **69**, 984 (2005).

[96] W. Brückner, H. Oppermann, W. Reichelt, J. I. Terukow, F. A. Tschudnowski, and E. Wolf, *Vanadiumoxide* (Akademie–Verlag, Berlin, 1983).

[97] E. Weschke, C. Laubschat, T. Simmons, M. Domke, O. Strebel, and G. Kaindl, Phys. Rev. B **44**, 8304 (1991).

[98] A. Shigemoto, S. Suga, A. Sekiyama, S. Imada, A. Yamasaki, A. Irizawa, S. Kasai, T. Muro, Y. Saitoh, Y. Ueda, and K. Yoshimura, J. Electron Spectrosc. Relat. Phenom. **144-147**, 837 (2005).

[99] S.-K. Mo, J. D. Denlinger, H.-D. Kim, J.-H. Park, J. W. Allen, A. Sekiyama, A. Yamasaki, K. Kadono, S. Suga, Y. Saitoh, T. Muro, P. Metcalf, G. Keller, K. Held, V. Eyert, V. I. Anisimov, and D. Vollhardt, Phys. Rev. Lett. **90**, 186403 (2003).

[100] J.-H. Park, L. H. Tjeng, A. Tanaka, J. W. Allen, C. T. Chen, P. Metcalf, J. M. Honig, F. M. F. de Groot, and G. A. Sawatzky, Phys. Rev. B **61**, 11506 (2000).

[101] L. A. Ladd and W. Paul, Solid State Commun. **7**, 425 (1969).

[102] F. M. F. de Groot, M. Grioni, J. C. Fuggle, J. Ghijsen, G. A. Sawatzky, and H. Petersen, Phys. Rev. B **40**, 5715 (1989).

[103] M. Abbate, F. M. F. de Groot, J. C. Fuggle, Y. J. Ma, C. T. Chen, F. Sette, A. F. Y. Ueda, and K. Kosuge, Phys. Rev. B **43**, 7263 (1991).

[104] D. R. Penn, Phys. Rev. Lett. **42**, 921 (1979).

[105] L. A. Feldkamp and L. C. Davis, Phys. Rev. Lett. **43**, 151 (1979).

[106] L. C. Davis and L. A. Feldkamp, Phys. Rev. B **23**, 6239 (1981).

[107] U. Fano, Phys. Rev. **124**, 1866 (1961).

[108] M. R. Thuler, R. L. Benbow, and Z. Hurych, Phys. Rev. B **26**, 669 (1982).

[109] J. Ghijsen, L. H. Tjeng, H. Eskes, G. A. Sawatzky, and R. L. Johnson, Phys. Rev. B **42**, 2268 (1990).

[110] L. H. Tjeng, C. T. Chen, J. Ghijsen, P. Rudolf, and F. Sette, Phys. Rev. Lett. **67**, 501 (1991).

[111] C. Guillot, Y. Ballu, J. Paigné, J. Lecante, K. P. Jain, P. Thiry, R. Pinchaux, Y. Pétroff, and L. M. Falicov, Phys. Rev. Lett. **39**, 1632 (1977).

[112] J. Zaanen, G. A. Sawatzky, and J. W. Allen, Phys. Rev. Lett. **55**, 418 (1985).

[113] J. Zaanen, C. Westra, and G. A. Sawatzky, Phys. Rev. B **33**, 8060 (1986).

[114] A. E. Bocquet, T. Mizokawa, K. Morikawa, A. Fujimori, S. R. Barman, K. Maiti, D. D. Sarma, Y. Tokura, and M. Onoda, Phys. Rev. B **53**, 1161 (1996).

[115] S. Doniach and M. Šunjić, J. Phys. C: Solid State Phys. **3**, 285 (1970).

[116] D. B. McWhan, T. M. Rice, and J. P. Remeika, Phys. Rev. Lett. **23**, 1384 (1969).

[117] D. B. McWhan and J. P. Remeika, Phys. Rev. B **2**, 3734 (1970).

[118] D. B. McWhan, A. Menth, J. P. Remeika, W. F. Brinkman, and T. M. Rice, Phys. Rev. B **7**, 1920 (1973).

[119] N. F. Mott, Proc. Phys. Soc. A **62**, 416 (1949).

[120] R. M. Moon, Phys. Rev. Lett. **25**, 527 (1970).

[121] C. Castellani, C. R. Natoli, and J. Ranninger, Phys. Rev. B **18**, 4945 (1978).

[122] I. S. Elfimov, T. Saha-Dasgupta, and M. A. Korotin, Phys. Rev. B **68**, 113105 (2003).

[123] P. Roziera, A. Ratusznab, and J. Galy, Z. Anorg. Allg. Chem. **628**, 1236 (2002).

[124] C. E. Rice and W. R. Robinson, Acta Cryst. **B33**, 1342 (1977).

[125] L. K. Keys and L. N. Mulay, Phys. Rev. **154**, 453 (1967).

[126] R. M. Moon, T. Riste, W. C. Koehler, and S. C. Abrahams, J. Appl. Phys. **40**, 1445 (1969).

[127] L. L. van Zandt, J. M. Honig, and J. B. Goodenough, J. Appl. Phys. **39**, 594 (1968).

[128] L. F. Mattheiss, J. Phys.: Condens. Matter **8**, 5987 (1996).

[129] R. L. Kurtz and V. E. Henrich, Phys. Rev. B **25**, 3563 (1982).

[130] K. E. Smith and V. E. Henrich, Phys. Rev. B **38**, 5965 (1988). See Ref. [131].

[131] K. E. Smith and V. E. Henrich, Phys. Rev. B **38**, 9571 (1988).

[132] T. Uozumi, K. Okada, A. Kotani, Y. Tezuka, and S. Shin, J. Phys. Soc. Jpn. **65**, 1150 (1996).

[133] R. L. Kurtz and V. E. Henrich, Surface Science Spectra **5**, 179 (1998).

[134] J. M. Honig and T. B. Reed, Phys. Rev. **174**, 1020 (1968).

[135] C. Kunz, S. Thiess, B. Cowie, T.-L. Lee, and J. Zegenhagen, Nucl. Instr. and Meth. A **547**, 73 (2005).

[136] C. Dallera, L. Braicovich, L. Duò, A. Palenzona, G. Panaccione, G. Paolicelli, B. Cowie, and J. Zegenhagen, Nucl. Instr. and Meth. A **547**, 113 (2005).

[137] M. A. van Veenendaal and G. A. Sawatzky, Phys. Rev. Lett. **70**, 2459 (1993).

[138] T. Uozumi, K. Okada, and A. Kotani, J. Phys. Soc. Jpn. **62**, 2595 (1993).

[139] W. A. Harrison, *Electronic Structure and the Properties of Solids: The Physics of the Chemical Bond* (Dover Publications, New York, 1989).

[140] A. A. Taskin and Y. Ando, Phys. Rev. Lett. **95**, 176603 (2005).

[141] R. von Helmolt, J. Wecker, B. Holzapfel, L. Schultz, and K. Samwer, Phys. Rev. Lett. **71**, 2331 (1993).

[142] P. Schiffer, A. P. Ramirez, W. Bao, and S.-W. Cheong, Phys. Rev. Lett. **75**, 3336 (1995).

[143] H. Wu, Phys. Rev. B **62**, R11953 (2000).

[144] Z. Hu, H. Wu, M. W. Haverkort, H. H. Hsieh, H. J. Lin, T. Lorenz, J. Baier, A. Reichl, I. Bonn, C. Felser, A. Tanaka, C. T. Chen, and L. H. Tjeng, Phys. Rev. Lett. **92**, 207402 (2004).

[145] A. Maignan, C. Martin, D. Pelloquin, N. Nguyen, and B. Raveau, J. Solid State Chem. **142**, 247 (1999).

[146] A. A. Taskin, A. N. Lavrov, and Y. Ando, Phys. Rev. B **71**, 134414 (2005).

[147] D. Akahoshi and Y. Ueda, J. Solid State Chem. **156**, 355 (2001).

[148] C. Frontera, J. L. García-Muñoz, A. Llobet, and M. A. G. Aranda, Phys. Rev. B **65**, 180405 (2002).

[149] F. Fauth, E. Suard, V. Caignaert, and I. Mirebeau, Phys. Rev. B **66**, 184421 (2002).

[150] A. A. Taskin, A. N. Lavrov, and Y. Ando, Phys. Rev. Lett. **90**, 227201 (2003).

[151] A. Maignan, V. Caignaert, B. Raveau, D. Khomskii, and G. Sawatzky, Phys. Rev. Lett. **93**, 026401 (2004).

[152] Y. P. Chernenkov, V. P. Plakhty, V. I. Fedorov, S. N. Barilo, S. V. Shiryaev, and G. L. Bychkov, Phys. Rev. B **71**, 184105 (2005).

[153] V. P. Plakhty, Y. P. Chernenkov, S. N. Barilo, A. Podlesnyak, E. Pomjakushina, E. V. Moskvin, and S. V. Gavrilov, Phys. Rev. B **71**, 214407 (2005).

[154] H. Wu, Phys. Rev. B **64**, 092413 (2001).

[155] H. Wu, private communication (unpublished).

[156] H. Wu, Eur. Phys. J. B **30**, 501 (2002).

[157] W. R. Flavell, A. G. Thomas, D. Tsoutsou, A. K. Mallick, M. North, E. A. Seddon, C. Cacho, A. E. R. Malins, S. Patel, R. L. Stockbauer, R. L. Kurtz, P. T. Sprunger, S. N. Barilo, S. V. Shiryaev, and G. L. Bychkov, Phys. Rev. B **70**, 224427 (2004).

[158] K. Takubo, J.-Y. Son, T. Mizokawa, M. Soda, and M. Sato, Phys. Rev. B **73**, 075102 (2006).

[159] Z. X. Zhou, S. McCall, C. S. Alexander, J. E. Crow, P. Schlottmann, S. N. Barilo, S. V. Shiryaev, G. L. Bychkov, and R. P. Guertin, Phys. Rev. B **70**, 024425 (2004).

[160] J. K. Lang, Y. Baer, and P. A. Cox, J. Phys. F: Metal Phys. **11**, 121 (1981).

[161] Z. Hu, H. Wu, S. N. Barilo, H. H. Hsieh, H.-J. Lin, M. Kriener, T. Lorenz, S. V. Shiryaev, G. L. Bychkov, C. T. Chen, and L. H. Tjeng (unpublished).

Acknowledgements

Zum Schluss möchte ich mich bei allen bedanken, die in der einen oder anderen Weise zum Gelingen dieser Arbeit beigetragen haben. Einige von ihnen möchte ich hier besonders hervorheben.

An erster Stelle muss selbstverständlich mein Doktorvater stehen, Hao Tjeng. Er hat mir nicht nur die Gelegenheit gegeben, mich in einer außergewöhnlichen Arbeitsgruppe voller hervorragender Wissenschaftler mit aufregenden Themen zu beschäftigen. Hier habe ich gelernt, was es bedeutet, ein Experiment zu planen — von der ersten Schraube an der Kammer bis hin zum Design der Probenhalter —, was man braucht um die Messungen durchzuführen zu können, und wie man schlussendlich die Spektren zu "lesen" hat. Allein zu begreifen, wieviel dahinter steckt, ist ein langer Lernprozess gewesen. Ich habe dabei auch enorm von Haos unglaublicher Hingabe an seine Arbeit und seiner tiefen Einsicht sowohl in die experimentellen Details, als auch die Theorie der Vielteilchenphysik profitiert — nicht zuletzt durch die Auswahl der Systeme, die ich untersucht habe, ohne zu wissen oder selbst einschätzen zu können, um was für "Schätze" es sich dabei handelt. Ganz am Anfang meiner Doktorarbeit sagte mal jemand zu mir: "It's tough to work with Hao" und ich konnte zu dem Zeitpunkt nicht viel damit anfangen. Heute würde ich antworten: "Yeah, and it's worth it!"

Als ich mit meiner Arbeit in Haos Gruppe angefangen habe, hatte ich keinen Schimmer vom experimentellen Arbeiten im Labor im Allgemeinen oder Photoelektronenspektroskopie im Besonderen. Ich hab mir alle Mühe gegeben, mich zurecht zu finden, aber ohne die Hilfe und Erfahrung von Zhiwei Hu und Christian Schüßler-Langeheine wäre ich sicher nicht besonders weit gekommen. Die beiden haben mir geholfen, die XPS in Gang zu bringen und mit ihr zu arbeiten, sie haben Proben organisiert und mir gezeigt, wie man sie präpariert, und haben mich auch zu Messzeiten am Synchrotron begleitet. Wenn ich gar nicht weiter wusste, konnten sie mich immer aus dem Schlamassel holen. Ich habe viel von ihnen gelernt und sicherlich einiges von ihrer Arbeitsweise übernommen, ohne es gemerkt zu haben, denn bei kaum einer Messung, die ich gemacht habe, stand mir nicht mindestens einer der beiden zur Seite. Ich verdanke ihnen eine Menge.

Experimentalphysik ist zu einem nicht unerheblichen Maß immer auch Handwerk. Das bedeutet einerseits, dass es eine Kunst sein kann, die man erlernen muss oder beherrschen kann. Das heißt aber auch, dass es in gewissem Sinne körperliche Arbeit ist, die anstrengend sein kann. Ich habe in Jan Gegner eine große Hilfe gehabt bei der alltäglichen Laborarbeit und den Nachtschichten beim Messen, aber auch im gemeinsamen Kampf um Erkenntnis im Dickicht der Ahnungslosigkeit, z. B. gegen mysteriöse Fehlfunktionen der Röntgenquelle, gegen unerklärliche Strukturen

in den Spektren, oder die tiefen Geheimnisse der Austrittsarbeit. Wir haben häufig die Dinge aus verschiedenen Perspektiven gesehen, und in phantastischen Diskussionen herausgefunden, dass jeder nur einen Teil der Wahrheit gesehen hatte. Die Zusammenarbeit mit ihm war sehr angenehm und hat mich in vielerlei Hinsicht bereichert.

Auch über Festkörperphysik wusste ich zu Anfang meiner Doktorarbeit noch herzlich wenig. Mein Vorlesungswissen erwies sich bald als völlig unzureichend für meine Alltagsaufgaben, so dass ich einige Nachhilfestunden bei Maurits Haverkort nehmen musste, um mir Stück für Stück eine Vorstellung davon machen zu können, was diese korrelierten Elektronen umtreibt. Maurits ist das gewohnt, er hat der halben Gruppe Nachhilfe gegeben, weil er das auch so gut kann. Nicht nur, dass er (fast) alle Fragen beantworten kann, er kann sie auch (fast) immer so beantworten, dass der fragende hinterher schlauer ist. Maurits war auch immer eine gute Adresse, wenn man z. B. ein kleines Fortran-Programm brauchte, das ein Spektrum verbreitern kann, oder eine Software um Daten mit einem Unixsystem auszutauschen, oder wenn man mal schnell eine Clusterrechnung machen wollte, oder irgendwelche Informationen über ein bestimmtes Material, eine Person oder ein theoretisches Verfahren suchte oder irgend etwas anderes! Ich habe auch ihm eine Menge zu verdanken. Mit Jan und Maurits zusammen ist es Justina Schlappa zu verdanken, dass bei uns im Zimmer immer eine angenehme Atmosphäre herrschte, die die Arbeit hier sehr angenehm machte.

Die Zusammenarbeit zwischen den verschiedenen Arbeitsgruppen des Instituts, und darüber hinaus innerhalb des SFB 608, hat eine tolle Vielfalt an Möglichkeiten eröffnet und ein sehr angenehmes Klima erzeugt. Eigentlich muss ich mich bei jedem einzelnen aus der Tjeng–Gruppe bedanken, und bei sehr vielen Leuten aus dem Institut, weil sie alle kleinere oder größere Beiträge geleistet haben, die aber für mich oft eine große Hilfe dargestellt haben. Besonders hervorheben möchte ich die Jungs, die mit mir zusammen im XPS–Labor arbeitet haben, Ronnie Sutarto, Tim Haupricht, Sven Binder und Stefan Klein. Sie haben mir geholfen Proben zu präparieren und durch die Kammern zu schleusen, und z. T. Referenzspektren aufgenommen für meine Synchrotron–Runs. Dasselbe gilt für Chun Fu Chang, genannt Roger, der mich auch zum Messen nach Grenoble begleitet hat. Des öfteren war ich beim Umgang mit der Laue–Kamera oder dem Röntgendiffraktometer auf die Hilfe von Daniel Senff, Olaf Schumann und Alexander Gößling angewiesen, sowie Ralf Müller, Marco Reuther und Holger Roth bei der Probenvorbereitung im Chemieraum.

A large part of the data shown in this work were taken at the ESRF, Grenoble. Knowing how much work it is to set up a little machine like my XPS and get to know how to work with it, it is not hard to imagine that measuring at a machine you may not even have seen before takes a lot of help, let alone all the beamline stuff! To get all the beautiful results was only possible with the great and friendly support of Oscar Tjernberg, Giacomo Ghiringhelli, Nick Brookes, Federica Venturini, Júlio Cezar, Gilles Retout, Ray Barrett, and everybody at ID08, as well as Giancarlo Panaccione, Francesco Offi, Piero Torelli, Paolo Lacovig and the rest of VOLPE–team, Giulio Monaco, Simo Huotari and the people at ID16. They did not only set up wonderful photoemission spectrometers and take care of the high performance beamlines, they were heavily involved in the actual measurements and also arranged

things like my accommodation and a lot more.

Ich hatte das Glück, hervorragende Proben für meine Messungen zur Verfügung zu haben, die eine entscheidende Bedeutung für die Qualität meiner Spektren hatten. Die $LaCoO_3$– und Ti_2O_3–Einkristalle wurden hier am II. Physikalischen Institut von Christian Zobel bzw. Holger Roth aus der Gruppe von Thomas Lorenz gezüchtet und charakterisiert. Mein Dank geht an die ganze Lorenz-Gruppe für die Messung von Widerstand und Magnetisierung dieser und vieler anderer Proben, die ich untersucht habe. Diese Messungen sind teilweise von großer Bedeutung für meine Experimente gewesen, wenn es z. B. darum ging, die Orientierung der Proben herauszufinden, oder den Temperaturbereich, in dem Photoemission ohne größere Aufladungsprobleme noch möglich ist. Vielen Dank an Werner Reichelt vom Institut für Anorganische Chemie der TU Dresden für eine große Zahl wunderschöner VO_2-Einkristalle, die so groß und regelmäßig gezüchtet waren, dass man sie mit bloßem Auge orientieren konnte. Many thanks to Sergei Barilo from the Institute of Solid State and Semiconductor Physics of the National Academy of Sciences in Minsk, Belarus, for beautiful $GdBaCo_2O_{5.5}$ samples.

Ich habe außerdem eine Menge Unterstützung aller Art bei den großen und kleinen Schwierigkeiten des Alltags gehabt, die ich vielleicht allein nicht hätte bewältigen können, oder nur unter ungeheurem Aufwand meiner schrecklich knappen Zeit. Besonders Lucie Hamdan, die immer sofort wusste, was ich brauchte und wo man das finden konnte, ist eine unschätzbare Hilfe gewesen. Das tolle an Lucie ist, dass sie in verblüffender Weise mitdenken kann. Mit vielen Tipps und praktischen Ratschlägen, u. a. mit dem flüssigen Helium und der Rückleitung, hat mir Bruno Roden immer sehr helfen können. Für alle Computer– und Netzwerkfragen konnte ich mich jederzeit an Jonas Weinen, Olaf Schumann und Christian Schüßler–Langeheine wenden. Eine große Hilfe sind auch Gerd Menz und Bernd Wartenberg und die Jungs von der E–Werkstatt gewesen, sowie Werner Külzer and Jürgen Towara und die Leute aus der mechanischen Werkstatt, die wunderschöne Probenhalter und andere aufwändige Metallteile auch noch in allerletzter Minute absolut perfekt hergestellt haben. I would like to thank Jean Thibaut for very valuable help and documentation about the x–ray source, in particular his extremely quick response. Von existentieller Wichtigkeit war Andrea Severing, die dafür gesorgt hat, dass ich in Lohn und Brot geblieben bin. In diesem Zusammenhang bedanke ich mich bei der Deutschen Forschungsgemeinschaft, die meine Stelle am II. Physikalischen Institut über den Sonderforschungsbereich 608 "Komplexe Übergangsmetallverbindungen mit Spin– und Ladungsfreiheitsgraden und Unordnung" finanziert hat; bei der Wilhelm und Else Heraeus–Stiftung für die finanzielle Unterstützung der Reisen zu den DPG–Frühjahrstagungen 2004 – 2006; der Bundesrepublik Deutschland und den Bundesländern Nordrhein–Westfalen und Baden–Württemberg für die kostengünstige Ausbildung; und der EU für das ESRF.

Zum Schluss möchte ich mich bei allen bedanken, die einen eher indirekten aber entscheidenden Beitrag zu dieser Arbeit geleistet haben, meinen Lehrern, Freunden, meiner Familie und Mdm.

Erklärung

Ich versichere, dass ich die von mir vorgelegte Dissertation selbständig angefertigt, die benutzten Quellen und Hilfsmittel vollständig angegeben und die Stellen der Arbeit — einschließlich Tabellen, Karten und Abbildungen —, die anderen Werken im Wortlaut oder dem Sinn nach entnommen sind, in jedem Einzelfall als Entlehnung kenntlich gemacht habe; dass diese Dissertation noch keiner anderen Fakultät oder Universität zur Prüfung vorgelegen hat; dass sie — abgesehen von unten angegebenen Teilpublikationen — noch nicht veröffentlicht worden ist sowie, dass ich eine solche Veröffentlichung vor Abschluss des Promotionsverfahrens nicht vornehmen werde. Die Bestimmungen dieser Promotionsordnung sind mir bekannt. Die von mir vorgelegte Dissertation ist von Prof. Dr. L. H. Tjeng betreut worden.

Thomas Koethe

Publications

Transfer of Spectral Weight and Symmetry across the Metal–Insulator Transition in VO_2
T. C. Koethe, Z. Hu, M. W. Haverkort, C. Schüßler–Langeheine, F. Venturini, N. B. Brookes, O. Tjernberg, W. Reichelt, H. H. Hsieh, H.–J. Lin, C. T. Chen, and L. H. Tjeng
Physical Review Letters **97**, 116402 (2006)

Electronic structure of RAuMg and RAgMg (R = Eu, Gd, Yb)
Jan Gegner, T. C. Koethe, Hua Wu, Z. Hu, H. Hartmann, T. Lorenz, T. Fickenscher, R. Pöttgen, and L. H. Tjeng
Physical Review B **74**, 073102 (2006)

Lebenslauf

Persönliche Daten

Name	Thomas Christoph Koethe
Geburtsdatum	20. Dezember 1975
Geburtsort	Düsseldorf
Staatsangehörigkeit	Deutsch
Familienstand	ledig

Studium

1995	Allg. Hochschulreife
10/1996 – 10/1998	Physik Grundstudium, Vordiplom Universität Konstanz
10/1998 – 01/2003	Physik Hauptstudium, Diplom Universität zu Köln
seit 03/2003	Doktorarbeit am II. Physikalischen Institut Universität zu Köln